

Design of *De Novo* Mini Fluorescence Activating Proteins as pH and Calcium Biosensors

Jason C. Klima

A dissertation

submitted in partial fulfillment of the

requirements for the degree of

Doctor of Philosophy

University of Washington

2019

Reading Committee:

David Baker, Chair

James Bryant Hurley

Abhinav Nath

Program Authorized to Offer Degree:

Biochemistry

© Copyright 2019

Jason C. Klima

University of Washington

Abstract

Design of *De Novo* Mini Fluorescence Activating Proteins as pH and Calcium Biosensors

Jason C. Klima

Chair of the Supervisory Committee:

David Baker

Department of Biochemistry

Recent advances in *de novo* protein design have enabled the design of mini fluorescence activating proteins (mFAPs): mini β -barrel topologies that bind and stabilize the fluorescent *cis*-planar state of the fluorogenic compound DFHBI. mFAPs offer advantages over conventional fluorescent proteins, such as smaller molecular size, smaller genetic footprint, and high signal-to-noise ratio. As described herein, I employ structure-guided protein design to engineer mFAPs to be brighter (only 3.5-fold dimmer than enhanced green fluorescent protein (EGFP)), and both selective and promiscuous toward different chromophores (DFHBI, DFHBI-1T, and DFHO), revealing additional advantages of spectral tunability, external spatiotemporal control over fluorescence, and photostability. Additionally, we engineered mFAPs to have stable folds at low pH, and to bind the protonated (phenolic) and deprotonated (phenolate) states of DFHBI,

conferring pH-responsive fluorescence based on the protonation/deprotonation equilibrium of DFHBI with a ~250-fold change in ratiometric fluorescence from pH 3.6-8.4. Furthermore, molecular engineering of mFAPs to exhibit Ca²⁺-responsive fluorescence was achieved by grafting one, two, or four EF-hand motifs onto mFAP loops juxtaposing the DFHBI binding pocket to generate fluorescent Ca²⁺ biosensors capable of monitoring Ca²⁺ transients *in cyto* with high photostability. Both positive allosteric coupling and negative allosteric coupling between Ca²⁺ and DFHBI binding is observed, with >500-fold changes in the thermodynamic dissociation constant for Ca²⁺ depending on the number of EF-hand motifs used. Structural insight into the positive allosteric modulation mechanism is provided via X-ray crystallographic data and molecular dynamics simulations. While mFAPs still have much room for improvement, it is anticipated that these already improved mFAPs have numerous advanced imaging applications within the fields of molecular biology, nanobiotechnology, and beyond.

Acknowledgements

I would like to express my immense gratitude to my supervisors and co-mentors Drs. David Baker and James B. Hurley for their guidance and support throughout my graduate career, as well as that from all of my graduate committee members: Drs. David Baker, James B. Hurley, Abhinav Nath, Jihong Bai, and William N. Zagotta. I am grateful to post-doctoral researchers in the Baker Laboratory who have been terrific scientific mentors to me: Drs. Per Greisen, Gerard A. Daniel, Matthew J. Bick, Scott E. Boyken, and Anastassia A. Vorobieva. I thank all members and alumni of the Baker and Hurley Laboratories for discussions. I additionally would like to thank graduate students and colleagues in the University of Washington Department of Biochemistry and RosettaCommons community for discussions. I am grateful for the unconditional support from: MaryAnn Klima (mother), Rob Klima (father), Brian Matthew Klima (brother), Jenna Castle Klima (sister-in-law), Penelope Darwin Klima (niece), Eleanor Preis (grandmother) and Dr. Ursula Bellugi (grandmother), my extended family, and friends. Finally, I would like to thank the National Science Foundation (NSF) Graduate Research Fellowship Program (GRFP) for financial support.

Table of Contents

| | |
|---|-----------|
| Chapter 1. Introduction | 8 |
| Chapter 2. Engineering pH-responsive mFAPs | 13 |
| 2.1. Introduction | 13 |
| Figure 1. Characterization of brighter and chromophore-specific mFAP variants mFAP2a and mFAP2b | 14 |
| 2.2. Results | 16 |
| Figure 2. Engineering of mFAP2a and mFAP2b from mFAP2 | 18 |
| Figure 3. Photophysical characterization of mFAP2a and mFAP2b in complex with DFHBI or DFHBI-1T chromophores, and chromophores only | 19 |
| Table 1. Photophysical properties of mFAP2a and mFAP2b with DFHBI or DFHBI-1T compared with controls | 20 |
| Table 2. Relative fluorescence intensities, relative expression levels, and chromophore affinities of mFAP variants | 23 |
| Figure 4. Laser scanning confocal fluorescence microscopy of <i>E. coli</i> expressing either mFAP2a or mFAP2b mixed in a 1:1 cellular ratio demonstrating mFAP2b selectivity for DFHBI over DFHBI-1T and mFAP2a promiscuity for DFHBI and DFHBI-1T | 24 |
| Figure 5. Widefield epifluorescence microscopy of fixed COS-7 cells with expressed mFAP2a or mFAP2b to the endoplasmic reticulum (ER) using a C-terminal sec61 β localization sequence | 25 |
| Figure 6. Photostability of mFAP2a and mFAP2b with DFHBI and DFHBI-1T compared to AcGFP1 | 26 |
| Figure 7. Photophysical characterization of pH-responsive mFAP variants | 27 |
| Figure 8. Characterization of pH-responsive mFAP_pH | 29 |
| 2.3. mFAP Primary Amino Acid Sequences | 30 |
| Chapter 3. Engineering Ca²⁺-responsive mFAPs | 34 |
| 3.1. Introduction | 34 |
| 3.2. Results | 34 |
| Figure 9. Photophysical characterization and computational modeling of extended loop7 variants | 35 |
| Figure 10. Structures of motifs conferring Ca ²⁺ -responsiveness to mFAPs | 36 |
| Figure 11. <i>In vitro</i> characterization of Ca ²⁺ -responsive mFAPs | 37 |
| Figure 12. Far-ultraviolet (UV) circular dichroism (CD) characterization of EF4n_mFAP2b without DFHBI | 38 |
| Figure 13. Normalized fluorescence intensity of positively allosteric Ca ²⁺ -responsive mFAPs containing one EF-hand motif | 39 |

| | |
|--|-----------|
| Figure 14. Normalized fluorescence intensity of negatively allosteric Ca ²⁺ -responsive mFAPs containing one EF-hand motif | 40 |
| Figure 15. Normalized fluorescence intensity of negatively allosteric Ca ²⁺ -responsive mFAPs containing two EF-hand motifs | 41 |
| Figure 16. Normalized fluorescence intensity of negatively allosteric Ca ²⁺ -responsive mFAPs containing four EF-hand motifs | 42 |
| Figure 17. Theoretical thermodynamic properties of Ca ²⁺ -responsive mFAPs | 43 |
| Table 3. Thermodynamic properties of Ca ²⁺ -responsive mFAPs | 48 |
| Figure 18. X-ray crystal structure of the EF1p2_mFAP2b–DFHBI–Ca ²⁺ co-crystal structure solved at 2.1 Å resolution as a dimeric asymmetric unit (PDB ID 6OHH) | 49 |
| Table 4. X-ray crystallography data collection and refinement metrics for the EF1p2_mFAP2b–DFHBI–Ca ²⁺ co-crystal structure (PDB ID 6OHH) | 50 |
| Figure 19. Structural and <i>in cyto</i> characterization of Ca ²⁺ -responsive mFAPs | 51 |
| Figure 20. Molecular dynamics (MD) simulations of the X-ray crystal structure of EF1p2_mFAP2b under the four conditions: Apo, Ca ²⁺ -bound, DFHBI-bound, and Holo | 53 |
| Figure 21. Time-lapse epifluorescence microscopy of acetylcholine (ACh) stimulations of live HEK293 cells expressing cytosolic Ca ²⁺ -responsive mFAPs or GCaMP6f | 56 |
| Figure 22. Time-lapse epifluorescence microscopy of human induced pluripotent stem cell (hiPSC)-derived cardiomyocytes (CMs) expressing sarcoplasmic reticulum (SR)-targeted EF1n_mFAP2b | 58 |
| Figure 23. Processing time-lapse epifluorescence microscopy images of human induced pluripotent stem cell (hiPSC)-derived cardiomyocyte (CM) cells expressing sarcoplasmic reticulum (SR)-targeted EF1n_mFAP2b | 59 |
| 3.3. Extended Loop7 mFAP and Ca ²⁺ -responsive mFAP Primary Amino Acid Sequences | 60 |
| Chapter 4. Discussion, Materials and Methods | 62 |
| 4.1. Discussion | 62 |
| 4.2. Methods | 63 |
| Design of brighter and pH-responsive mFAPs | 63 |
| Design of chromophore-selective mFAPs | 65 |
| Design of extended loop library | 66 |
| Design of Ca ²⁺ -responsive mFAPs | 67 |
| Synthetic DNA construction | 68 |
| Large-scale protein purification | 69 |
| Size-exclusion chromatography (SEC) | 71 |
| Small-scale protein purification | 71 |
| Screening libraries | 72 |
| Fluorescence intensity assays | 73 |
| Densitometry | 75 |
| | 6 |

| | |
|--|------------|
| pH-dependent fluorescence assays | 75 |
| DFHBI, DFHBI-1T, and DFHO titrations | 79 |
| Ca ²⁺ -responsive mFAP DFHBI titrations | 80 |
| Ca ²⁺ -responsive mFAP Ca ²⁺ titrations | 82 |
| EF2n_mFAP2b DFHBI titration versus Ca ²⁺ titration heatmap | 83 |
| Circular dichroism (CD) | 84 |
| Quantum yield measurements | 84 |
| COS-7 cell culture, transfection, and fixation | 87 |
| Epifluorescence microscopy of COS-7 cells | 87 |
| Photostability assay | 88 |
| Laser scanning confocal fluorescence microscopy of <i>E. coli</i> | 89 |
| X-ray crystallography | 90 |
| Molecular dynamics (MD) simulations | 91 |
| HEK293 cell transfections | 93 |
| HEK293 cell Ca ²⁺ titrations | 94 |
| HEK293 cell acetylcholine stimulations | 95 |
| Human induced pluripotent stem cell (hiPSC)-derived cardiomyocyte (CM) imaging | 97 |
| 4.3. Code Availability | 99 |
| 4.4. Data Availability | 108 |
| 4.5. Acknowledgements | 108 |
| 4.6. Author Contributions | 109 |
| 4.7. Competing Interests | 110 |
| Chapter 5. Conclusion and Future Directions | 111 |
| References | 115 |
| Curriculum Vitae | 124 |
| Education | 124 |
| Publications | 124 |
| Awards and Honors | 124 |
| Work Experience | 125 |
| Research Skills | 126 |
| Teaching Experience | 127 |
| Volunteer Experience | 128 |
| Vitae | 128 |

Chapter 1. Introduction

Biosensors are useful tools utilized in molecular biology to spatiotemporally locate and quantify the concentration of analytes of interest for applications such as drug discovery, environmental monitoring, and disease diagnosis¹. My doctoral studies have focused on the molecular engineering of protein-based fluorescent biosensors for the detection and quantification of analytes of interest (i.e. Ca^{2+} , protons). Development of protein-based fluorescent biosensors typically involves grafting of an analyte-binding biorecognition module to different mutational variants of green fluorescent protein² (GFP), a 12-stranded intrinsically fluorescent protein molecule originating from the jellyfish *Aequorea victoria*. The discovery and re-engineering of GFP has revolutionized the field of molecular biology, allowing researchers to visualize dynamic cellular processes and accurately quantify the concentrations and spatial locations of proteins, ions, and metabolites in living cells using fluorescence microscopy. Fluorescence is a physical process characterized by an atom or molecule emitting electromagnetic radiation after absorbing higher energy electromagnetic radiation. Fluorescence microscopy is an imaging technique in which a picture is captured of a sample (e.g. a human cell in a petri dish) at high magnification by directing electromagnetic radiation onto the sample and recording the location and intensity of lower energy electromagnetic radiation emitted from the sample. The sample is labeled with fluorescent molecules to be detected, typically via genetic expression of GFP-based fluorescent biosensors. The re-engineering of GFP-based fluorescent biosensors for fluorescence microscopy applications has been hampered by an incomplete understanding of how the sequence of amino acids, the building blocks of proteins, encodes the three-dimensional structure and fluorescence properties of GFP. Traditional protein engineering

approaches employed to improve biosensors, such as directed evolution (using error-prone polymerase chain reaction³) and site-saturation mutagenesis⁴ (SSM), rely on random or exhaustive sampling of the sequence of amino acids to improve desirable photophysical parameters of GFP variants. Such approaches generate an enormous diversity of amino acid sequences that must be thoroughly screened *in vitro*. Many of the produced gene sequences encode proteins that do not fold into the desired three-dimensional shape, and consequently do not maintain desired functions such as displaying specific thermodynamic and photophysical properties. Therefore, directed evolution and SSM employ a non-systematic and laborious⁵ yet viable⁶ approach to protein engineering.

As opposed to traditional engineering approaches to GFP-based biosensors, *de novo* protein design is guided by the physical principles that underlie protein folding⁵, and explores the full amino acid sequence space *in silico* before expressing the re-engineered proteins *in vitro*. The recent advances in computational protein design techniques and computing power open up exciting prospects of overcoming the challenges of traditional protein engineering techniques such as directed evolution and SSM. Molecular engineering of *de novo* protein-based fluorescent biosensors provides the opportunity to not only complement, but even outperform, GFP-based fluorescent biosensors in terms of thermodynamic and photophysical properties. Although *de novo* protein design has its own set of challenges such as optimizing the energy function for the most physically realistic simulations *in silico*⁷, optimizing the degree of conformational sampling *in silico*⁸, and identifying computational metrics that correlate with the desired protein function⁹ (e.g. whether the surface shape complementarity value between analyte and protein may result in an increased analyte binding affinity and therefore fluorescence dynamic range of the engineered

fluorescent protein), we have overcome these multitudinous challenges to uncover principles for designing mini β -barrel topologies that bind the *cis*-planar conformation of the exogenous chromophore DFHBI¹⁰, which is similar in structure to the endogenous chromophore in GFP. The 8-stranded mini β -barrel topology contains a hydrophobic core essential for protein folding and a chromophore binding pocket with high shape and electrostatic complementarity with DFHBI. In Chapters 2, 3, and 4, I propose that these protein–chromophore complexes, called mini fluorescence activating proteins (mFAPs), constitute a versatile platform for engineering protein-based fluorescent biosensors.

By iteratively designing the amino acid sequence of mFAPs using Rosetta, a computer software suite for modeling proteins and macromolecules, and experimentally screening *E. coli* lysates expressing mFAPs for brighter fluorescence, I optimized mFAPs to be only 3.5-fold dimmer than enhanced GFP (EGFP), one of the brightest known GFP variants. Additionally, I was able to engineer mFAP molecules to modulate their fluorescence properties upon selective binding and unbinding to both hydrogen ions and calcium ions. Hydrogen ion (H^+) concentrations, also known as pH values, of specific compartments within human cells have been implicated in the homeostasis of human physiological¹¹ and disease conditions¹². Similarly, calcium ion (Ca^{2+}) concentrations dynamically fluctuate during cellular signaling events and are implicated in human neurobiological homeostasis¹³. As outlined in Chapters 2, 3, and 4, I have engineered mFAP molecules to reversibly modulate their fluorescence properties in both the presence and absence of hydrogen and calcium ions, allowing researchers to study dynamic molecular mechanisms of human diseases in real-time with high spatiotemporal precision inside of living cells using fluorescence microscopy. Although there is still considerable room to

improve mFAPs, engineering of novel protein-based fluorescent pH and Ca²⁺ ion biosensors provides researchers with new opportunities for innovation in the treatment of many human pathologies such as Alzheimer's and Parkinson's diseases.

Chapters 2, 3, and 4 comprise material that has been submitted for publication as:

mFAPs: A Versatile Platform For New Fluorescent Protein Sensor Engineering

Jason C. Klima^{1,2}, Lindsey A. Doyle³, Justin H. Lee^{4,5}, Michael Rappleye^{5,6}, Lauren A. Gagnon⁷, Min Yen Lee⁷, Anastassia A. Vorobieva^{1,2}, Jiayi Dou^{2,8}, Emilia P. Barros⁹, Samantha Bremner^{5,6}, Cameron M. Chow², Lauren Carter², David L. Mack^{5,6,10}, Rommie E. Amaro⁹, Joshua C. Vaughan^{7,11}, Andre Berndt^{4,5,6}, Barry L. Stoddard³, David Baker^{1,2,12}

¹Department of Biochemistry, University of Washington, Seattle, WA, USA.

²Institute for Protein Design, University of Washington, Seattle, WA, USA.

³Division of Basic Sciences, Fred Hutchinson Cancer Research Center, Seattle, WA, USA.

⁴Molecular Engineering Ph.D. Program, University of Washington, Seattle, WA, USA.

⁵Institute for Stem Cell and Regenerative Medicine, University of Washington, Seattle, WA, USA.

⁶Department of Bioengineering, University of Washington, Seattle, WA, USA.

⁷Department of Chemistry, University of Washington, Seattle, WA, USA.

⁸Current address: Department of Bioengineering, Stanford University, Stanford, CA, USA.

⁹Department of Chemistry and Biochemistry, University of California, San Diego, La Jolla, CA, USA.

¹⁰Department of Rehabilitation Medicine, University of Washington, Seattle, WA, USA.

¹¹Department of Physiology and Biophysics, University of Washington, Seattle, WA, USA.

¹²Howard Hughes Medical Institute, University of Washington, Seattle, WA, USA.

Abstract

Through the efforts of many groups¹²⁻¹⁷, a wide range of fluorescent protein reporters and sensors based on green fluorescent protein and its relatives have been engineered in recent years. Here we explore the versatility of a new platform for fluorescent reporter and sensor engineering based on a *de novo* designed fluorogenic protein that binds and stabilizes the fluorescent *cis*-planar state of the fluorogenic compound DFHBI. We show that the fluorescence intensity and specificity of these mFAPs (mini fluorescence activating proteins) for different chromophores can be tuned, and fluorescence properties modified by pH and Ca²⁺ ions for real-time fluorescence reporting. For example, a design which thermodynamically links DFHBI and Ca²⁺ binding enables direct visualization of individual Ca²⁺ ion transients in the sarcoplasmic reticulum of human cardiomyocytes. The relative ease with which new sensing modalities can be incorporated and advantages in smaller size and photostability make mFAPs attractive candidates for further fluorescent protein and biosensor development.

Chapter 2. Engineering pH-responsive mFAPs

2.1. Introduction

De novo designed mini fluorescence activating proteins (mFAPs) (Figure 1a) bind and fluorescently activate the fluorogenic compound ¹*DFHBI (compound **1**, Figure 1b) *in vitro* and in *E. coli*, yeast and mammalian cells¹⁰. DFHBI does not fluoresce when free in solution¹⁸, but becomes brightly fluorescent upon stabilization of the *cis*-planar conformation (also known as the planar *Z* conformation) through macromolecular binding¹⁹. RNA aptamers have been evolved to bind similar fluorogenic DFHBI-derived compounds^{20,21}, namely ²*DFHBI-1T (compound **2**, Figure 1c) and ³*DFHO, but to our knowledge so far no protein-based systems have been reported to bind and fluorescently activate DFHBI-1T or DFHO chromophores.

¹* 3,5-difluoro-4-hydroxybenzylidene imidazolinone

²* (Z)-4-(3,5-difluoro-4-hydroxybenzylidene)-2-methyl-1-(2,2,2-trifluoroethyl)-1H-imidazol-5(4H)-one

³* 3,5-difluoro-4-hydroxybenzylidene imidazolinone-2-oxime

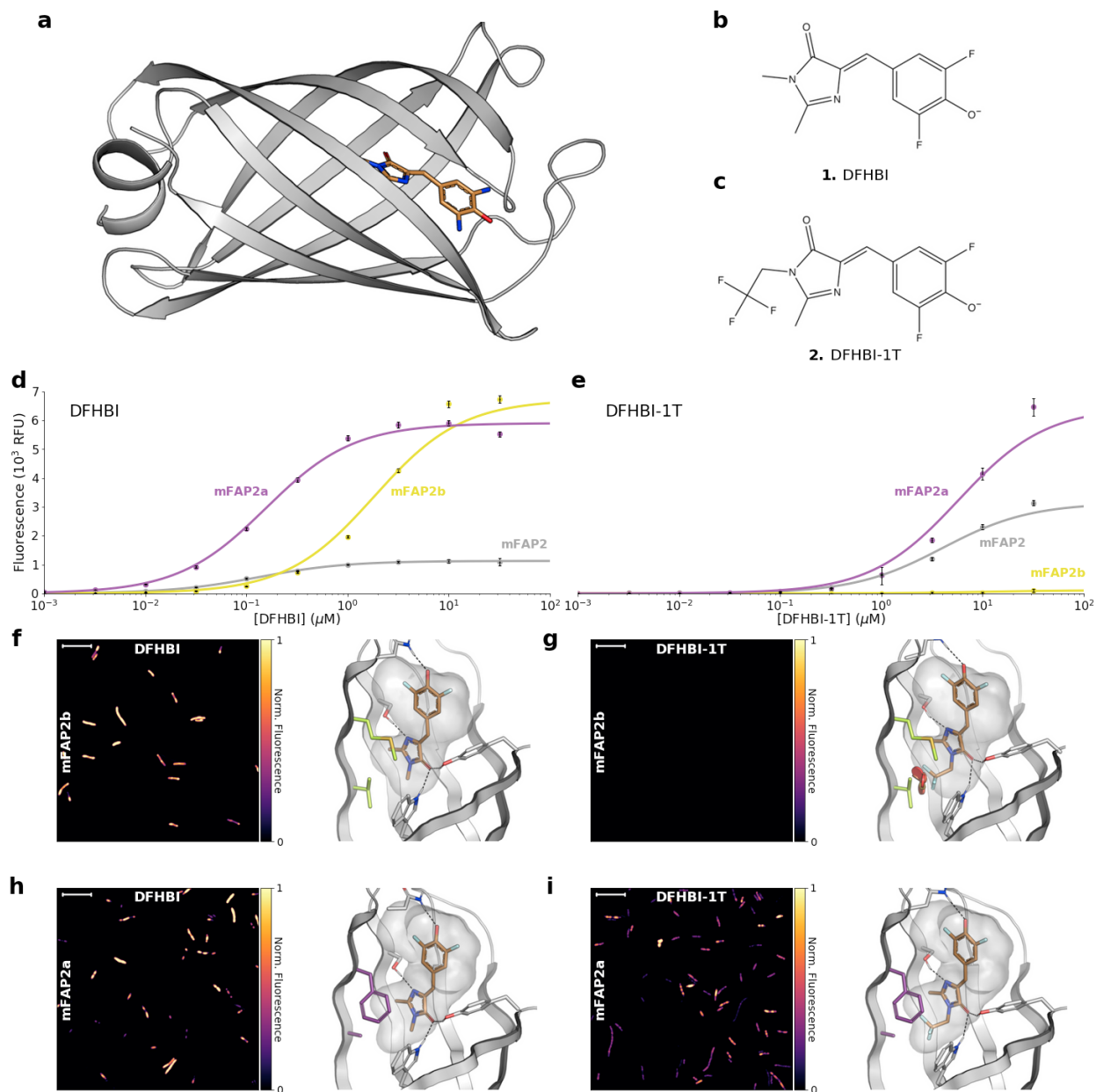


Figure 1. Characterization of brighter and chromophore-specific mFAP variants mFAP2a and mFAP2b

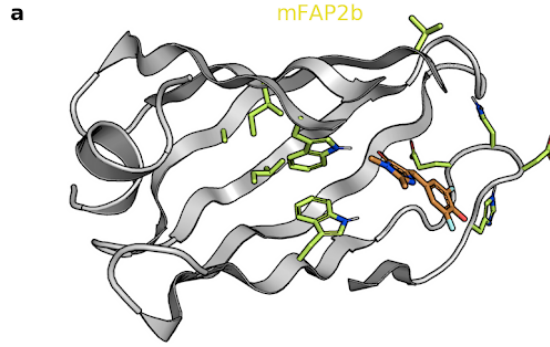
a, Design model of *de novo* β -barrel variant mFAP2b protein backbone (*cartoon*) bound to the DFHBI chromophore (*sticks*). **b,c**, Chemical structures of (**b**) DFHBI and (**c**) DFHBI-1T, respectively. **d,e**, *In vitro* titration of (**d**) DFHBI or (**e**) DFHBI-1T with mFAP2 (*grey*), mFAP2b (*lime*), and mFAP2a (*violet*) proteins. Error bars represent standard deviation of the mean of 8 technical replicates. Normalized means were fit to a single binding site isotherm equation using non-linear least squares fitting to obtain K_d values (Table 1), and the fits re-scaled to the maximum mean values (*lines*). **f-i**, Each panel shows a representative image of the fluorescence signal emitted by *E. coli* cells expressing the indicated mFAP variant labeled with 10 μ M

concentration of the indicated chromophore (*left*) and a zoom-in of the modeled binding pocket of that mFAP variant bound to that chromophore (*right*). The images (*left*) show the pseudo-colored normalized fluorescence intensity per pixel. Scale bars represent 10 microns. The design models (*right*) show the residues unique to mFAP2b (V13, M15) (*lime sticks*) or mFAP2a (A13, F15) (*violet sticks*). Intermolecular hydrogen bonds to the chromophore are shown (*black dotted lines*). Vacuum electrostatic contact potential around the chromophore is shown (*transparent grey surface*). **(f)** mFAP2b with DFHBI, **(g)** mFAP2b with DFHBI-1T does not emit a detectable fluorescence signal because binding is precluded by steric clashes of DFHBI-1T with V13 (*red cylinders*), **(h)** mFAP2a with DFHBI, and **(i)** mFAP2a with DFHBI-1T.

Optimization of *de novo* mFAPs to be brighter, chromophore-selective, pH-responsive, or Ca^{2+} -responsive has the potential to yield new sensors and fluorescent reporters with photophysical properties that complement or outperform those based on conventional fluorescent proteins, such as green fluorescent protein (GFP), in fluorescence microscopy applications. mFAPs have several properties that make them attractive candidates for further development. First, they are less than half the size of GFP, so their genetic footprint is smaller, fusions to proteins of interest are less perturbative, and their fluorescence is more tightly localized (for example, for Förster resonance energy transfer (FRET)-based probes of protein structure). Second, the bound chromophore can readily exchange with free chromophore in solution, and hence could be more photostable²². Third, chemical variants of DFHBI with different photophysical properties can be added, providing more control over color (i.e. fluorescence excitation and emission wavelength) than intrinsically fluorescent proteins²³. Finally, *de novo* mFAPs can be engineered to remain folded at low pH, allowing the possibility to engineer fluorescent pH biosensors.

2.2. Results

We sought to improve the stability of mFAPs at low pH, the binding affinity to the protonated (phenolic) and deprotonated (phenolate) states of DFHBI, as well as the fluorescence intensity of both complexes. mFAP2 was chosen for optimization because it has the brightest fluorescence (absolute quantum yield of 2.1%) and highest affinity (K_d of ~180 nM) for the deprotonated state of DFHBI compared to mFAP1¹⁰. Through a series of library selections (see Section 4.2) targeting aliphatic and aromatic residues directly interacting with DFHBI or in the hydrophobic core of the β -barrel, as well as residues in the loop connecting the seventh and eighth β -strands (hereafter referred to as loop7), we obtained brighter and chromophore-selective mFAP2 variants mFAP2a and mFAP2b that are 12 and 10 mutations from mFAP2, respectively (Figure 2).



```

#FAP_ph .....I.....V...A.....I.....END.H.....
#FAP2a .....A.F.....W.....I.....V...A.....I.....W.....END.H.....
#FAP2b .....W.....I.....V...A.....I.....W.....END.H.....
#FAP2.5 .....W.....I.....V...A.....I.....W.....END.H.....
#FAP2.4 .....W.....I.....V...A.....I.....W.....END.H.....
#FAP2.3 .....W.....I.....V...A.....I.....W.....END.H.....
#FAP2.2 .....W.....I.....V...A.....I.....W.....END.H.....
#FAP2.1 .....T.V.....
#FAP2  SRAAQLLPGTWVHTNTNEDGQTSQGMHFQPRSPYTHDVAAGTISDGRPIISGYGKVTVKTPDITLQVDITYPPLGNIAAGGQITHDSPTFKFDATTKGAGNFGRLTGLRORR

```

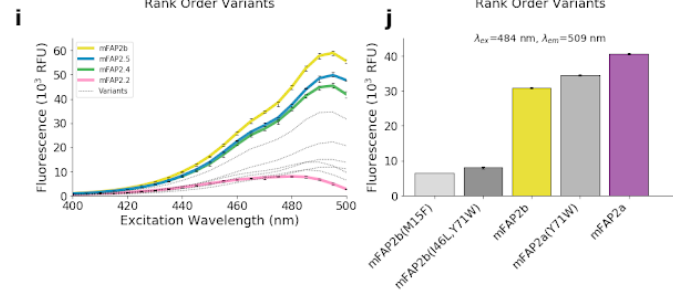
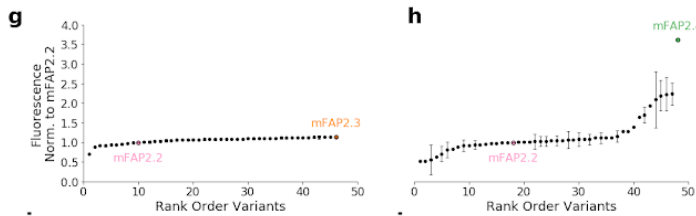
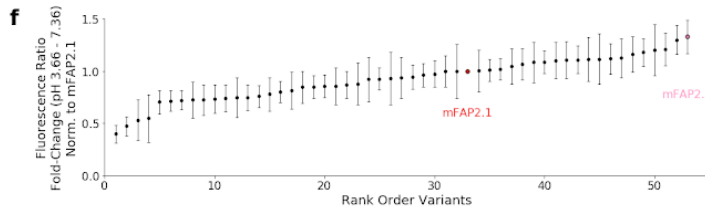
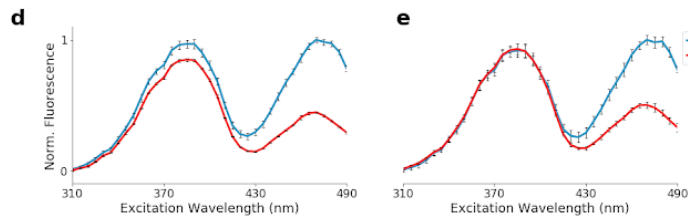
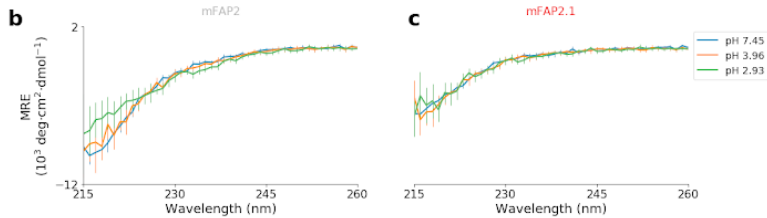


Figure 2. Engineering of mFAP2a and mFAP2b from mFAP2

a, Computational model of mFAP2b showing backbone (*grey cartoon*) and residues mutated from the original design mFAP2 (*lime sticks*) with DFHBI bound (*copper sticks*). Below, a multiple sequence alignment of mFAP mutants. **b**, Average (n=1) far-ultraviolet (UV) circular dichroism (CD) spectra of mFAP2 reveals that β -sheet character diminishes at low pH. **c**, Average (n=1) far-UV CD spectra of mFAP2.1 demonstrates similar β -sheet character across high and low pH. **d**, Average (n=3) mFAP2 fluorescence emission spectra reveals that fluorescence emission from the protonated (phenolic) state of DFHBI (with blueshifted excitation peak) diminishes between pH 4.22 and pH 3.66. **e**, Average (n=3) mFAP2.1 fluorescence emission spectra reveals that fluorescence emission from the protonated (phenolic) state of DFHBI (with blueshifted excitation peak) remains approximately constant at pH 4.22 and pH 3.66. **f**, Average (n=3 technical replicates of n=1-5 biological replicates) fluorescence ratio fold-change from pH 3.66-7.36 normalized to that of mFAP2.1 of selected mFAP2.1 variants from the β -barrel site-directed mutagenesis (SDM) library. **g**, Fluorescence intensity (n=1) or average fluorescence intensity where error bars are shown (n=2-20) from the deprotonated (phenolate) state of DFHBI normalized to that of mFAP2.2 of selected mFAP2.2 variants from the β -barrel loop7 combinatorial library. **h**, Fluorescence intensity (n=1) or average fluorescence intensity where error bars are shown (n=2-16) from the deprotonated (phenolate) state of DFHBI normalized to that of mFAP2.2 of selected mFAP2.2 variants from the β -barrel core residue combinatorial library. **i**, Average (n=3) fluorescence excitation spectra at neutral pH of equimolar selected mFAP2.5 variants from the β -barrel methyl group combinatorial library labeled with the DFHBI concentration 10-fold below the protein concentration. **j**, Average (n=3) fluorescence intensity from the deprotonated (phenolate) form of DFHBI labeled 10-fold below protein concentration of equimolar selected mFAP2b variants from the β -barrel aromatics and aliphatics combinatorial library. **b,c**, Error bars represent the standard deviation of the mean of 3 measurements per wavelength. **d,e**, Error bars represent the standard deviation of the mean of 3 technical replicates. **f**, Error bars represent the standard deviation of the mean of 3 technical replicates of 1-5 biological replicates. **g**, Error bars represent the standard deviation of the mean of 2-20 biological replicates. **h**, Error bars represent the standard deviation of the mean of 2-16 biological replicates. **i,j**, Error bars represent the standard deviation of the mean of 3 technical replicates.

In vitro titrations of mFAP2, mFAP2a, and mFAP2b with either DFHBI (Figure 1d) or DFHBI-1T (Figure 1e) and quantum yield measurements (Figure 3, Table 1) showed that mFAP2 has brighter fluorescence with DFHBI-1T than DFHBI but binds DFHBI with ~30.4-fold higher affinity; mFAP2a has ~2.5-fold brighter fluorescence with DFHBI-1T than DFHBI but binds DFHBI with ~37.3-fold higher affinity; and mFAP2b has ~29.8-fold brighter fluorescence with

DFHBI than DFHBI-1T and binds DFHBI with ~ 5.8 -fold higher affinity than DFHBI-1T. The mFAP2a–DFHBI-1T complex is the brightest known, with 12.9% absolute quantum yield (under $\sim 96\%$ saturation conditions) resulting in ~ 132 -fold fluorescence activation over free DFHBI-1T (Table 1).

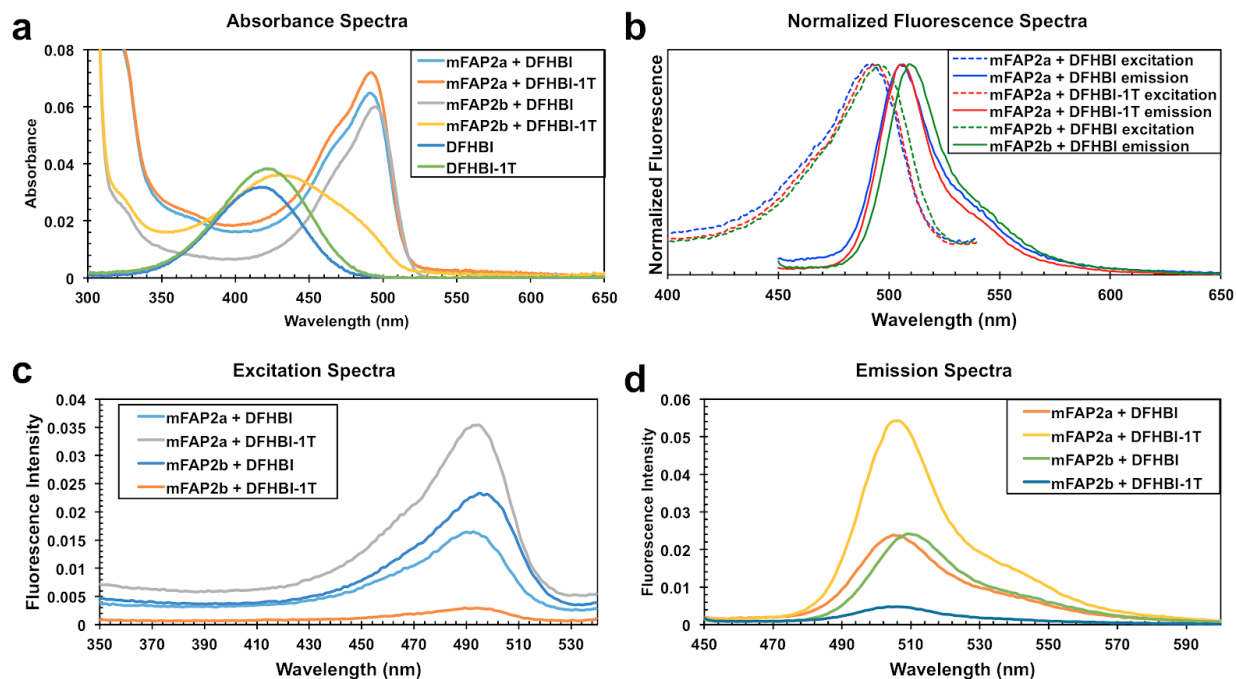


Figure 3. Photophysical characterization of mFAP2a and mFAP2b in complex with DFHBI or DFHBI-1T chromophores, and chromophores only

a, Absorbance spectra of $\sim 1 \mu\text{M}$ protein–chromophore complexes or $1 \mu\text{M}$ chromophores. **b**, Normalized fluorescence excitation (*dotted lines*) and emission (*solid lines*) spectra of $\sim 1 \mu\text{M}$ protein–chromophore complexes in relative fluorescence units (RFU). **c**, Unnormalized fluorescence excitation spectra of $\sim 1 \mu\text{M}$ protein–chromophore complexes in RFU. **d**, Unnormalized fluorescence emission spectra of $\sim 1 \mu\text{M}$ protein–chromophore complexes in RFU.

| | λ_{abs} (nm)* | λ_{ex} (nm)* | λ_{em} (nm)* | Extinction Coefficient (M ⁻¹ ·cm ⁻¹)† | Brightness‡ | Absolute Quantum Yield§ | Relative Quantum Yield§ | Reported Quantum Yield | % Bound | K _d (μM) |
|----------------------------------|---------------------------------|--------------------------------|--------------------------------|--|-------------------------------------|-------------------------------|-------------------------------|------------------------------|------------|---------------------|
| EGFP | - | 488# | 507# | 56,000# | 33,600# | - | - | 0.60# | - | - |
| mFAP2a + DFHBI | 491 | 491 | 505 | 64,873 | 3,892 | 0.060 | 0.063 | - | 99.9 | 0.15 ± 0.01 |
| mFAP2a + DFHBI-1T | 492 | 493 | 505 | 75,113 | 9,690 (3.5x dimmer than EGFP) | 0.129 | 0.128 | - | 95.8 | 5.78 ± 0.86 |
| mFAP2b + DFHBI | 495 | 495 | 509 | 60,533 | 5,630 | 0.093 | 0.099 | - | 99.1 | 1.83 ± 0.25 |
| mFAP2b + DFHBI-1T | 430 | 494 | 505 | 37,843 | 189 | 0.005 | 0.003 | - | 95.1 | 10.53 ± 3.08 |
| DFHBI | 418# | 423# | 489# | 30,100# 31,935# | - | 0.001# | - | 0.0007# | - | - |
| DFHBI-1T | 422# | 426# | 495# | 35,400# | - | - | - | 0.00098# | - | - |

Table 1. Photophysical properties of mFAP2a and mFAP2b with DFHBI or DFHBI-1T compared with controls

The % bound values are calculated based on the reported K_d values and final protein and chromophore concentrations used in quantum yield measurements. K_d values are obtained by non-linear least squares fits to the mean fluorescence intensities of the 8 technical replicates per chromophore titration (Figure 1d,e). K_d error estimates are the standard deviations of the mean of the non-linear least squares fits. * λ_{abs} is peak absorbance wavelength, λ_{ex} is peak excitation wavelength, and λ_{em} is peak emission wavelength. † Extinction coefficients are measured from λ_{abs} estimated based on 1 data point in this study. ‡ Brightness is defined as extinction coefficient multiplied by absolute quantum yield. § Absolute quantum yield is the average of 10 scans measured with an integrating sphere; relative quantum yield is reported using Acridine Yellow G²⁴ and fluorescein as reference standards. ¶ Previously reported value²⁰. # Previously reported value¹⁰.

Relative fluorescence intensities and thermodynamic dissociation constants (K_d values) for the deprotonated states of DFHBI, DFHBI-1T, and DFHO for the Ca²⁺-independent mFAP variants presented in this study are given in Table 2 (for example, mFAP3 binds the orange-red

colored DFHO chromophore with ~10-fold lower fluorescence intensity than mFAP2b with DFHBI).

| | 10 μ M DFHBI | 10 μ M DFHBI-1T | 10 μ M DFHO | Densitometry | | 100nM DFHBI | 100nM DFHBI-1T | 100nM DFHO | Densitometry | | DFHBI K _d (μ M) | DFHBI-1T K _d (μ M) | DFHO K _d (μ M) |
|------------|------------------|---------------------|-----------------|--------------|------------|-------------|----------------|-------------|--------------|------------|---------------------------------|------------------------------------|--------------------------------|
| mFAP2b | 1.0 ± 0.0 | 0.01 ± 0.0 | 0.01 ± 0.0 | 0.4858 | mFAP2a | 1.0 ± 0.0 | 0.59 ± 0.06 | 0.03 ± 0.01 | 0.3875 | mFAP0.2 | < 0.5 (0.0008 ± 0.01) | < 0.5 (0.2958 ± 0.03) | < 0.5 (0.0003 ± 0.01) |
| mFAP4 | 0.89 ± 0.13 | 0.14 ± 0.01 | 0.02 ± 0.0 | 0.4489 | mFAP3 | 0.96 ± 0.02 | 0.39 ± 0.07 | 0.05 ± 0.02 | 0.2893 | mFAP2c.13 | < 0.5 (0.0067 ± 0.01) | 79.4970 ± 29.51 | 42.3372 ± 23.82 |
| mFAP5 | 0.81 ± 0.13 | 0.04 ± 0.0 | 0.01 ± 0.0 | 0.7636 | mFAP5 | 0.93 ± 0.03 | 0.04 ± 0.01 | 0.01 ± 0.0 | 0.7636 | mFAP2a | 0.0546 ± 0.01 | 3.7039 ± 0.56 | 8.4683 ± 1.99 |
| mFAP2.5 | 0.8 ± 0.03 | 0.01 ± 0.0 | 0.0 ± 0.0 | 0.6405 | mFAP2.5 | 0.83 ± 0.02 | 0.01 ± 0.0 | 0.01 ± 0.0 | 0.6405 | mFAP0.3 | < 0.5 (0.0689 ± 0.10) | < 0.5 (0.0030 ± 0.01) | 2.1082 ± 1.49 |
| mFAP2a | 0.77 ± 0.12 | 0.92 ± 0.05 | 0.04 ± 0.0 | 0.3875 | mFAP2b | 0.82 ± 0.02 | 0.01 ± 0.0 | 0.01 ± 0.0 | 0.4858 | mFAP2c.5 | < 0.5 (0.0945 ± 0.02) | 1.1874 ± 0.22 | 3.9817 ± 1.54 |
| mFAP2.4 | 0.69 ± 0.06 | 0.01 ± 0.0 | 0.0 ± 0.0 | 0.7495 | mFAP4 | 0.81 ± 0.03 | 0.04 ± 0.01 | 0.01 ± 0.0 | 0.4489 | mFAP3 | 0.1012 ± 0.06 | 2.3442 ± 0.38 | 3.5622 ± 1.81 |
| mFAP3 | 0.65 ± 0.14 | 0.63 ± 0.07 | 0.1 ± 0.01 | 0.2893 | mFAP7 | 0.79 ± 0.04 | 0.29 ± 0.07 | 0.01 ± 0.0 | 0.2519 | mFAP2c.11 | < 0.5 (0.1117 ± 0.02) | 0.8747 ± 0.12 | 3.9982 ± 1.21 |
| mFAP2.2.9 | 0.64 ± 0.03 | 0.01 ± 0.0 | 0.0 ± 0.0 | 0.9665 | mFAP2.4 | 0.69 ± 0.03 | 0.01 ± 0.0 | 0.01 ± 0.0 | 0.7495 | mFAP2.2.13 | < 0.5 (0.1153 ± 0.03) | 1.0636 ± 0.18 | 3.7849 ± 3.10 |
| mFAP2.5.1 | 0.61 ± 0.02 | 0.01 ± 0.0 | 0.01 ± 0.0 | 0.5421 | mFAP2.2.9 | 0.69 ± 0.01 | 0.02 ± 0.0 | 0.01 ± 0.0 | 0.9665 | mFAP2c.9 | < 0.5 (0.1292 ± 0.02) | 1.6795 ± 0.23 | 6.0611 ± 1.97 |
| mFAP7 | 0.52 ± 0.09 | 0.47 ± 0.04 | 0.01 ± 0.0 | 0.2519 | mFAP2.2.10 | 0.61 ± 0.01 | 0.01 ± 0.0 | 0.01 ± 0.0 | 0.8843 | mFAP2c.12 | < 0.5 (0.1404 ± 0.02) | 0.7317 ± 0.09 | 3.4271 ± 1.32 |
| mFAP2.2.10 | 0.44 ± 0.04 | 0.01 ± 0.0 | 0.0 ± 0.0 | 0.8843 | mFAP2.5.2 | 0.55 ± 0.03 | 0.01 ± 0.0 | 0.01 ± 0.0 | 0.4993 | mFAP2.3 | < 0.5 (0.1463 ± 0.02) | 1.5844 ± 0.34 | 10.4115 ± 3.59 |
| mFAP2.5.2 | 0.39 ± 0.05 | 0.0 ± 0.0 | 0.0 ± 0.0 | 0.4993 | mFAP2.5.1 | 0.4 ± 0.04 | 0.01 ± 0.0 | 0.01 ± 0.0 | 0.5421 | mFAP2.2.12 | < 0.5 (0.1517 ± 0.02) | 1.9995 ± 0.31 | 5.8276 ± 4.89 |
| mFAP2.5.3 | 0.36 ± 0.02 | 0.01 ± 0.0 | 0.0 ± 0.0 | 0.4504 | mFAP6 | 0.29 ± 0.04 | 0.01 ± 0.0 | 0.01 ± 0.0 | 0.6829 | mFAP2.2.17 | < 0.5 (0.1529 ± 0.02) | 3.1093 ± 0.38 | 4.2661 ± 4.16 |
| mFAP2.5.4 | 0.34 ± 0.01 | 0.05 ± 0.01 | 0.01 ± 0.0 | 0.5709 | mFAP2.5.4 | 0.22 ± 0.0 | 0.02 ± 0.0 | 0.01 ± 0.0 | 0.5709 | mFAP2.2.7 | < 0.5 (0.1541 ± 0.03) | 1.3177 ± 0.22 | 0.7445 ± 0.77 |
| mFAP2.5.5 | 0.25 ± 0.01 | 0.0 ± 0.0 | 0.0 ± 0.0 | 0.5419 | mFAP2.0.1 | 0.22 ± 0.0 | 0.04 ± 0.0 | 0.01 ± 0.0 | 0.5854 | mFAP2.2.1 | < 0.5 (0.1569 ± 0.03) | 1.6601 ± 0.34 | < 0.5 (0.0098 ± 0.01) |
| mFAP2.2.2 | 0.23 ± 0.01 | 0.83 ± 0.08 | 0.02 ± 0.0 | 0.825 | mFAP2.5.5 | 0.21 ± 0.02 | 0.01 ± 0.0 | 0.01 ± 0.0 | 0.5419 | mFAP2.2.16 | < 0.5 (0.1594 ± 0.03) | 3.1061 ± 0.43 | 2.3478 ± 2.35 |
| mFAP2.2.1 | 0.23 ± 0.02 | 0.81 ± 0.06 | 0.02 ± 0.0 | 0.8782 | mFAP1 | 0.18 ± 0.0 | 0.01 ± 0.0 | 0.01 ± 0.0 | 0.4326 | mFAP2c.10 | < 0.5 (0.1630 ± 0.03) | 3.3847 ± 0.87 | 8.9359 ± 2.65 |
| mFAP2bL2 | 0.22 ± 0.03 | 0.0 ± 0.0 | 0.01 ± 0.0 | 0.191 | mFAP2.5.3 | 0.16 ± 0.04 | 0.01 ± 0.0 | 0.01 ± 0.0 | 0.4504 | mFAP_pH | < 0.5 (0.1638 ± 0.04) | 1.5031 ± 0.31 | 10.4730 ± 4.57 |
| mFAP2bL5 | 0.22 ± 0.02 | 0.0 ± 0.0 | 0.0 ± 0.0 | 0.4088 | mFAP_pH | 0.16 ± 0.0 | 0.2 ± 0.0 | 0.01 ± 0.0 | 0.2222 | mFAP2c.3 | < 0.5 (0.1782 ± 0.03) | 1.2777 ± 0.26 | 10.9815 ± 4.99 |
| mFAP2.2.3 | 0.21 ± 0.03 | 0.65 ± 0.06 | 0.01 ± 0.0 | 0.6837 | mFAP2.2.4 | 0.15 ± 0.0 | 0.5 ± 0.02 | 0.02 ± 0.0 | 0.654 | mFAP2c.4 | < 0.5 (0.1945 ± 0.02) | 4.0694 ± 0.45 | 8.5976 ± 1.45 |
| mFAP2.2.4 | 0.2 ± 0.03 | 0.66 ± 0.04 | 0.01 ± 0.0 | 0.654 | mFAP2.3 | 0.15 ± 0.0 | 0.52 ± 0.02 | 0.02 ± 0.0 | 0.7958 | mFAP2.2.2 | < 0.5 (0.1957 ± 0.03) | 4.1160 ± 0.28 | 13.2598 ± 7.38 |
| mFAP2.2.12 | 0.2 ± 0.03 | 0.61 ± 0.04 | 0.01 ± 0.0 | 0.8731 | mFAP2.2.3 | 0.15 ± 0.0 | 0.43 ± 0.02 | 0.02 ± 0.0 | 0.6837 | mFAP2c.0 | < 0.5 (0.1986 ± 0.03) | 2.3890 ± 0.49 | 10.1867 ± 3.05 |
| mFAP2.2.3 | 0.2 ± 0.03 | 0.67 ± 0.04 | 0.01 ± 0.0 | 0.7958 | mFAP2.2.1 | 0.15 ± 0.0 | 0.59 ± 0.0 | 0.02 ± 0.0 | 0.8782 | mFAP2.2.15 | < 0.5 (0.2058 ± 0.03) | 3.2757 ± 0.79 | 4.6730 ± 4.43 |
| mFAP2.0.1 | 0.19 ± 0.01 | 0.05 ± 0.01 | 0.0 ± 0.0 | 0.5854 | mFAP2.2.2 | 0.15 ± 0.0 | 0.54 ± 0.01 | 0.02 ± 0.0 | 0.825 | mFAP2c.1 | < 0.5 (0.2125 ± 0.02) | 0.9018 ± 0.17 | 7.8463 ± 2.69 |
| mFAP8 | 0.18 ± 0.02 | 0.0 ± 0.0 | 0.0 ± 0.0 | 0.3208 | mFAP2c.0 | 0.14 ± 0.0 | 0.19 ± 0.01 | 0.01 ± 0.0 | 0.4216 | mFAP2.2.3 | < 0.5 (0.2129 ± 0.04) | 1.8521 ± 0.36 | 5.9604 ± 3.54 |
| mFAP2bL4 | 0.18 ± 0.02 | 0.0 ± 0.0 | 0.0 ± 0.0 | 0.3462 | mFAP2.2.15 | 0.14 ± 0.0 | 0.3 ± 0.0 | 0.01 ± 0.0 | 0.7157 | mFAP2.2.14 | < 0.5 (0.2137 ± 0.04) | 3.2697 ± 0.54 | 8.4056 ± 6.83 |
| mFAP2.2 | 0.17 ± 0.03 | 0.55 ± 0.02 | 0.01 ± 0.0 | 0.4749 | mFAP2bL5 | 0.14 ± 0.02 | 0.01 ± 0.0 | 0.01 ± 0.0 | 0.4088 | mFAP2.2.4 | < 0.5 (0.2255 ± 0.02) | 1.9117 ± 0.50 | 5.1666 ± 2.90 |
| mFAP2.2.5 | 0.17 ± 0.03 | 0.61 ± 0.0 | 0.01 ± 0.0 | 0.6397 | mFAP2.2.5 | 0.14 ± 0.0 | 0.46 ± 0.01 | 0.02 ± 0.0 | 0.6397 | mFAP2.2.6 | < 0.5 (0.2377 ± 0.03) | 3.2757 ± 0.33 | 6.1682 ± 3.07 |
| mFAP2.2.6 | 0.16 ± 0.03 | 0.46 ± 0.03 | 0.01 ± 0.0 | 0.6241 | mFAP2.2.16 | 0.14 ± 0.0 | 0.34 ± 0.0 | 0.02 ± 0.0 | 0.5464 | mFAP2c.8 | < 0.5 (0.2742 ± 0.05) | 1.8872 ± 0.38 | 5.2470 ± 1.98 |
| mFAP2.2.13 | 0.15 ± 0.03 | 0.5 ± 0.0 | 0.01 ± 0.0 | 0.9546 | mFAP2.2.13 | 0.14 ± 0.0 | 0.54 ± 0.0 | 0.03 ± 0.0 | 0.9546 | mFAP4 | < 0.5 (0.2839 ± 0.08) | 20.4951 ± 2.85 | 12.8162 ± 4.05 |
| mFAP6 | 0.15 ± 0.01 | 0.0 ± 0.0 | 0.0 ± 0.0 | 0.6829 | mFAP2.2.17 | 0.14 ± 0.0 | 0.1 ± 0.01 | 0.01 ± 0.0 | 0.3296 | mFAP7 | < 0.5 (0.3407 ± 0.09) | 3.7127 ± 0.33 | 16.0744 ± 3.93 |
| mFAP2 | 0.14 ± 0.03 | 0.33 ± 0.04 | 0.01 ± 0.0 | 0.4332 | mFAP2.2.12 | 0.13 ± 0.0 | 0.47 ± 0.0 | 0.02 ± 0.0 | 0.8731 | mFAP2a.1 | < 0.5 (0.4256 ± 0.02) | 3.3935 ± 0.45 | 6.6887 ± 1.50 |
| mFAP2.2.7 | 0.14 ± 0.03 | 0.45 ± 0.01 | 0.01 ± 0.0 | 0.6313 | mFAP2.1 | 0.13 ± 0.0 | 0.34 ± 0.01 | 0.01 ± 0.0 | 0.4747 | mFAP2c.14 | < 0.5 (0.4598 ± 0.77) | 16.3926 ± 13.03 | 55.0423 ± 23.95 |
| mFAP2.2.14 | 0.14 ± 0.03 | 0.28 ± 0.02 | 0.01 ± 0.0 | 0.7266 | mFAP2.2 | 0.13 ± 0.0 | 0.33 ± 0.02 | 0.01 ± 0.0 | 0.4749 | mFAP1 | < 0.5 (0.4958 ± 0.09) | 10.8040 ± 1.00 | 7.7959 ± 2.89 |
| mFAP1 | 0.13 ± 0.02 | 0.01 ± 0.0 | 0.0 ± 0.0 | 0.4326 | mFAP2a.0 | 0.13 ± 0.02 | 0.01 ± 0.0 | 0.01 ± 0.0 | 0.318 | mFAP5 | 0.8771 ± 0.14 | 48.9042 ± 7.78 | 28.8692 ± 13.17 |
| mFAP2bL3 | 0.13 ± 0.03 | 0.0 ± 0.0 | 0.0 ± 0.0 | 0.1451 | mFAP2.2.6 | 0.13 ± 0.0 | 0.35 ± 0.01 | 0.02 ± 0.0 | 0.6241 | mFAP2.2.9 | 0.9454 ± 0.05 | 21.6794 ± 3.99 | 1.9498 ± 2.11 |
| mFAP2.2.15 | 0.13 ± 0.03 | 0.27 ± 0.02 | 0.0 ± 0.0 | 0.7157 | mFAP2.2.14 | 0.13 ± 0.0 | 0.26 ± 0.01 | 0.01 ± 0.0 | 0.7266 | mFAP2.2.10 | 1.0351 ± 0.15 | 19.5162 ± 5.39 | < 0.5 (0.0016 ± 0.01) |
| mFAP2bL1 | 0.12 ± 0.02 | 0.0 ± 0.0 | 0.0 ± 0.0 | 0.2045 | mFAP2.2.7 | 0.13 ± 0.0 | 0.41 ± 0.01 | 0.02 ± 0.0 | 0.6313 | mFAP2.5 | 1.1345 ± 0.09 | 52.5356 ± 7.48 | 34.2296 ± 13.69 |
| mFAP2c.0 | 0.11 ± 0.03 | 0.33 ± 0.01 | 0.0 ± 0.0 | 0.4216 | mFAP2 | 0.12 ± 0.0 | 0.15 ± 0.01 | 0.01 ± 0.0 | 0.4332 | mFAP2.2 | 1.1470 ± 0.16 | 43.1588 ± 7.01 | 22.7242 ± 9.66 |
| mFAP_pH | 0.11 ± 0.03 | 0.41 ± 0.02 | 0.01 ± 0.0 | 0.2222 | mFAP2bL2 | 0.11 ± 0.02 | 0.01 ± 0.0 | 0.01 ± 0.0 | 0.191 | mFAP2 | 1.1470 ± 0.16 | 43.1588 ± 7.01 | 22.7242 ± 9.66 |
| mFAP2.2.16 | 0.11 ± 0.02 | 0.29 ± 0.0 | 0.01 ± 0.0 | 0.5464 | mFAP2c.1 | 0.1 ± 0.0 | 0.22 ± 0.01 | 0.01 ± 0.0 | 0.2433 | mFAP2.4 | 1.3138 ± 0.10 | 38.7414 ± 5.71 | 32.7303 ± 14.21 |
| mFAP2.2.8 | 0.1 ± 0.02 | 0.16 ± 0.03 | 0.0 ± 0.0 | 1.0 | mFAP2.2.8 | 0.1 ± 0.0 | 0.27 ± 0.01 | 0.01 ± 0.0 | 1.0 | mFAP2.5.2 | 1.3596 ± 0.17 | 40.4714 ± 4.26 | 27.7269 ± 5.72 |
| mFAP2a.0 | 0.09 ± 0.02 | 0.01 ± 0.0 | 0.0 ± 0.0 | 0.318 | mFAP2bL1 | 0.07 ± 0.02 | 0.01 ± 0.0 | 0.01 ± 0.0 | 0.2045 | mFAP2bL2 | 1.4072 ± 0.10 | N/D | N/D |
| mFAP2.1 | 0.07 ± 0.02 | 0.25 ± 0.01 | 0.01 ± 0.0 | 0.4747 | mFAP2bL4 | 0.06 ± 0.01 | 0.01 ± 0.0 | 0.01 ± 0.0 | 0.3462 | mFAP2.5.4 | 1.6382 ± 0.14 | 39.1587 ± 4.33 | 23.4552 ± 7.34 |
| mFAP2.2.17 | 0.07 ± 0.02 | 0.12 ± 0.01 | 0.0 ± 0.0 | 0.3296 | mFAP2bL3 | 0.05 ± 0.01 | 0.01 ± 0.0 | 0.01 ± 0.0 | 0.1451 | mFAP2b | 1.6678 ± 0.08 | 42.2026 ± 6.03 | 9.0088 ± 1.91 |
| mFAP0.1 | 0.06 ± 0.0 | 0.1 ± 0.01 | 0.01 ± 0.0 | 0.7885 | mFAP6 | 0.04 ± 0.01 | 0.01 ± 0.0 | 0.01 ± 0.0 | 0.3208 | mFAP2.2.5 | 1.7235 ± 0.22 | N/D | N/D |
| mFAP0.2 | 0.03 ± 0.0 | 0.06 ± 0.01 | 0.01 ± 0.0 | 0.7152 | mFAP0.1 | 0.02 ± 0.0 | 0.06 ± 0.0 | 0.02 ± 0.0 | 0.7885 | mFAP2a.0 | 1.8984 ± 0.23 | 43.2453 ± 6.34 | < 0.5 (0.0130 ± 0.02) |
| mFAP2c.1 | 0.01 ± 0.0 | 0.04 ± 0.01 | 0.0 ± 0.0 | 0.2433 | mFAP2c.9 | 0.02 ± 0.01 | 0.01 ± 0.0 | 0.01 ± 0.0 | 0.0018 | mFAP0.1 | 2.2631 ± 1.37 | 0.8514 ± 0.16 | 23.4738 ± 19.09 |
| mFAP0.3 | 0.0 ± 0.0 | 0.0 ± 0.0 | 0.01 ± 0.0 | 0.7652 | mFAP2a.1 | 0.02 ± 0.0 | 0.01 ± 0.0 | 0.01 ± 0.0 | 0.0092 | mFAP2bL5 | 2.6987 ± 0.15 | N/D | N/D |
| mFAP2c.3 | 0.0 ± 0.0 | 0.01 ± 0.0 | 0.0 ± 0.0 | 0.0217 | mFAP2c.8 | 0.02 ± 0.0 | 0.01 ± 0.0 | 0.01 ± 0.0 | 0.0273 | mFAP2.5.1 | 4.4260 ± 0.44 | 71.7430 ± 13.55 | 32.5163 ± 18.50 |
| mFAP2c.4 | 0.0 ± 0.0 | 0.0 ± 0.0 | 0.0 ± 0.0 | 0.0 | mFAP2c.3 | 0.01 ± 0.0 | 0.01 ± 0.0 | 0.01 ± 0.0 | 0.0217 | mFAP2bL1 | 4.5945 ± 0.48 | N/D | N/D |
| mFAP2a.1 | 0.0 ± 0.0 | 0.0 ± 0.0 | 0.0 ± 0.0 | 0.0092 | mFAP2c.4 | 0.01 ± 0.0 | 0.01 ± 0.0 | 0.01 ± 0.0 | 0.0 | mFAP2.5.5 | 5.5264 ± 0.59 | 66.6045 ± 12.29 | 39.1751 ± 13.38 |
| mFAP2c.8 | 0.0 ± 0.0 | 0.0 ± 0.0 | 0.0 ± 0.0 | 0.0273 | mFAP2c.10 | 0.01 ± 0.0 | 0.01 ± 0.0 | 0.01 ± 0.0 | 0.0013 | mFAP2bL3 | 5.9286 ± 0.39 | N/D | N/D |
| mFAP2c.9 | 0.0 ± 0.0 | 0.0 ± 0.0 | 0.0 ± 0.0 | 0.0018 | mFAP0.2 | 0.01 ± 0.0 | 0.04 ± 0.0 | 0.01 ± 0.0 | 0.7152 | mFAP2.5.3 | 9.4730 ± 0.72 | 91.8351 ± 20.65 | < 0.5 (0.0004 ± 0.01) |
| mFAP2c.10 | 0.0 ± 0.0 | 0.0 ± 0.0 | 0.0 ± 0.0 | 0.0013 | mFAP2c.13 | 0.01 ± 0.0 | 0.01 ± 0.0 | 0.01 ± 0.0 | 0.0015 | mFAP2bL4 | 13.0436 ± 0.82 | N/D | N/D |
| mFAP2c.11 | 0.0 ± 0.0 | 0.0 ± 0.0 | 0.0 ± 0.0 | 0.0008 | mFAP2c.11 | 0.01 ± 0.0 | 0.01 ± 0.0 | 0.01 ± 0.0 | 0.0008 | mFAP6 | 13.1430 ± 1.71 | < 0.5 (0.0023 ± 0.01) | < 0.5 (0.0001 ± 0.00) |
| mFAP2c.12 | 0.0 ± 0.0 | 0.0 ± 0.0 | 0.0 ± 0.0 | 0.0042 | mFAP2c.5 | 0.01 ± 0.0 | 0.01 ± 0.0 | 0.01 ± 0.0 | 0.0008 | mFAP8 | 58.1233 ± 8.61 | 40.5055 ± 14.87 | 48.4135 ± 31.00 |
| mFAP2c.5 | 0.0 ± 0.0 | 0.0 ± 0.0 | 0.0 ± 0.0 | 0.0008 | mFAP2c.14 | 0.0 ± 0.0 | 0.01 ± 0.0 | 0.01 ± 0.0 | 0.0013 | mFAP2c.6 | 150.1431 ± 264.69 | 98.6905 ± 65.59 | 41.6416 ± 8.08 |
| mFAP2c.13 | 0.0 ± 0.0 | 0.0 ± 0.0 | 0.0 ± 0.0 | 0.0015 | mFAP2c.6 | 0.0 ± 0.0 | 0.01 ± 0.0 | 0.01 ± 0.0 | 0.0004 | | | | |
| mFAP2c.6 | 0.0 ± 0.0 | 0.0 ± 0.0 | 0.0 ± 0.0 | 0.0004 | mFAP2c.12 | 0.0 ± 0.0 | 0.01 ± 0.0 | 0.01 ± 0.0 | 0.0042 | | | | |
| mFAP2c.14 | 0.0 ± 0.0 | 0.0 ± 0.0 | 0.0 ± 0.0 | 0.0013 | mFAP0.4 | 0.0 ± 0.0 | 0.01 ± 0.0 | 0.01 ± 0.0 | 0.0667 | | | | |
| mFAP0.4 | 0.0 ± 0.0 | 0.0 ± 0.0 | 0.0 ± 0.0 | 0.0667 | mFAP0.3 | 0.0 ± 0.0 | 0.01 ± 0.0 | 0.02 ± 0.0 | 0.7652 | | | | |

Table 2. Relative fluorescence intensities, relative expression levels, and chromophore affinities of mFAP variants

Fluorescence intensity of the deprotonated state of each chromophore at 10 μM (*left*) and 100 nM (*middle*) chromophore concentrations were measured at two purified protein volumes (25 μL and 50 μL). Fluorescence intensities were normalized from 0 to 1 across all three chromophores (DFHBI, DFHBI-1T, and DFHO) for each chromophore concentration and each protein volume, and the normalized values for the two protein volumes tested for each chromophore at each chromophore concentration were averaged and standard deviations of the mean computed. Reported values are the normalized averages and standard deviations of the means for each chromophore at each chromophore concentration in descending order of average fluorescence intensity at each chromophore concentration. Heatmap colors aid visualization of the brightest variants per chromophore concentration per chromophore relative to the brightest variant per chromophore concentration. Reported densitometry values are the relative densitometry values normalized from 0 to 1 and represent how well each design expresses relative to one another in Lemo21(DE3) *E. coli* cultures. Thermodynamic dissociation constants (*right*) are obtained by non-linear least squares fitting of fluorescence endpoint measurements normalized from 0 to 1 of chromophore titrations ($n=1$) to a single binding site isotherm equation, and K_d values reported with the standard deviation of the fit. Where the obtained K_d values are below the protein concentration tested, the K_d and standard deviation of the fit are reported in parentheses. Values with “N/D” were not determined. Heatmap colors aid visualization of the spread of K_d values per chromophore.

Using a laser scanning confocal fluorescence microscope to image *E. coli* expressing either mFAP2a or mFAP2b labeled with either DFHBI or DFHBI-1T, we observed pronounced chromophore selectivity of mFAP2b for DFHBI over DFHBI-1T, and chromophore promiscuity of mFAP2a for both DFHBI or DFHBI-1T (Figure 1f-i). *E. coli* cultures expressing either mFAP2a or mFAP2b mixed in a 1:1 cellular ratio labeled with DFHBI-1T have ~49% of the fluorescence signal as cultures labeled with DFHBI (Figure 4).

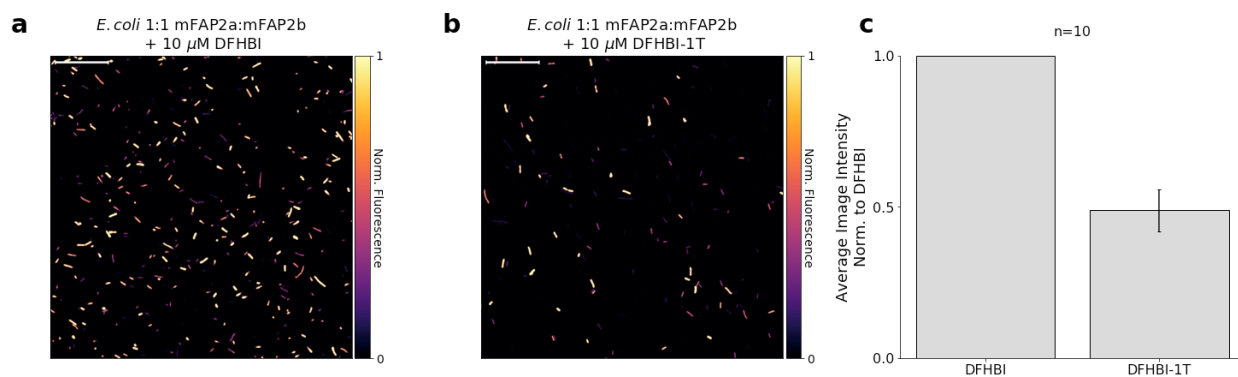


Figure 4. Laser scanning confocal fluorescence microscopy of *E. coli* expressing either mFAP2a or mFAP2b mixed in a 1:1 cellular ratio demonstrating mFAP2b selectivity for DFHBI over DFHBI-1T and mFAP2a promiscuity for DFHBI and DFHBI-1T

a,b, Representative normalized laser scanning confocal fluorescence microscopy image of *E. coli* labeled with (a) 10 μM DFHBI or (b) 10 μM DFHBI-1T. Scale bars represent 50 microns. **c**, Average (n=10) of summed pixel intensities from 10 images of *E. coli* mixtures labeled with 10 μM DFHBI or 10 images of *E. coli* mixtures labeled with 10 μM DFHBI-1T normalized to the DFHBI images. Error bars represent the standard error of the mean of summed pixel intensities over the 10 images.

We next targeted mFAP2a or mFAP2b to the endoplasmic reticulum (ER) of mammalian COS-7 cells using a C-terminal sec61β localization sequence, and observed bright fluorescence of ER under live cell widefield epifluorescence microscopy imaging after labeling with DFHBI (data not shown). Under fixed cell widefield epifluorescence microscopy imaging, following washing and re-labeling with DFHBI-1T (Figure 5), the fluorescence was altered as expected, demonstrating external spatiotemporal control over fluorescence.

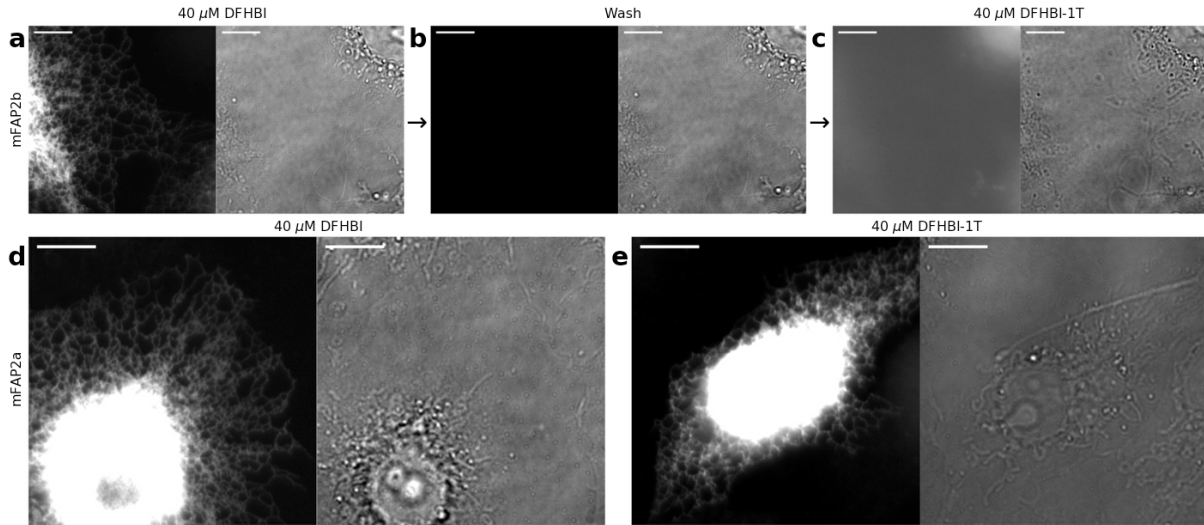


Figure 5. Widefield epifluorescence microscopy of fixed COS-7 cells with expressed mFAP2a or mFAP2b to the endoplasmic reticulum (ER) using a C-terminal sec61 β localization sequence

a-c, Images of the same region of an mFAP2b-expressing fixed COS-7 cell (**a**) labeled with 40 μ M DFHBI, (**b**) rinsed three times with 1 mL of phosphate buffered saline (PBS), then (**c**) labeled with 40 μ M DFHBI-1T for 10 minutes, demonstrating reversible on-demand fluorescence *in cyto*. **d,e**, Images of different mFAP2a-expressing fixed COS-7 cells labeled with either (**d**) 40 μ M DFHBI or (**e**) 40 μ M DFHBI-1T. **a-e**, Panels show fluorescence images (*left*) and brightfield images (*right*). Exposure times were 200 ms and current was 500 mA. Scale bars represent 10 microns.

To compare the photostability of mFAP2a and mFAP2b to an enhanced GFP (EGFP) variant, we also targeted AcGFP1 to the ER of COS-7 cells. Upon continuous wave illumination imaging at ~ 0.885 Hz (1.13 s/frame) of fixed COS-7 cells using laser scanning confocal fluorescence microscopy imaging, we found with a 50 μ M chromophore concentration a 14.5-fold, 6.8-fold, and 18.8-fold improved photostability of mFAP2a-DFHBI, mFAP2a-DFHBI-1T, and mFAP2b-DFHBI complexes over AcGFP1, respectively, and a 4.5-fold, 3.0-fold, 4.4-fold improved photostability over AcGFP1 with 500 nM chromophore concentration, respectively (Figure 6).

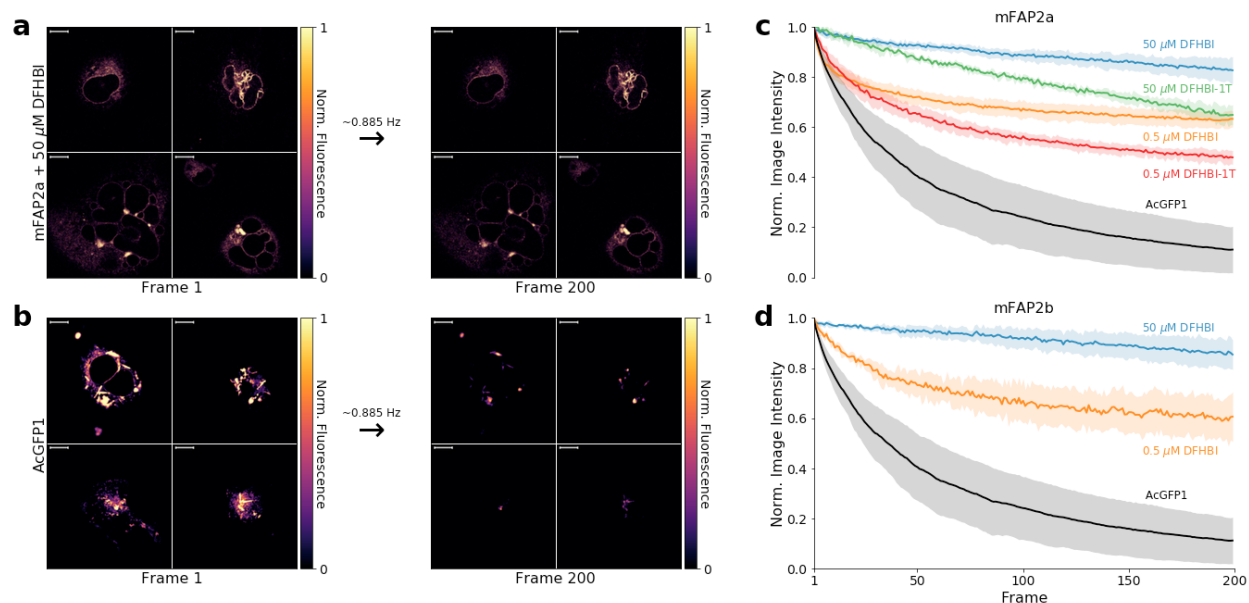


Figure 6. Photostability of mFAP2a and mFAP2b with DFHBI and DFHBI-1T compared to AcGFP1

a,b, Normalized fluorescence intensity images for four regions of interest (ROIs) acquired under continuous wave imaging at ~ 0.885 Hz (1.13 s/frame) shown for frame 1 (*left*) and frame 200 (*right*) of fixed COS-7 cells expressing endoplasmic reticulum-targeted (a) mFAP2a labeled with 50 μ M DFHBI compared to (b) AcGFP1. Scale bars represent 10 microns. **c,d,** Means (*lines*) and standard deviation of the means (*shading*) of the normalized summed pixel intensities of four ROIs ($n=4$) under continuous wave imaging for (c) mFAP2a labeled with 50 μ M DFHBI (*blue*), 0.5 μ M DFHBI (*orange*), 50 μ M DFHBI-1T (*green*), or 0.5 μ M DFHBI-1T (*red*) compared to AcGFP1 (*black*), and (d) mFAP2b labeled at 50 μ M DFHBI (*blue*) or 0.5 μ M DFHBI (*orange*) compared to AcGFP1 (*black*).

A prerequisite to designing a robust pH-responsive mFAP is its ability to bind both protonated (phenolic) DFHBI tautomers and both deprotonated (phenolate) DFHBI resonance structures (Figure 8a). When stabilized in the *cis*-planar conformation, the phenolic and phenolate forms of DFHBI exhibit blueshifted or redshifted peak excitation wavelengths, respectively²⁵ (Figure 8d). Although mFAP2 binds both the phenolic and phenolate states of DFHBI (data not shown), we screened a series of design variants based on the change in

fluorescence between pH 3.61 and pH 7.34 (Figure 7), and identified a particularly pH-responsive variant we call mFAP_pH (Figure 8b).

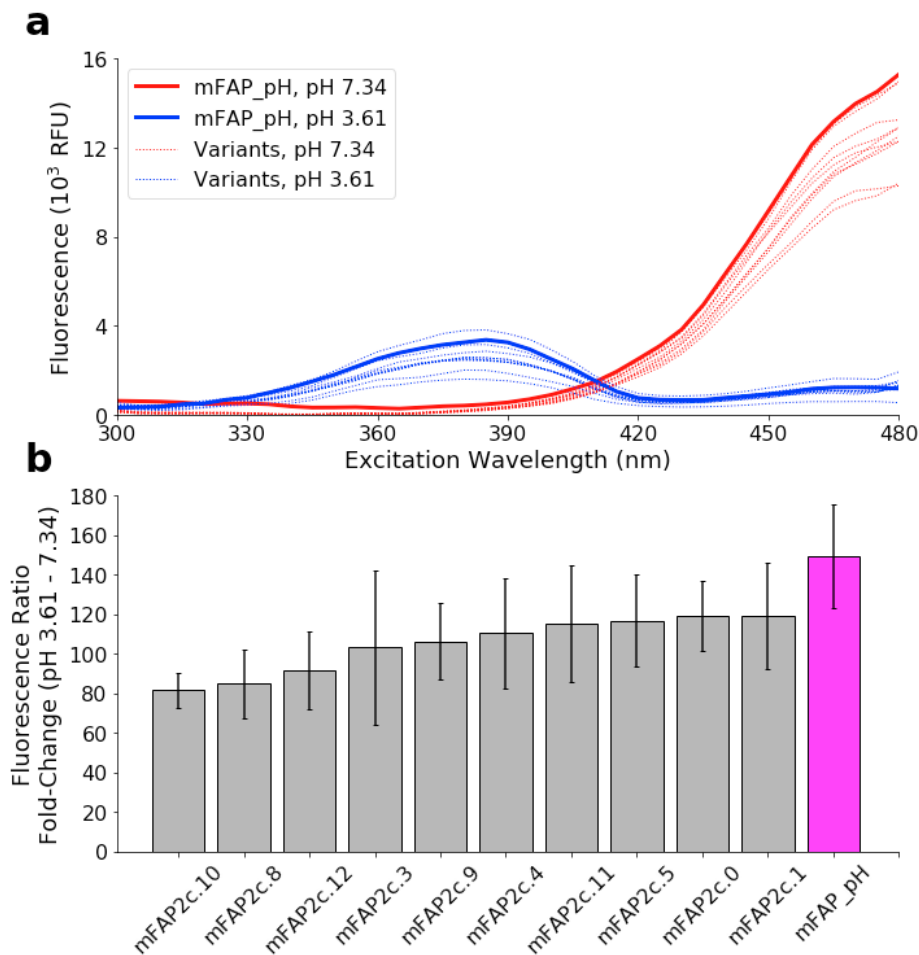


Figure 7. Photophysical characterization of pH-responsive mFAP variants

a, Fluorescence excitation spectra of selected pH-responsive mFAP variants. **b**, Average (n=3) fluorescence ratio fold-change from pH 3.61-7.34 of selected pH-responsive mFAP variants. Error bars represent the standard deviation of the mean of 3 technical replicates.

Computational models (Figure 8b,c) suggest that the additional substitutions in mFAP_pH compared to mFAP2b (i.e. W27M and W93F) improve pH-responsiveness of the protein–DFHBI complex by increasing shape complementarity toward the protonated (phenolic)

state of DFHBI via removing a hydrogen bond between the W27 indole ring and the DFHBI imidazolinone moiety, and by reducing net positive charge in the β -barrel core via removing a buried unsatisfied hydrogen bond donor in the indole ring of W93 (Figure 8f,g). The pK_a of free DFHBI in solution²¹ is ~ 5.4 , and we observe the same pK_a for the mFAP_pH–DFHBI complex (Figure 8h).

At peak excitation and emission wavelengths (Figure 8d,e), mFAP_pH showed a marked ~ 250 -fold change in ratiometric fluorescence (F_{ratio} , see Section 4.2) from pH 8.38 to pH 3.63, compared with only a ~ 34 -fold change in F_{ratio} from pH 8.38 to pH 4.79 for pHRed¹² (Figure 8i). At low pH, the β -barrel fold of mFAP_pH is more resistant to denaturation than that of pHRed, and therefore the mFAP_pH–DFHBI complex has a higher dynamic range of ratiometric fluorescence across the physiologically-relevant pH range. Ratiometric fluorescence imaging of the mFAP_pH–DFHBI complex hence enables real-time *in situ* quantification of pH (see Section 4.2).

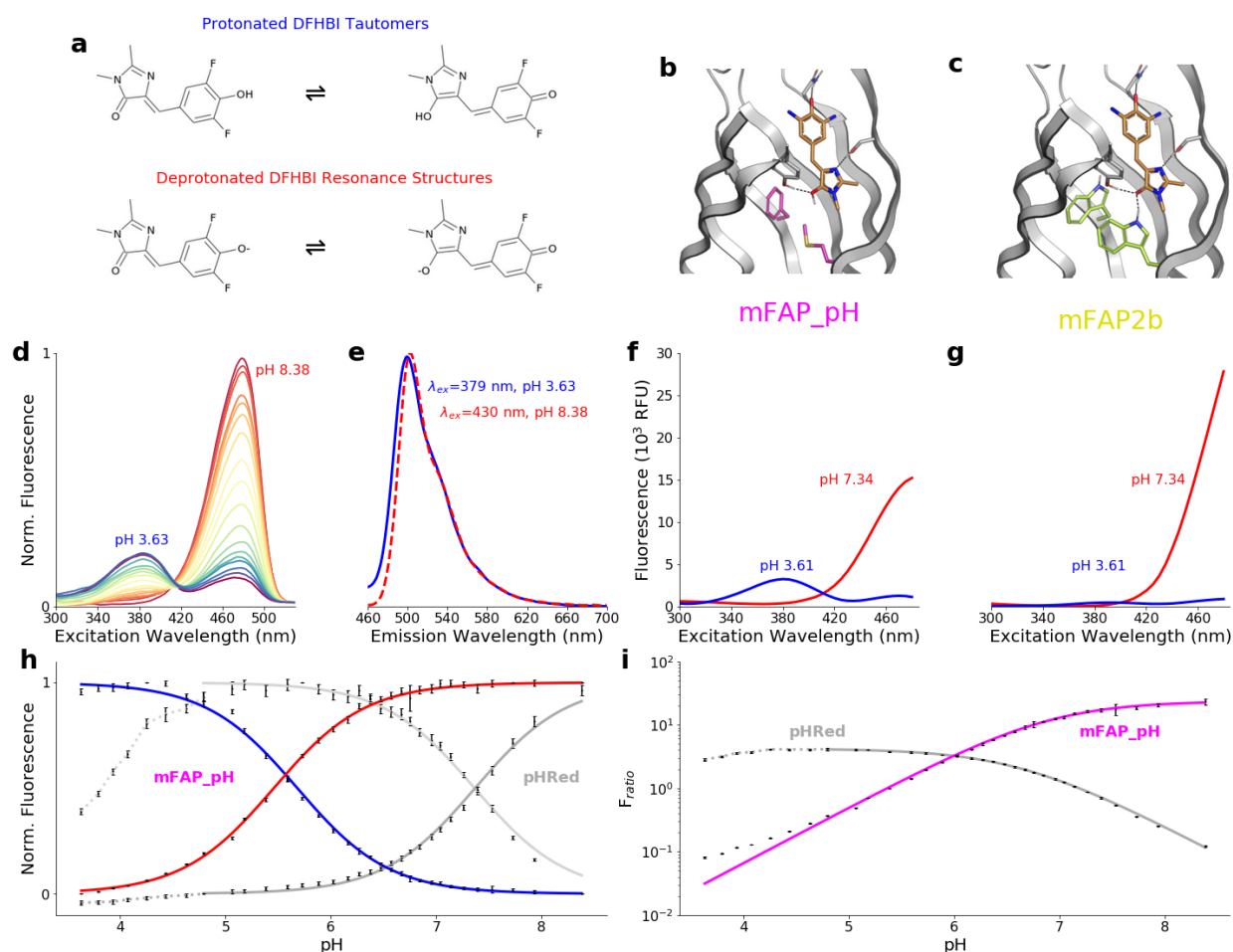


Figure 8. Characterization of pH-responsive mFAP_{pH}

a-c, Chemical basis of pH-responsiveness in mFAP_{pH}. **a**, Chemical structures of protonated tautomers and deprotonated resonance structures of DFHBI. **b,c**, Computational models showing the residues unique to **(b)** mFAP_{pH} (M27, F93) (magenta) and **(c)** mFAP2b (W27, W93) (lime). The arrangement of intermolecular hydrogen bonds (black dotted lines) in **(b)** the mFAP_{pH}-DFHBI complex permits binding to both the phenolate and phenolic (shown) states of DFHBI whereas of **(c)** the mFAP2b-DFHBI complex only permits binding to the phenolate (shown) state of DFHBI. **d**, Normalized fluorescence excitation spectra of the mFAP_{pH}-DFHBI complex for a pH titration between pH 3.63 and pH 8.38. **e**, Normalized fluorescence emission spectra of the mFAP_{pH}-DFHBI complex at pH 3.63 and pH 8.38. **f,g**, Comparison of the excitation spectra at pH 3.61 and pH 7.34 of **(f)** the pH-responsive mFAP_{pH}-DFHBI complex and **(g)** the pH-unresponsive mFAP2b-DFHBI complex. **h**, Normalized mean ($n=3$) fluorescence emission from the pH titration of the mFAP_{pH}-DFHBI complex (blue and red) and previously reported pHRed (dark grey and light grey), showing fluorescence emission by exciting the blueshifted fluorescence excitation peak (blue and dark grey) and fluorescence emission by exciting the redshifted fluorescence excitation peak (red and light grey). **i**, Ratiometric fluorescence (F_{ratio}) from the pH titration of the mFAP_{pH}-DFHBI complex (magenta) and pHRed (grey). **h,i**, The means are fit to **(h)** a sigmoid or inverse sigmoid

equation or (i) a logistic equation using non-linear least squares fitting (*lines*). The dotted lines indicate pH values at which the measured F_{ratio} coincides with two different pH values, and therefore are not used in the fittings. Error bars represent the standard deviation of the mean of 3 technical replicates.

2.3. mFAP Primary Amino Acid Sequences

| Design Name | Sequence |
|-------------|--|
| mFAP0.1 | SRAAQLLPGTWQTTMTNEDGQTSQGQMHFQPRSPYTLDVVAQGTISDGRPISGYGKVTVKTD DTLDVDITYPSLGNIKVQGQVTMDSPTQFKFDATTS DGKKLTGTLQRQE |
| mFAP0.2 | SRAAQLLPGTWQSTMTNEDGQTSQGQMHFQPRSPYTLDVVAQGTISDGRPISGYGKVTVKTD DTLDVDITYPSLGNIKVQGQVTMDSPTQFKFDATTS DGKKLTGTLQRQE |
| mFAP0.3 | SRAAQLLPGTWQVTMTNEDGQTTQGQMHFQPRSPYTLDVVAQGTISDGRPISGYGKVTVKTD DTLDVDITYPSLGNIKVQGQVTMDSPTQFKFDATTS DGKKLTGTLQRQE |
| mFAP0.4 | SRAAQLLPGTWQSTMTNEDGQTTQGQMHFQPRSPYTLDVVAQGTISDGRPISGYGKVTVKTD DTLDVDITYPSLGNIKVQGQVTMDSPTQFKFDATTS DGKKLTGTLQRQE |
| mFAP1 | SRAAQLLPGTWQVTMTNEDGQTSQGQWHFQPRSPYTLDIVAQGTISDGRPITGYGKATVKTD DTLHANLTYPSLGNIKAQQQITYDSPTQFTWNSTTSDGKKLTGTLQRQE |
| mFAP2 | SRAAQLLPGTWQVTMTNEDGQTSQGQMHFQPRSPYTM DVVAQGTISDGRPISGYGKVTVKTP DTLDVDITYPSLGNIKAQQQITMDSPTQFKFDATTKGAGNFTGRLTGTLQRQE |
| mFAP2.0.1 | SRAAQLLPGTWQVTMTNEDGQTSQGQMHFQPRSPYTM DVVSQGTISDGRPISGYGKVTVKTP DTLDVDITYPSLGNIKAQQQITMDSPTQFKFDATTKGAGNFTGRLTGTLQRQE |
| mFAP2.1 | SRAAQLLPGTWQVTMTNEDGQTSQGQMHFQPRSPYTM DVVAQGTISDGRPIVGYGKVTVKTP DTLDVDITYPSLGNIKAQQQITMDSPTQFKFDATTKGAGNFTGRLTGTLQRQE |
| mFAP2.2 | SRAAQLLPGTWQVTMTNEDGQTSQGQMHFQPRSPYTM DVVAQGTISDGRPIVGYGKVTVKTP DTLDVDITYPSLGNIKAQQQITMDSPTQFKFDATTKGAGNFTGRLTGTLQRQE |
| mFAP2.2.1 | SRAAQLLPGTWQVTMTNEDGQTSQGQMHFQPRSPYTM DVVAQGTISDGRPIVGYGKVTVKTP DTLDVDITYPSLGNIKAQQQITMDSPTQFKFDATTKGDDGFQGRLTGTLQRQE |
| mFAP2.2.10 | SRAAQLLPGTWQVTMTNEDGQTSQGQWHFQPRSPYTM DVVAQGTISDGRPIVGYGKATVKTP DTLDVDLTYPSLGNIKAQQQITMDSPTQFKWDATTKGAGNFTGRLTGTLQRQE |
| mFAP2.2.12 | SRAAQLLPGTWQVTMTNEDGQTSQGQMHFQPRSPYTM DVVAQGTISDGRPIVGYGKATVKTP DTLDVDITYPSLGNLKAQQQITMDSPTQFKFDATTKGAGNFTGRLTGTLQRQE |
| mFAP2.2.13 | SRAAQLLPGTWQVTMTNEDGQTSQGQWHFQPRSPYTM DIVAQGTISDGRPIVGYGKATVKTP DTLDVDITYPSLGNIKAQQQITMDSPTQFKWDATTKGAGNFTGRLTGTLQRQE |
| mFAP2.2.14 | SRAAQLLPGTWQVTMTNEDGQTSQGQMHFQPRSPYTM DVVAQGTISDGRPIVGYGKATVKTP DTLDVDITYPSLGNIKAQQQITMDSPTQFKFDSTTKGAGNFTGRLTGTLQRQE |

| | |
|------------|---|
| mFAP2.2.15 | SRAAQLLPGTWQVTMTNEDGQTSQGQMHFQPRSPYTMDIVAQQGTISDGRPIVGYGKATVKTP DTLDVDITYPSLGNIKAQQQITMDSPTQFKFDATTKGAGNFTGRLTGTLQRQE |
| mFAP2.2.16 | SRAAQLLPGTWQVTMTNEDGQTSQGQMHFQPRSPYTM DVVAQGTISDGRPIVGYGKATVKTP DTLDADITYPSLGNIKAQQQITMDSPTQFKFDATTKGAGNFTGRLTGTLQRQE |
| mFAP2.2.17 | SRAAQLLPGTWQVTMTNEDGQTSQGQMHFQPRSPYTM DVVAQGTISDGRPIVGYGKVTVKTP DTLDADLITYPSLGNLKAQQQITMDSPTQFKFDATTKGAGNFTGRLTGTLQRQE |
| mFAP2.2.2 | SRAAQLLPGTWQVTMTNEDGQTSQGQMHFQPRSPYTM DVVAQGTISDGRPIVGYGKVTVKTP DTLDVDITYPSLGNIKAQQQITMDSPTQFKFDATTKGEDGFQGRLTGTLQRQE |
| mFAP2.2.3 | SRAAQLLPGTWQVTMTNEDGQTSQGQMHFQPRSPYTM DVVAQGTISDGRPIVGYGKVTVKTP DTLDVDITYPSLGNIKAQQQITMDSPTQFKFDATTKGENDFVGRLTGTLQRQE |
| mFAP2.2.4 | SRAAQLLPGTWQVTMTNEDGQTSQGQMHFQPRSPYTM DVVAQGTISDGRPIVGYGKVTVKTP DTLDVDITYPSLGNIKAQQQITMDSPTQFKFDATTKGENDFQGRLTGTLQRQE |
| mFAP2.2.5 | SRAAQLLPGTWQVTMTNEDGQTSQGQMHFQPRSPYTM DVVAQGTISDGRPIVGYGKVTVKTP DTLDVDITYPSLGNIKAQQQITMDSPTQFKFDATTKGADGWHGRLTGTLQRQE |
| mFAP2.2.6 | SRAAQLLPGTWQVTMTNEDGQTSQGQMHFQPRSPYTM DVVAQGTISDGRPIVGYGKVTVKTP DTLDVDITYPSLGNIKAQQQITMDSPTQFKFDATTKGEDGWWGRLTGTLQRQE |
| mFAP2.2.7 | SRAAQLLPGTWQVTMTNEDGQTSQGQMHFQPRSPYTM DVVAQGTISDGRPIVGYGKVTVKTP DTLDVDITYPSLGNIKAQQQITMDSPTQFKFDATTKGADGWDGRLTGTLQRQE |
| mFAP2.2.8 | SRAAQLLPGTWQVTMTNEDGQTSQGQMHFQPRSPYTM DVVAQGTISDGRPIVGYGKVTVKTP DTLDVDITYPSLGNIKAQQQITMDSPTQFKFDATTKGEDDYVGRLTGTLQRQE |
| mFAP2.2.9 | SRAAQLLPGTWQVTMTNEDGQTSQGQWHFQPRSPYTM DVVAQGTISDGRPIVGYGKATVKTP DTLDVDITYPSLGNIKAQQQITMDSPTQFKWDATTKGAGNFTGRLTGTLQRQE |
| mFAP2.3 | SRAAQLLPGTWQVTMTNEDGQTSQGQMHFQPRSPYTM DVVAQGTISDGRPIVGYGKVTVKTP DTLDVDITYPSLGNIKAQQQITMDSPTQFKFDATTKGENDFHGRLTGTLQRQE |
| mFAP2.4 | SRAAQLLPGTWQVTMTNEDGQTSQGQMHFQPRSPYTM DIVAQQGTISDGRPIVGYGKATVKTP DTLDVDITYPSLGNIKAQQQITMDSPTQFKFDATTKGAGNFTGRLTGTLQRQE |
| mFAP2.5 | SRAAQLLPGTWQVTMTNEDGQTSQGQWHFQPRSPYTM DIVAQQGTISDGRPIVGYGKATVKTP DTLDVDITYPSLGNIKAQQQITMDSPTQFKWDATTKGENDFHGRLTGTLQRQE |
| mFAP2.5.1 | SRAAQLLPGTWQLTMTNEDGQTSQGQWHFQPRSPYTM DIVAQQGTISDGRPIVGYGKATVKTP DTLDVDITYPSLGNIKAQQQITMDSPTQFKWDATTKGENDFHGRLTGTLQRQE |
| mFAP2.5.2 | SRAAQLLPGTWQVTMTNEDGQTSQGQWHFQPRSPYTM DIVAQQGTISDGRPIVGYGKATVKTP DTLDVDITYPSLGNIKAQQQITMDSPTQFKWDATTKGENYFHGRLTGTLQRQE |
| mFAP2.5.3 | SRAAQLLPGTWQVTMTNEDGQTSQGQWHFQPRSPYTM DIVAQQGTISDGRPIVGYGKATVKTP DTLDDLVTYPSLGNIKAQQQITMDSPTQFKWDATTKGENDFHGRLTGTLQRQE |
| mFAP2.5.4 | SRAAQLLPGTWQATMTNEDGQTSQGQWHFQPRSPYTM DIVAQQGTISDGRPIVGYGKATVKTP DTLDVDVTYPSLGNIKAQQQITMDSPTQFKWDATTKGENDFHGRLTGTLQRQE |

| | |
|-----------|---|
| mFAP2.5.5 | SRAAQLLPGTWQITMTNEDGQTSQGQWHFQPRSPYTMDIVAQGTISDGRPIVGYGKATVKTP DTLDIDITYPSLGNIKAQQQITMDSPTQFKWDATTKGENDFHGRLTGTLQRQE |
| mFAP2a | SRAAQLLPGTWQATFTNEDGQTSQGQWHFQPRSPYTMDIVAQGTISDGRPIVGYGKATVKTP DTLDIDITYPSLGNIKAQQQITMDSPTQFKWDATTKGENDFHGRLTGTLQRQE |
| mFAP2a.0 | SRAAQLLPGTWQVFTNEDGQTSQGQWHFQPRSPYTMDIVAQGTISDGRPIVGYGKATVKTP DTLDIDITYPSLGNIKAQQQITMDSPTQFKWDATTKGENDFHGRLTGTLQRQE |
| mFAP2a.1 | SRAAQLLPGTWQGTFTNEDGQTSQGQWHFQPRSPYTMDIVAQGTISDGRPIVGYGKATVKTP DTLDIDITYPSLGNIKAQQQITMDSPTQFKWDATTKGENDFHGRLTGTLQRQE |
| mFAP2b | SRAAQLLPGTWQVTMTNEDGQTSQGQWHFQPRSPYTMDIVAQGTISDGRPIVGYGKATVKTP DTLDIDITYPSLGNIKAQQQITMDSPTQFKWDATTKGENDFHGRLTGTLQRQE |
| mFAP2c.0 | SRAAQLLPGTWQVTMTNEDGQTSQGQMHFQPRSPYTMVVVAQGTISDGRPIVGYGKATVKTP DTLDVDITYPSLGNLKAQQQITMDSPTQFKFDATTKGENDFHGRLTGTLQRQE |
| mFAP2c.1 | SRAAQLLPGTWQVTMTNEDGQTSQGQMHFQPRSPYTMDIVAQGTISDGRPIVGYGKATVKTP DTLDIDITYPSLGNIKAQQQITMDSPTQFKWDATTKGENDFHGRLTGTLQRQE |
| mFAP2c.10 | SRAAQLLPGTWQVTMTNEDGQTSQGQMHFQPRSPYTMVVVAQGTISDGRPIVGYGKATVKTP DTLDVDITYPSLGNLKAQQQITMDSPTQFKFDATTKGADGWHGRLTGTLQRQE |
| mFAP2c.11 | SRAAQLLPGTWQVTMTNEDGQTSQGQMHFQPRSPYTMDIVAQGTISDGRPIVGYGKATVKTP DTLDVDITYPSLGNIKAQQQITMDSPTQFKFDATTKGADGWHGRLTGTLQRQE |
| mFAP2c.12 | SRAAQLLPGTWQVTMTNEDGQTSQGQMHFQPRSPYTMDIVAQGTISDGRPIVGYGKATVKTP DTLDVDITYPSLGNIKAQQQITMDSPTQFKWDATTKGADGWHGRLTGTLQRQE |
| mFAP2c.13 | SRAAQLLPGTWQVTMTNEDGQTSQGQMHFQPRSPYTMDIVAQGTISDGRPIVGYGKATVKTP DTLDIDITYPSLGNIKAQQQITMDSPTQFKFDATTKGADGWHGRLTGTLQRQE |
| mFAP2c.14 | SRAAQLLPGTWQVTMTNEDGQTSQGQMHFQPRSPYTMVVVAQGTISDGRPIVGYGKATVKTP DTLDADLTYPSLGNLKAQQQITMDSPTQFKFDATTKGADGWHGRLTGTLQRQE |
| mFAP2c.3 | SRAAQLLPGTWQVTMTNEDGQTSQGQMHFQPRSPYTMDIVAQGTISDGRPIVGYGKATVKTP DTLDVDITYPSLGNIKAQQQITMDSPTQFKWDATTKGENDFHGRLTGTLQRQE |
| mFAP2c.4 | SRAAQLLPGTWQVTMTNEDGQTSQGQMHFQPRSPYTMVVVAQGTISDGRPIVGYGKATVKTP DTLDADLTYPSLGNLKAQQQITMDSPTQFKFDATTKGENDFHGRLTGTLQRQE |
| mFAP2c.5 | SRAAQLLPGTWQVTMTNEDGQTSQGQMHFQPRSPYTMDIVAQGTISDGRPIVGYGKATVKTP DTLDVDITYPSLGNIKAQQQITMDSPTQFKFDATTKGENDFHGRLTGTLQRQE |
| mFAP2c.6 | SRAAQLLPGTWQVTMTNEDGQTSQGQMHFQPRSPYTMVVVAQGTISDGRPIVGYGKATVKTP DTLDADITYPSLGNIKAQQQITMDSPTQFKFDATTKGENDFHGRLTGTLQRQE |
| mFAP2c.8 | SRAAQLLPGTWQVTMTNEDGQTSQGQMHFQPRSPYTMDIVAQGTISDGRPIVGYGKATVKTP DTLDIDITYPSLGNIKAQQQITMDSPTQFKWDATTKGADGWHGRLTGTLQRQE |
| mFAP2c.9 | SRAAQLLPGTWQVTMTNEDGQTSQGQMHFQPRSPYTMVVVAQGTISDGRPIVGYGKATVKTP DTLDADITYPSLGNIKAQQQITMDSPTQFKFDATTKGADGWHGRLTGTLQRQE |

| | |
|---------|---|
| mFAP3 | SRAAQLLPGTWQATFTNEDGQTSQGQWHFQPRSPYTMDIVAQGTISDGRPIVGYGKATVKTP DTLDIDITWPSLGNIKGQGQITMDSPTQFKWDGTTKGENDFHGRLTGTLQRQE |
| mFAP4 | SRAAQLLPGTWQATFTNEDGQTSQGQWHFQPRSPYTMDIVAQGTISDGRPIVGYGKATVKTP DTLDIDITWPSLGNIKAQGQITMDSPTQFKWDGTTKGENDFHGRLTGTLQRQE |
| mFAP5 | SRAAQLLPGTWQATFTNEDGQTSQGQWHFQPRSPYTMDIVAQGTISDGRPIVGYGKATVKTP DTLDIDITWPSLGNIKAQGQITMDSPTQFKWDATTKGENDFHGRLTGTLQRQE |
| mFAP6 | SRAAQLLPGTWQVTMTNEDGQTSQGQWHFQPRSPYTMDIVAQGTLSDGRPIVGYGKATVKTP DTLDIDITWPSLGNIKAQGQITMDSPTQFKWDATTKGENDFHGRLTGTLQRQE |
| mFAP7 | SRAAQLLPGTWQATFTNEDGQTSQGQWHFQPRSPYTMDIVAQGTISDGRPIVGYGKATVKTP DTLDIDITYPSLGNIKGQGQITMDSPTQFKWDGTTKGENDFHGRLTGTLQRQE |
| mFAP8 | SRAAQLLPGTWQATFTNEDGQTSQGQWHFQPRSPYTMDIVAQGTISDGRPIVGYGKATVKTP DTLDIDITWPSLGNIKVQGQITMDSPTQFKWDGTTKGENDFHGRLTGTLQRQE |
| mFAP_pH | SRAAQLLPGTWQVTMTNEDGQTSQGQMHFQPRSPYTMDIVAQGTISDGRPIVGYGKATVKTP DTLDIDITYPSLGNIKAQGQITMDSPTQFKFDATTKGENDFHGRLTGTLQRQE |

Chapter 3. Engineering Ca²⁺-responsive mFAPs

3.1. Introduction

In mFAPs, the chromophore binding site is close to the protein surface, which facilitates the design of environmentally responsive fluorescent reporters. In this chapter, I describe expanding the function of mFAP2a and mFAP2b designs outlined in Chapter 2 to detect analyte concentration changes, specifically Ca²⁺ ion fluxes. Ca²⁺-responsive mFAPs report changes in Ca²⁺ ion concentration via modulating the affinity for the deprotonated state of DFHBI to the mFAP biosensor. Therefore, changes in Ca²⁺ ion concentration in the environment increase or decrease the fluorescence intensity outputted from the biosensor.

3.2. Results

To enable the engineering of additional environmental responsiveness in mFAPs, we used Rosetta^{26,27} to *de novo* design 59 extensions of loops 1, 3 and 7 and screened them for fluorescence after labeling with DFHBI. We identified five extended loop7 variants that maintain the β -barrel fold and are compatible with DFHBI binding (Figure 9).

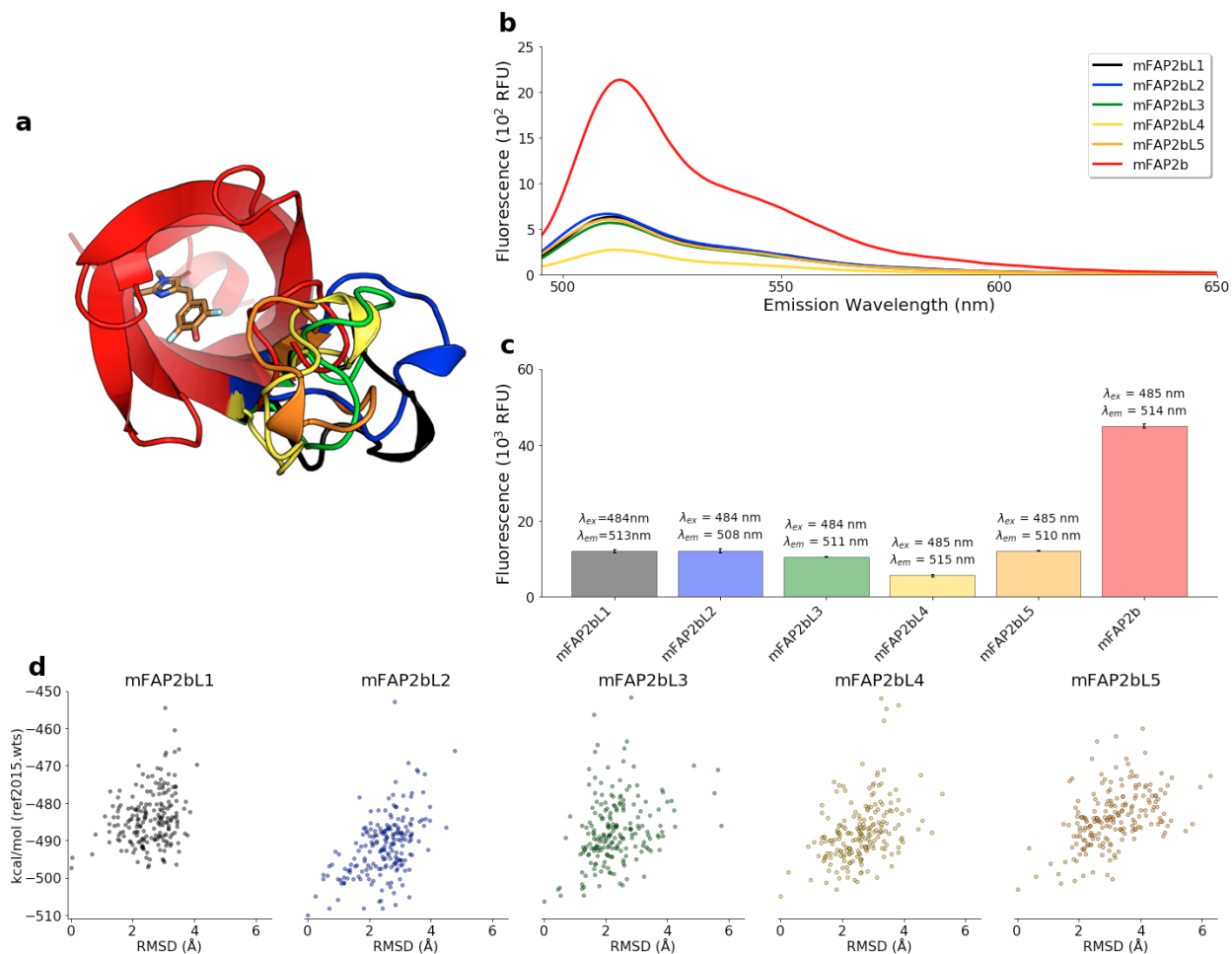


Figure 9. Photophysical characterization and computational modeling of extended loop7 variants

a, Aligned computational models of mFAP2b (*red cartoon*) and five extended loop7 variants (colored according to **b,c**) including mFAP2bL1 (*black cartoon*), mFAP2bL2 (*blue cartoon*), mFAP2bL3 (*green cartoon*), mFAP2bL4 (*yellow cartoon*), mFAP2bL5 (*orange cartoon*) with DFHBI bound (*copper sticks*). **b**, Fluorescence emission spectra from the deprotonated (phenolate) state of DFHBI labeled 10-fold below protein concentration for equimolar mFAP2b (*red*) and five extended loop7 variant designs. **c**, Average ($n=3$) fluorescence intensity from the deprotonated (phenolate) state of DFHBI labeled 10-fold below protein concentration at the indicated peak excitation and emission wavelengths for equimolar mFAP2b and five extended loop7 variants. Error bars represent the standard deviation of the mean of 3 technical replicates. **d**, Loop7 residues 95-112 of the five fluorescent extended loop7 variant design models were computationally refined using the Rosetta loopmodel application^{28,29,30,31} using 200 repeats with the “ref2015.wts” energy function⁷. For each decoy model, the root mean square distance (RMSD) of protein backbone heavy atoms to the lowest energy (kcal/mol) decoy model (shown in **a**) was computed after protein backbone C_{α} - C_{α} atom alignment.

Using these extended loop7 primary amino acid sequences as linkers (see Section 4.2), we grafted one EF-hand motif³², one EF-hand domain³³ (i.e. two EF-hand motifs), or calmodulin³⁴ (i.e. four EF-hand motifs) into loop7 of mFAP2b (Figure 10).

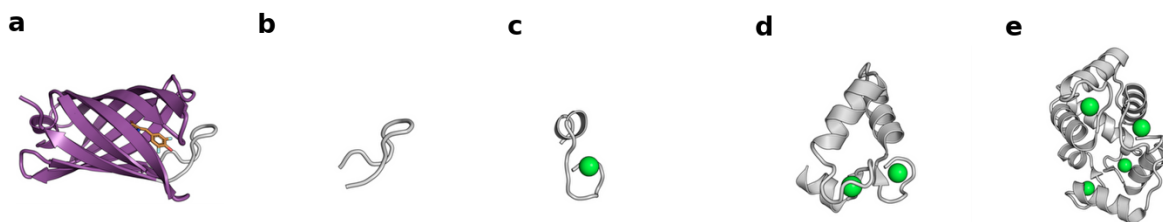


Figure 10. Structures of motifs conferring Ca²⁺-responsiveness to mFAPs

a, Computational model of *de novo* β -barrel scaffold (*purple cartoon*) showing replaceable loop7 (*grey cartoon*) with DFHBI bound (*copper sticks*). **b**, Computational model of mFAP2b loop7. **c**, Solution nuclear magnetic resonance (NMR) structure of Ca²⁺-binding peptide (*grey cartoon*) bound to one La³⁺ ion (*green sphere*) from PDB ID 1NKF³². **d**, X-ray crystal structure of *E. coli* fragment TR2C from the Ca²⁺-binding protein calmodulin (*grey cartoon*) bound to two Ca²⁺ ions (*green spheres*) from PDB ID 1FW4³³. **e**, Crystal structure of bovine brain calmodulin in a compact form (*grey cartoon*) bound to four Ca²⁺ ions (*green spheres*) from PDB ID 1PRW³⁴. (**a-e**) Models and structures are shown on different scales.

Through DFHBI and Ca²⁺ titrations, we found that Ca²⁺ binding was allosterically coupled to DFHBI binding, with either positive or negative allosteric modulation of fluorescence (Figure 11a,b,c) depending only on the amino acid sequence of the linkers. As expected based on the cooperativity of Ca²⁺ binding to calmodulin^{35,36}, we found that as the number of grafted EF-hand motifs increases, so does the affinity for Ca²⁺ (Figure 11f).

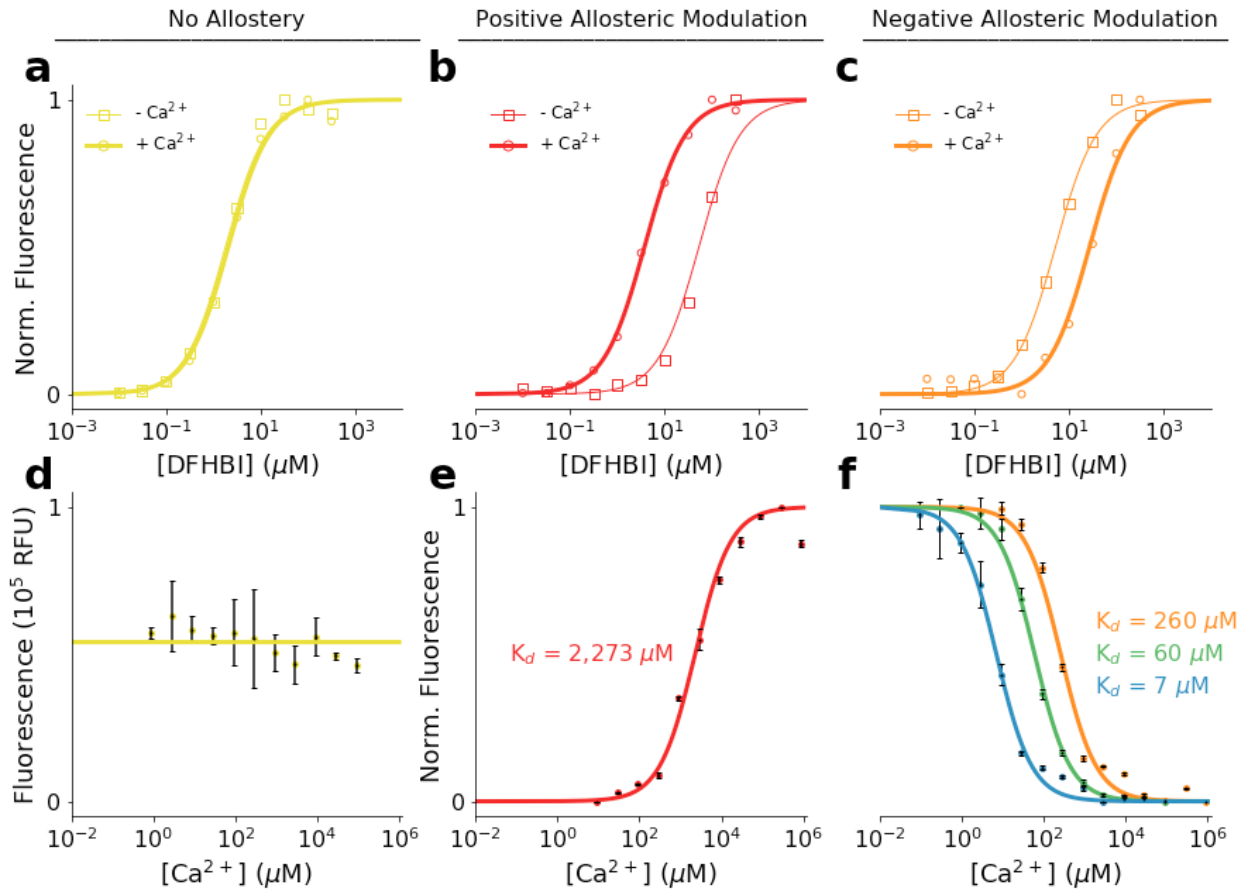


Figure 11. *In vitro* characterization of Ca^{2+} -responsive mFAPs

a-c, DFHBI titration in the absence of Ca^{2+} (*squares*) and in excess of Ca^{2+} (*circles*). **a**, mFAP2b demonstrating no allostery between Ca^{2+} and DFHBI binding. **b**, EF1p2_mFAP2b demonstrating positive allosteric modulation. **c**, EF1n_mFAP2b demonstrating negative allosteric modulation. **a-c**, Normalized fluorescence values ($n=1$) are fit to a sigmoid equation using non-linear least squares fitting (*lines*). **d-f**, Ca^{2+} titrations with excess DFHBI concentration compared to protein concentration. **d**, Unnormalized mean fluorescence intensities of mFAP2b demonstrating a lack of Ca^{2+} -responsiveness. **e**, Normalized mean fluorescence intensities of EF1p2_mFAP2b (with one EF-hand motif, $K_d = \sim 2,273 \mu\text{M}$) demonstrating positive allostery between DFHBI and Ca^{2+} binding. **f**, The fluorescence intensity across varying Ca^{2+} concentrations is dependent on the number of EF-hand motifs inserted into loop7, as exemplified by the normalized mean fluorescence intensities of EF1n_mFAP2b (with one EF-hand motif, $K_d = \sim 260 \mu\text{M}$), EF2n_mFAP2b (with two EF-hand motifs, $K_d = \sim 60 \mu\text{M}$), and EF4n_mFAP2b (with four EF-hand motifs, $K_d = \sim 7 \mu\text{M}$), demonstrating negative allostery between DFHBI and Ca^{2+} binding. **d-f**, Error bars represent the standard deviation of the mean of 3 technical replicates. The means ($n=3$) are fit to a sigmoid or inverse sigmoid equation with Hill coefficients of 1 using non-linear least squares fitting (*lines*) to obtain K_d values (Table 3).

Ca²⁺ binding nucleates α -helical secondary structure formation, presumably in the calmodulin domain, and enhances thermostability for an mFAP harboring calmodulin (Figure 12).

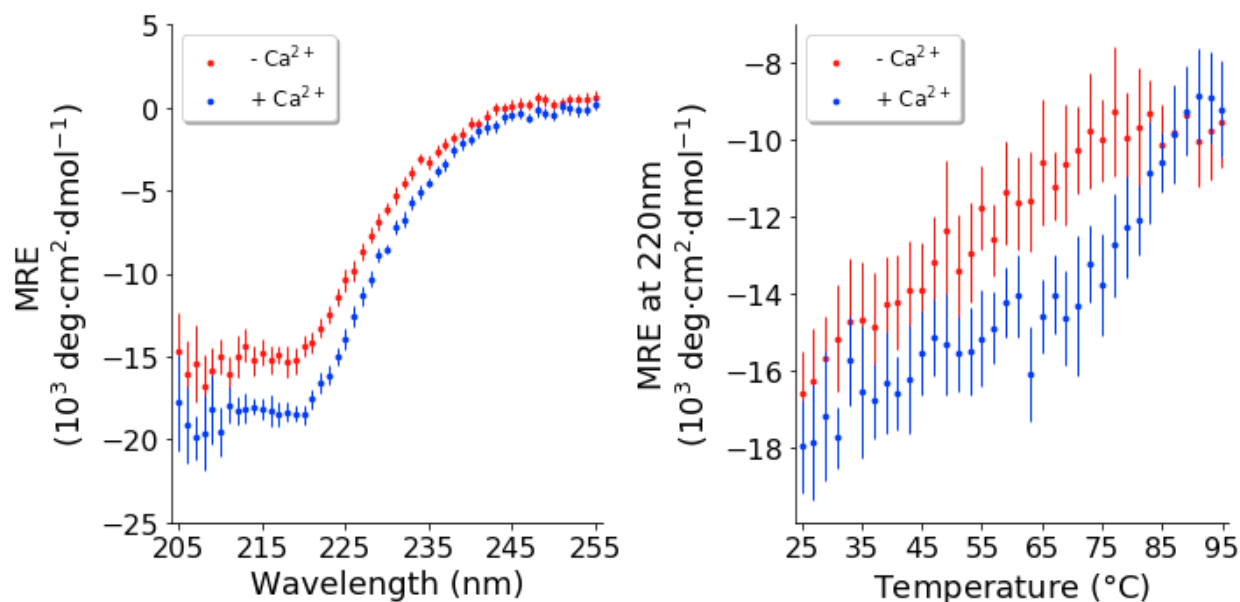


Figure 12. Far-ultraviolet (UV) circular dichroism (CD) characterization of EF4n_mFAP2b without DFHBI

a, Average ($n=1$) far-UV CD wavelength scans in either buffer only (*red*) or buffer supplemented with 100 μM CaCl₂ (*blue*). **b**, Thermal denaturation monitoring average ($n=1$) CD signal at 220 nm in either buffer only (*red*) or buffer supplemented with 100 μM CaCl₂ (*blue*). **a,b**, Reported averages are background subtracted using averages ($n=1$) at identical conditions in the absence of protein. Error bars represent the standard deviation of the mean of 3 independent measurements (**a**) per wavelength or (**b**) per $^{\circ}\text{C}$.

Incorporation of the mFAP2a hydrophobic core mutations (A13, F15) increased Ca^{2+} affinity by up to ~ 11.7 -fold for positively allosteric Ca^{2+} -responsive mFAPs and decreased Ca^{2+} affinity by up to ~ 11.6 -fold for negatively allosteric Ca^{2+} -responsive mFAPs (Figure 13, Figure 14, Figure 15, Figure 16).

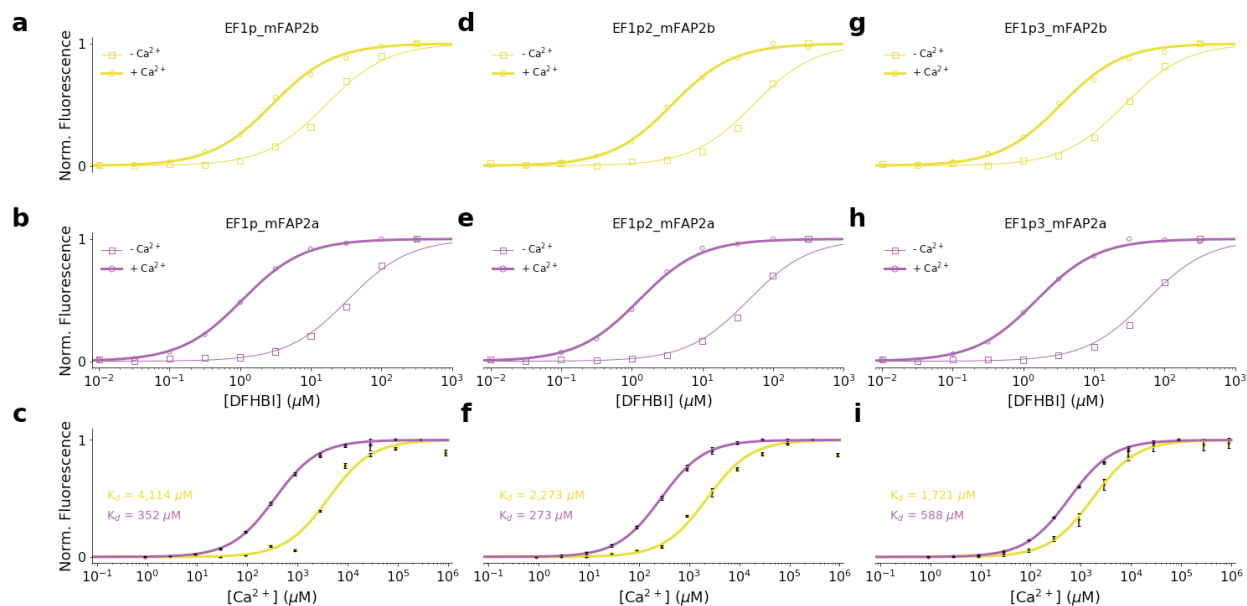


Figure 13. Normalized fluorescence intensity of positively allosteric Ca^{2+} -responsive mFAPs containing one EF-hand motif

a,b,d,e,g,h, DFHBI titrations of 500 nM sensors in buffer (*squares*) or buffer substituted with 450 mM CaCl_2 (*circles*). **c,f,i**, Ca^{2+} titrations of 500 nM sensors with 5 μM DFHBI. Error bars represent the standard deviation of the mean of 3 technical replicates. **a-i**, Non-linear least squares fitting to a single binding site isotherm equation with Hill coefficients of 1 were used to obtain K_d^- (**a,b,d,e,g,h**, *thin lines*), K_d^+ (**a,b,d,e,g,h**, *thick lines*), and Ca^{2+} K_d (**c,f,i**, *thick lines*) values (Table 3).

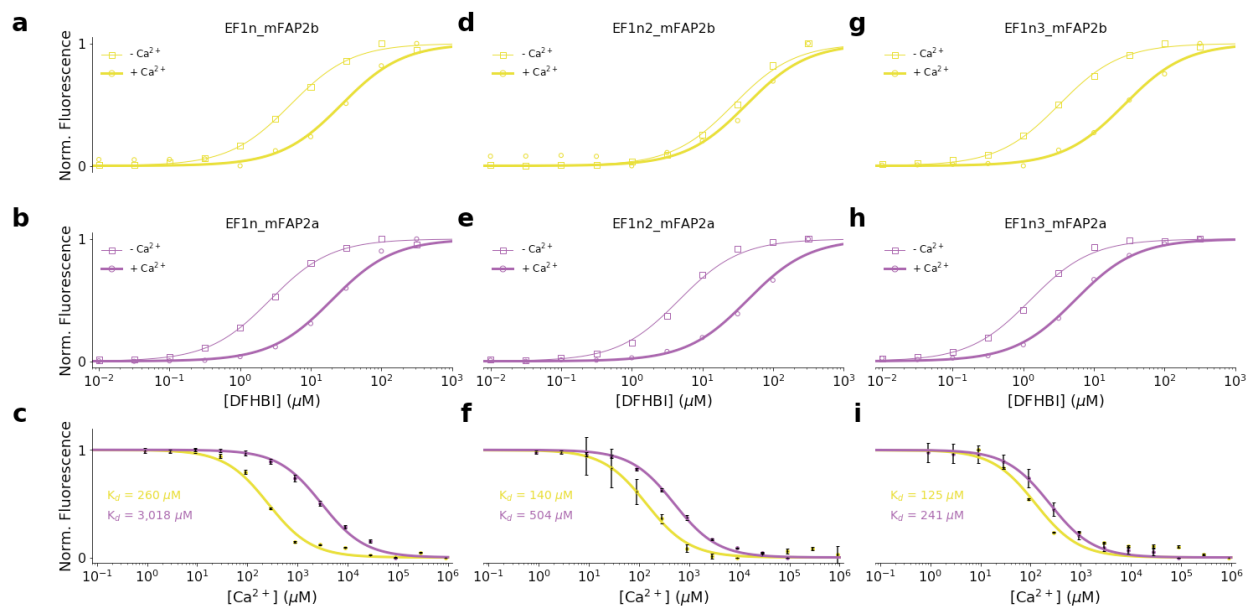


Figure 14. Normalized fluorescence intensity of negatively allosteric Ca^{2+} -responsive mFAPs containing one EF-hand motif

a,b,d,e,g,h, DFHBI titrations of 500 nM sensors in buffer (*squares*) or buffer substituted with 450 mM CaCl_2 (*circles*). **c,f,i**, Ca^{2+} titrations of 500 nM sensors with 5 μM DFHBI. Error bars represent the standard deviation of the mean of 3 technical replicates. **a-i**, Non-linear least squares fitting to (**a,b,d,e,g,h**) a single binding site isotherm equation or (**c,f,i**) an inverse single binding site isotherm equation (**a-i**) with Hill coefficients of 1 were used to obtain K_d^- (**a,b,d,e,g,h**, *thin lines*), K_d^+ (**a,b,d,e,g,h**, *thick lines*), and Ca^{2+} K_d (**c,f,i**, *thick lines*) values (Table 3).

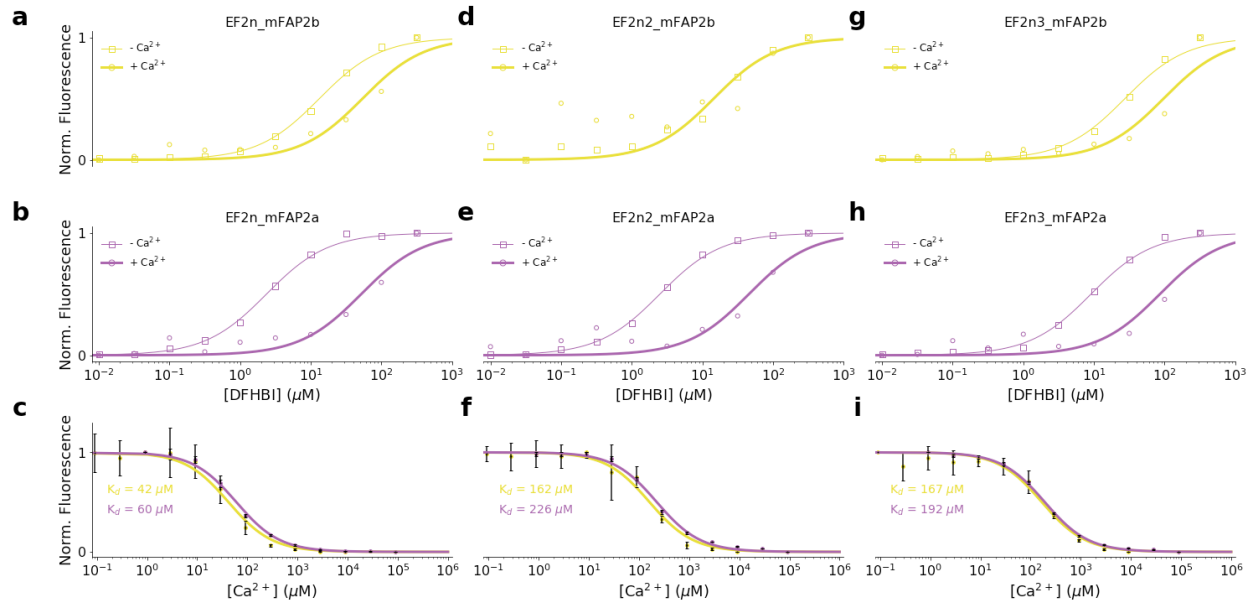


Figure 15. Normalized fluorescence intensity of negatively allosteric Ca^{2+} -responsive mFAPs containing two EF-hand motifs

a,b,d,e,g,h, DFHBI titrations of 500 nM sensors in buffer (*squares*) or buffer substituted with 450 mM CaCl_2 (*circles*). **c,f,i**, Ca^{2+} titrations of 500 nM sensors with 5 μM DFHBI. Error bars represent the standard deviation of the mean of 3 technical replicates. **a-i**, Non-linear least squares fitting to (**a,b,d,e,g,h**) a single binding site isotherm equation or (**c,f,i**) an inverse single binding site isotherm equation (**a-i**) with Hill coefficients of 1 were used to obtain K_d^- (**a,b,d,e,g,h**, *thin lines*), K_d^+ (**a,b,d,e,g,h**, *thick lines*), and Ca^{2+} K_d (**c,f,i**, *thick lines*) values (Table 3).

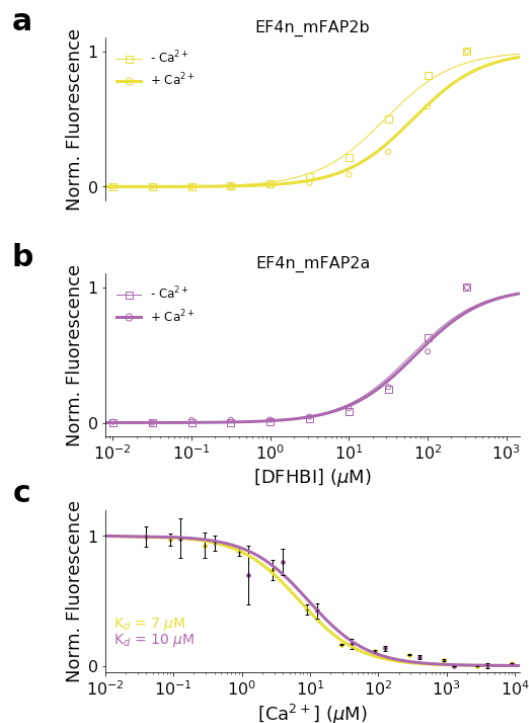


Figure 16. Normalized fluorescence intensity of negatively allosteric Ca^{2+} -responsive mFAPs containing four EF-hand motifs

a,b, DFHBI titrations of 5 μM sensors in either 500 μM EGTA (*squares*) or 500 μM CaCl_2 (*circles*). **c**, Ca^{2+} titrations of 500 nM sensors with 5 μM DFHBI. Error bars represent the standard deviation of the mean of 3 technical replicates. **c**, Ca^{2+} titrations of 6.25 μM EF4n_mFAP2b with 43.35 μM DFHBI (*lime*), and 8 μM EF4n_mFAP2a with 80 μM DFHBI (*violet*), using buffer pre-treated with Chelex 100. Error bars represent the standard deviation of the mean of 3 technical replicates. **a-c**, Non-linear least squares fitting to (**a,b**) a single binding site isotherm equation or (**c**) an inverse single binding site isotherm equation (**a-c**) with Hill coefficients of 1 were used to obtain K_d^- (**a,b**, *thin lines*), K_d^+ (**a,b**, *thick lines*), and $\text{Ca}^{2+} K_d$ (**c**, *thick lines*) values (Table 3).

The mFAP2a hydrophobic core substitutions (A13, F15) increase the affinity of DFHBI binding (Figure 1d), and titration data indicate thermodynamic coupling between Ca^{2+} and DFHBI binding (Figure 17).

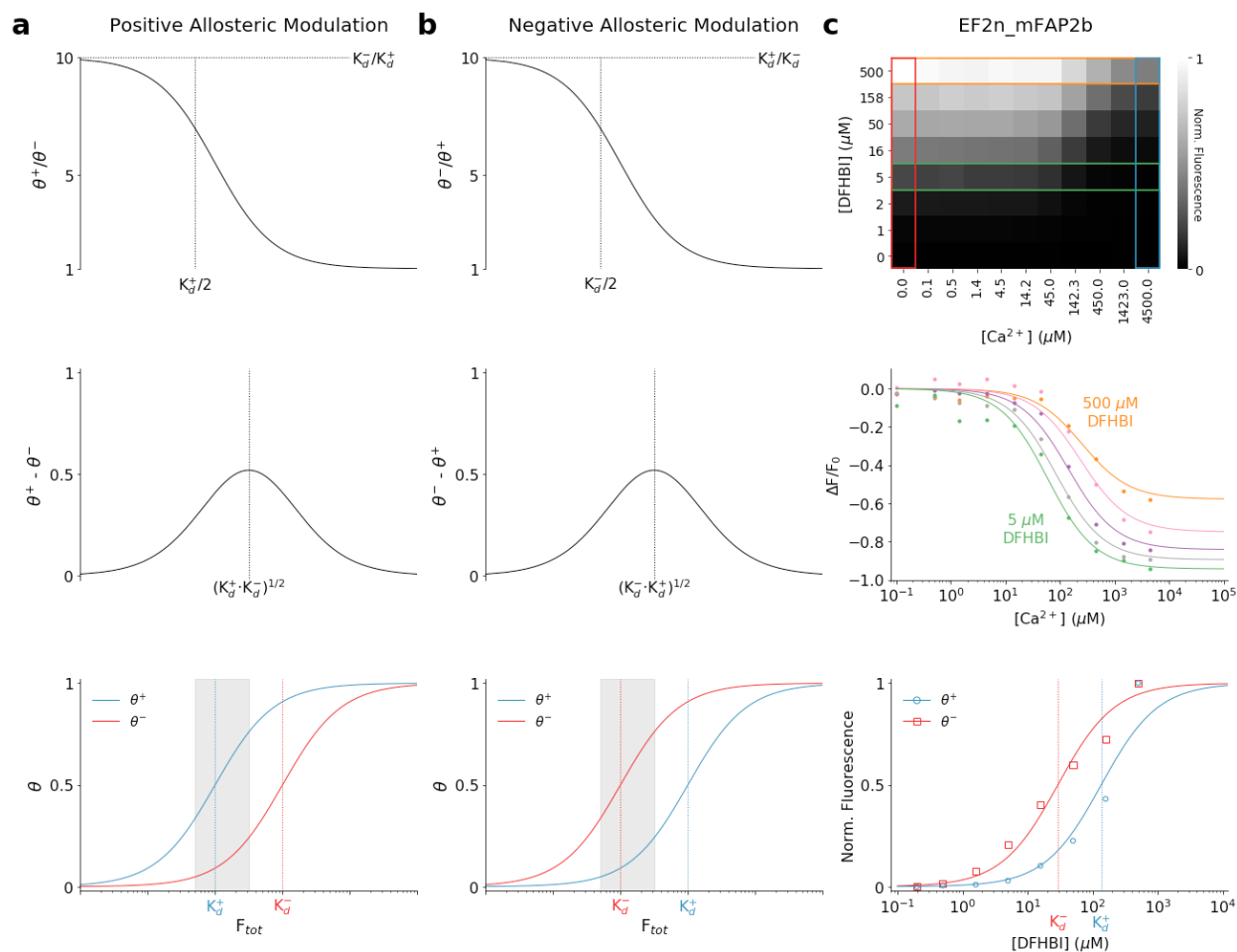


Figure 17. Theoretical thermodynamic properties of Ca²⁺-responsive mFAPs

a,b, Theoretical fraction of protein–fluorogen complex to total protein in excess Ca²⁺, θ^+ (blue), and in absence of Ca²⁺, θ^- (red), simulated with a 10-fold difference in the fluorogen thermodynamic dissociation constant in excess Ca²⁺ (K_d^+) and in the absence of Ca²⁺ (K_d^-) for (a) positive allosteric modulation and (b) negative allosteric modulation. (Top row) Theoretical dependence of the fractional change in the ratio of protein–fluorogen complex to total protein upon Ca²⁺ binding (i.e. the theoretical fluorescence dynamic range of the sensor), (a) $\frac{\theta^+}{\theta^-}$ for positive allosteric modulation or (b) $\frac{\theta^-}{\theta^+}$ for negative allosteric modulation, on the fluorogen concentration, F_{tot} . (Middle row) Theoretical dependence of the difference in the ratio of protein–fluorogen complex to total protein upon Ca²⁺ binding on the fluorogen concentration, F_{tot} . (Bottom row) Choosing F_{tot} between the range $\frac{K_d^+}{2} \leq F_{tot} \leq (K_d^+ \cdot K_d^-)^{1/2}$ for positive allosteric modulation (a, grey rectangle) or between the range $\frac{K_d^-}{2} \leq F_{tot} \leq (K_d^- \cdot K_d^+)^{1/2}$ for negative allosteric modulation (b, grey rectangle) provides a compromise in both good dynamic range and satisfactory detection sensitivity of the sensor. **c,** DFHBI titration versus Ca²⁺ titration of a negatively allosteric Ca²⁺-responsive mFAP, EF2n_mFAP2b. The heatmap (top row) represents the fluorescence intensities normalized from 0 to 1 across all DFHBI and Ca²⁺ concentrations. Normalized fluorescence intensities from the heatmap in the absence of Ca²⁺ (red

box) and in excess Ca^{2+} (*blue box*) are fit to a single binding site isotherm equation using non-linear least squares fitting (*bottom row lines*) to obtain the fluorogen thermodynamic dissociation constant in the absence of Ca^{2+} (K_d^-) and in excess Ca^{2+} (K_d^+). Unnormalized fluorescence intensities from Ca^{2+} titrations at DFHBI concentrations between 5 μM (*green box*) and 500 μM (*orange box*) from the heatmap were used to calculate the fluorescence fold-change ($\frac{\Delta F}{F_0}$) at each DFHBI concentration (*middle row*), which were then fit to an inverse single binding site isotherm equation using non-linear least squares fitting and scaled to the minimum values (*middle row lines*). The dependence of the peak magnitude of fluorescence fold-change ($\frac{\Delta F}{F_0}$) on DFHBI concentration follows the theoretical dependence of $\frac{\theta^-}{\theta^+}$ on F_{tot} for negative allosteric modulation (**b**, *top row*). Due to the thermodynamic coupling between Ca^{2+} and DFHBI binding, it is evident that the thermodynamic dissociation constant for Ca^{2+} follows the DFHBI concentration for negatively allosteric Ca^{2+} -responsive mFAPs.

We propose that the discussion of theoretical thermodynamics of analyte-dependent fluorogenic proteins as previously presented²³, applies to the suite of positively allosteric Ca^{2+} -responsive mFAPs presented herein, and we further extend this discussion to negatively allosteric analyte-dependent proteins. In the presence of excess fluorogen, the fraction of protein–fluorogen complex to total protein, θ , is given by:

$$\theta = \frac{F_{tot}}{K_d + F_{tot}}$$

where F_{tot} is the total concentration of fluorogen and K_d is the thermodynamic dissociation constant of protein–fluorogen complex. In the presence of excess analyte, one can model the fraction of protein–fluorogen complex to total protein, θ^+ , as:

$$\theta^+ = \frac{F_{tot}}{K_d^+ + F_{tot}}$$

where K_d^+ is the thermodynamic dissociation constant of protein–fluorogen complex in the presence of excess analyte. Conversely, in the absence of analyte, one can model the fraction of protein–fluorogen complex to total protein, θ^- , as:

$$\theta^- = \frac{F_{tot}}{K_d^- + F_{tot}}$$

where K_d^- is the thermodynamic dissociation constant of protein–fluorogen complex in the absence of analyte.

For positively allosteric analyte-dependent fluorogenic proteins, where analyte binding increases the affinity of fluorogen to the protein, one can characterize the fluorescence response upon analyte binding by computing the difference in protein–fluorogen complex to total protein in excess or in absence of analyte as the following:

$$\theta^+ - \theta^- = \frac{F_{tot}}{K_d^+ + F_{tot}} - \frac{F_{tot}}{K_d^- + F_{tot}}$$

For negatively allosteric analyte-dependent fluorogenic proteins, where analyte binding decreases the affinity of fluorogen to protein, one can characterize the fluorescence response upon analyte binding by computing the difference in protein–fluorogen complex to total protein in absence or in excess of analyte as the following:

$$\theta^- - \theta^+ = \frac{F_{tot}}{K_d^- + F_{tot}} - \frac{F_{tot}}{K_d^+ + F_{tot}}$$

In both positive and negative allosteric modulation, it follows that the maximum variational change in protein–fluorogen complex to total protein upon analyte binding is given by:

$$F_{tot} = (K_d^+ \cdot K_d^-)^{1/2}$$

Additionally, for positively allosteric analyte-dependent fluorogenic proteins, one can characterize the fluorescence response upon analyte binding by computing the fractional increase in protein–fluorogen complex to total protein as the following:

$$\frac{\theta^+}{\theta^-} = \frac{\frac{F_{tot}}{K_d^+ + F_{tot}}}{\frac{F_{tot}}{K_d^- + F_{tot}}}$$

Similarly, for negatively allosteric analyte-dependent fluorogenic proteins, one can characterize the fluorescence response upon analyte binding by computing the fractional decrease in protein–fluorogen complex to total protein as the following:

$$\frac{\theta^-}{\theta^+} = \frac{\frac{F_{tot}}{K_d^- + F_{tot}}}{\frac{F_{tot}}{K_d^+ + F_{tot}}}$$

For both positive and negative allosteric modulation, it follows that $\frac{\theta^+}{\theta^-}$ and $\frac{\theta^-}{\theta^+}$ are maximal at exceedingly low F_{tot} , approaching $\frac{K_d^-}{K_d^+}$ for positive allosteric modulation and $\frac{K_d^+}{K_d^-}$ for negative allosteric modulation. Furthermore, by considering the fluorescence intensities of an analyte-dependent fluorogenic protein in excess or in absence of analyte as I^+ or I^- , respectively, and brightnesses (typically given by quantum yield multiplied by extinction coefficient) in excess or in absence of analyte as B^+ or B^- , respectively, the fluorescence dynamic range of a positively allosteric analyte-dependent fluorogenic protein is given by:

$$\frac{I^+}{I^-} = \frac{B^+ \cdot \theta^+}{B^- \cdot \theta^-}$$

and the fluorescence dynamic range of a negatively allosteric analyte-dependent fluorogenic protein is given by:

$$\frac{I^-}{I^+} = \frac{B^- \cdot \theta^-}{B^+ \cdot \theta^+}$$

Therefore, the dynamic range of an analyte-dependent fluorogenic protein is directly proportional to $\frac{\theta^+}{\theta^-}$ for positive allosteric modulation and $\frac{\theta^-}{\theta^+}$ for negative allosteric modulation, which is experimentally optimized as F_{tot} decreases. However, F_{tot} must be high enough to

achieve a detectable fluorescence signal without compromising fluorescence dynamic range of the sensor. As previously proposed for positively allosteric analyte-dependent fluorogenic proteins²³, we concur that an ideal compromise to obtain both good dynamic range and satisfactory detection sensitivity is to choose F_{tot} in the range:

$$\frac{K_d^+}{2} \leq F_{tot} \leq (K_d^+ \cdot K_d^-)^{1/2}$$

We extend this suggestion, proposing that for negatively allosteric analyte-dependent fluorogenic proteins, an ideal compromise to obtain both good dynamic range and satisfactory detection sensitivity is to choose F_{tot} in the range:

$$\frac{K_d^-}{2} \leq F_{tot} \leq (K_d^- \cdot K_d^+)^{1/2}$$

The total fluorogen concentration may be tuned by the researcher according to experimental requirements. Lower fluorogen concentrations may be chosen to improve overall fluorescence dynamic range of the sensor while higher fluorogen concentrations can be selected to improve overall fluorescence signal and photostability in both the excess and absence of analyte. Experimentally determined K_d^+ and K_d^- , and computed $(K_d^+ \cdot K_d^-)^{1/2}$, for positively allosteric and negatively allosteric Ca^{2+} -responsive mFAPs are available in Table 3.

Overall, the Ca^{2+} -responsive mFAPs exhibit over 500-fold differences in affinity for Ca^{2+} ions (Table 3), enabling the choice of an mFAP biosensor with optimal fluorescence dynamic range in the anticipated Ca^{2+} concentration range under study.

| Design Name | DFHBI K_d^+ (μM) | DFHBI K_d^- (μM) | Ca^{2+} K_d (μM) | Hill Coefficient, n_H | K_d^+/K_d^- | K_d^+/K_d^- | $(K_d^+ \cdot K_d^-)^{1/2}$ (μM) | Max. $ \theta^+ - \theta^- $ (%) |
|--------------|---------------------------------|---------------------------------|--|-------------------------|---------------|---------------|---|----------------------------------|
| EF1p_mFAP2b | 2.8 ± 0.1 | 16.6 ± 1.3 | 4,114.3 ± 639.7 | 1.3 ± 0.2 | 5.8 ± 0.6 | - | 6.9 ± 0.3 | 41.5 |
| EF1p_mFAP2a | 1.1 ± 0.0 | 33.3 ± 3.2 | 352.3 ± 11.4 | 0.9 ± 0.0 | 31.2 ± 3.1 | - | 6.0 ± 0.3 | 69.6 |
| EF1p2_mFAP2b | 10.8 ± 1.1 | 34.8 ± 3.3 | 2,273.2 ± 285.3 | 0.9 ± 0.1 | 3.2 ± 0.5 | - | 19.4 ± 1.4 | 28.4 |
| EF1p2_mFAP2a | 1.3 ± 0.1 | 45.0 ± 5.3 | 272.8 ± 3.9 | 1.0 ± 0.0 | 35.5 ± 4.4 | - | 7.6 ± 0.5 | 71.3 |
| EF1p3_mFAP2b | 3.4 ± 0.2 | 27.1 ± 2.2 | 1,720.6 ± 81.1 | 1.0 ± 0.0 | 7.9 ± 0.8 | - | 9.6 ± 0.5 | 47.6 |
| EF1p3_mFAP2a | 1.5 ± 0.1 | 56.2 ± 8.0 | 588.3 ± 13.5 | 0.9 ± 0.0 | 36.5 ± 5.5 | - | 9.3 ± 0.7 | 71.6 |
| EF1n_mFAP2b | 6.9 ± 0.3 | 5.0 ± 0.3 | 259.9 ± 28.7 | 1.2 ± 0.1 | - | 1.4 ± 0.1 | 5.9 ± 0.2 | 8.0 |
| EF1n_mFAP2a | 19.9 ± 1.6 | 2.6 ± 0.1 | 3,017.6 ± 202.9 | 0.9 ± 0.0 | - | 7.5 ± 0.7 | 7.2 ± 0.3 | 46.6 |
| EF1n2_mFAP2b | 42.2 ± 8.0 | 27.6 ± 2.2 | 139.8 ± 14.2 | 1.1 ± 0.1 | - | 1.5 ± 0.3 | 34.1 ± 3.5 | 10.6 |
| EF1n2_mFAP2a | 43.6 ± 4.8 | 4.7 ± 0.3 | 504.4 ± 26.5 | 0.9 ± 0.0 | - | 9.3 ± 1.2 | 14.3 ± 0.9 | 50.7 |
| EF1n3_mFAP2b | 26.9 ± 2.2 | 3.2 ± 0.1 | 125.2 ± 78.0 | 0.8 ± 0.5 | - | 8.4 ± 0.8 | 9.3 ± 0.4 | 48.6 |
| EF1n3_mFAP2a | 5.4 ± 0.2 | 1.3 ± 0.1 | 240.9 ± 13.2 | 1.0 ± 0.0 | - | 4.3 ± 0.3 | 2.6 ± 0.1 | 35.0 |
| EF2n_mFAP2b | 38.0 ± 3.6 | 10.0 ± 0.7 | 41.9 ± 5.9 | 1.5 ± 0.1 | - | 3.8 ± 0.4 | 19.5 ± 1.1 | 32.1 |
| EF2n_mFAP2a | 51.9 ± 14.2 | 2.4 ± 0.1 | 60.0 ± 4.1 | 1.1 ± 0.1 | - | 22.0 ± 6.1 | 11.1 ± 1.6 | 64.8 |
| EF2n2_mFAP2b | 14.5 ± 9.7 | 14.6 ± 2.7 | 161.8 ± 37.8 | 1.3 ± 0.3 | - | 1.0 ± 0.7 | 14.5 ± 5.1 | 0.2 |
| EF2n2_mFAP2a | 45.7 ± 13.0 | 2.5 ± 0.1 | 225.9 ± 15.3 | 1.1 ± 0.1 | - | 18.2 ± 5.2 | 10.7 ± 1.5 | 62.0 |
| EF2n3_mFAP2b | 96.6 ± 25.1 | 27.4 ± 2.3 | 167.3 ± 25.7 | 1.1 ± 0.2 | - | 3.5 ± 1.0 | 51.4 ± 7.0 | 30.5 |
| EF2n3_mFAP2a | 85.7 ± 23.7 | 9.1 ± 0.5 | 191.5 ± 7.1 | 1.0 ± 0.0 | - | 9.4 ± 2.7 | 27.9 ± 4.0 | 50.9 |
| EF4n_mFAP2b | 65.1 ± 10.4* | 28.9 ± 2.6 [†] | 7.0 ± 0.6* | 1.0 ± 0.1 | - | 2.3 ± 0.4 | 43.4 ± 4.0 | 20.1 |
| EF4n_mFAP2a | 69.9 ± 11.8* | 62.7 ± 10.3 [†] | 9.5 ± 1.7* | 0.8 ± 0.1 | - | 1.1 ± 0.3 | 66.2 ± 7.8 | 2.7 |

Table 3. Thermodynamic properties of Ca^{2+} -responsive mFAPs

Thermodynamic dissociation constants for DFHBI in excess Ca^{2+} (K_d^+) and in the absence of Ca^{2+} (K_d^-) are computed by fitting the normalized fluorescence intensity measurements ($n=1$) from DFHBI titrations to a single binding site isotherm equation with Hill coefficient of 1 using non-linear least squares fitting, with standard deviations of the fit reported. Thermodynamic dissociation constants for Ca^{2+} in excess DFHBI ($\text{Ca}^{2+} K_d$) are computed by fitting the normalized average fluorescence intensity measurements ($n=3$) from Ca^{2+} titrations to a single binding site isotherm equation (for positively allosteric Ca^{2+} -responsive mFAPs) or to an inverse single binding site isotherm equation (for negatively allosteric Ca^{2+} -responsive mFAPs) with Hill coefficient of 1 using non-linear least squares fitting, with standard deviations of the fit reported. Hill coefficients are computed by fitting the Ca^{2+} titration normalized average fluorescence intensity measurements to a single binding site isotherm equation (for positively allosteric Ca^{2+} -responsive mFAPs) or to an inverse single binding site isotherm equation (for negatively allosteric Ca^{2+} -responsive mFAPs) with variable Hill coefficient using non-linear least squares fitting, with the standard deviation of the fit reported. For positively allosteric Ca^{2+} -responsive mFAPs K_d^-/K_d^+ is reported, for negatively allosteric Ca^{2+} -responsive mFAPs K_d^+/K_d^- is reported, and for all Ca^{2+} -responsive mFAPs $(K_d^+ \cdot K_d^-)^{1/2}$ is reported (see Figure 17). The maximum absolute values of the difference in ratio of sensor bound by DFHBI to total sensor in excess Ca^{2+} and in absence of Ca^{2+} , Max. $|\theta^+ - \theta^-|$, is reported as a percent. It is anticipated that under varying experimental conditions such as different chromophore concentrations or the presence of free competitive inhibitor ions^{37,38} known to bind EF-hand motifs (e.g. Mg^{2+} , Tb^{3+} , La^{3+}) that thermodynamic dissociation constants for DFHBI and Ca^{2+} may be altered. Therefore, characterization of the thermodynamic properties of Ca^{2+} -responsive mFAPs under various

systems of interest should be carried out. * Chelex 100 was used to pre-treat buffers. † Titrations carried out in EGTA.

To investigate the origin of the allosteric coupling between Ca^{2+} and DFHBI binding, we solved the X-ray crystal structure (Table 4) for one of the positively allosteric Ca^{2+} -responsive mFAPs harboring one EF-hand motif, EF1p2_mFAP2b, in complex with DFHBI and Ca^{2+} (Figure 18).

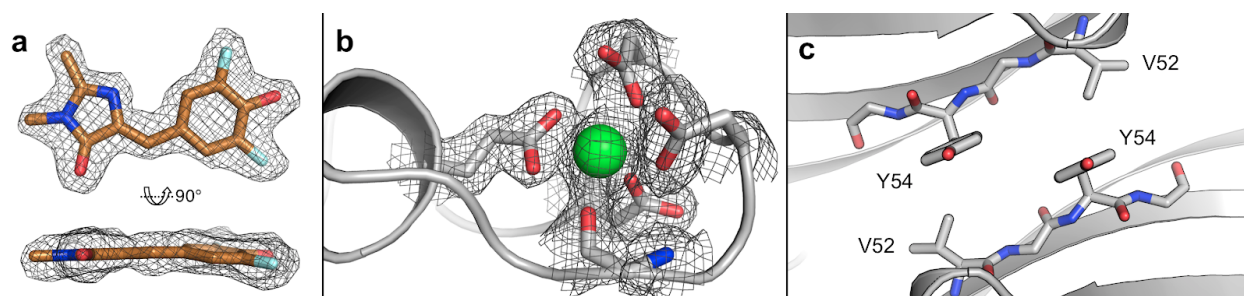


Figure 18. X-ray crystal structure of the EF1p2_mFAP2b-DFHBI- Ca^{2+} co-crystal structure solved at 2.1 Å resolution as a dimeric asymmetric unit (PDB ID 6OHH)

a, DFHBI (*copper sticks*) shown with 2Fo-Fc omit density maps indicate that DFHBI is in the *cis*-planar conformation in the co-crystal structure. **b**, Structure of grafted EF-hand motif (*grey cartoon*), bound Ca^{2+} (*green sphere*), and Ca^{2+} -coordinating residues (*grey sticks*) shown with 2Fo-Fc omit density map. **c**, Asymmetric unit dimer interface suggests that the S52V mutation (acquired from mFAP2 to mFAP2.1 and eventually carried to EF1p2_mFAP2b), and additionally Y54 present on mFAP2, mFAP2.1 and EF1p2_mFAP2b, promotes crystallization by forming hydrophobic contacts between β-barrel monomers.

| Data Collection | | Refinement | |
|----------------------|------------------|------------------------------|--------|
| Space group | P 1 21 1 | R-work | 0.1691 |
| Unit cell | | R-free | 0.2010 |
| a, b, c | 36.4, 35.6, 86.6 | Number of non-hydrogen atoms | 2,160 |
| alpha, beta, gamma | 90, 90.7, 90 | macromolecules | 1,904 |
| Wavelength (Å) | 1.54 | ligands | 38 |
| Resolution range (Å) | 50-2.1 (2.2-2.1) | water | 218 |
| Unique reflections | 13,070 | Protein residues | 254 |
| R-merge | 0.025 (0.055) | RMS(bonds) | 0.004 |
| R-meas | 0.030 (0.068) | RMS(angles) | 0.83 |
| R-pim | 0.016 (0.040) | Ramachandran favored (%) | 98.00 |
| CC1/2 | (0.996) | Ramachandran allowed (%) | 2.00 |
| I/sigma(I) | 35.2 (14.7) | Ramachandran outliers (%) | 0.00 |
| Chi ² | 0.595 | Clashscore | 4.27 |
| Multiplicity | 3.6 (2.8) | Average B-factor | 20.11 |
| Completeness (%) | 98.9 (86.2) | macromolecules | 19.33 |
| Wilson B-factor | 18.62 | ligands | 14.58 |
| | | solvent | 27.9 |

Table 4. X-ray crystallography data collection and refinement metrics for the EF1p2_mFAP2b-DFHBI-Ca²⁺ co-crystal structure (PDB ID 6OHH)

The EF1p2_mFAP2b–DFHBI–Ca²⁺ co-crystal structure (Figure 19a) revealed the residue K101 from the Ca²⁺-bound EF-hand motif directly hydrogen bonded to the hydroxybenzylidene moiety of DFHBI, providing structural insight into the allosteric coupling mechanism between DFHBI and Ca²⁺ binding (Figure 19c).

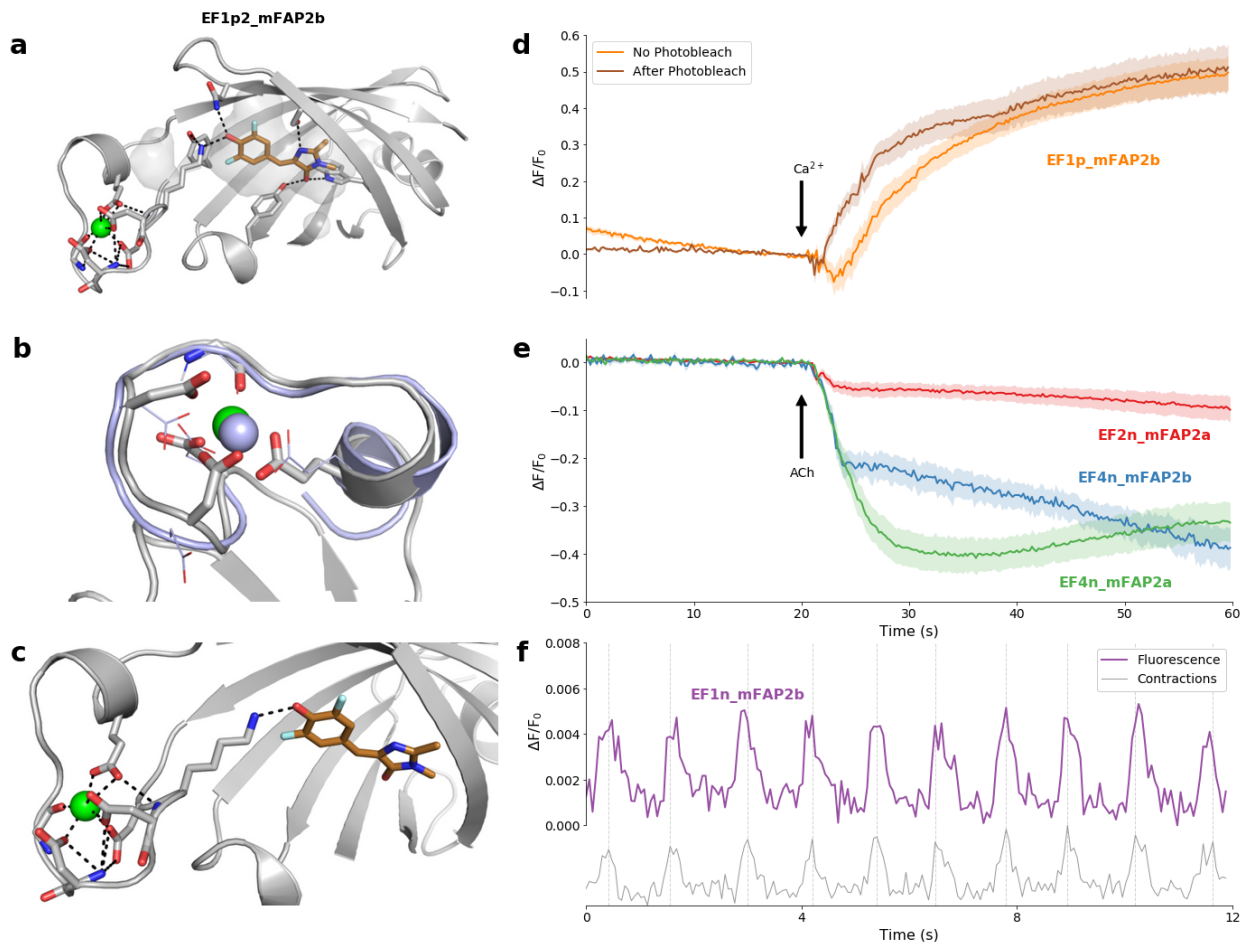


Figure 19. Structural and *in cyto* characterization of Ca²⁺-responsive mFAPs

a-c, EF1p2_mFAP2b–DFHBI–Ca²⁺ co-crystal structure at 2.1 Å resolution. The asymmetric unit is a dimer (PDB ID 6OHH). **a**, Structure of monomer with Ca²⁺ (*green sphere*) and DFHBI (*copper sticks*) bound, with protein side-chains (*grey sticks*) forming first- and second-shell hydrogen bonds with Ca²⁺ and DFHBI (*black dotted lines*), and vacuum electrostatic contact potential around DFHBI (*transparent grey surface*). **b**, The nuclear magnetic resonance (NMR) solution structure from PDB ID 1NKF (*violet cartoon and lines*) with La³⁺ bound (*violet sphere*) having the closest C_α-C_α root mean square distance (2.190 Å) to the crystal structure of the grafted EF-hand motif (*grey sticks and cartoon*) bound to Ca²⁺ ion (*green sphere*) is aligned. **c**,

Crystal structure of EF-hand motif residues (*grey sticks*) reveals that residue K101 from the EF-hand motif directly hydrogen bonds (*black dotted lines*) with DFHBI, suggesting an allosteric coupling mechanism between Ca^{2+} (*green sphere*) and DFHBI (*copper sticks*) binding. **d**, Fluorescence imaging of Ca^{2+} titrations (beginning at arrow) of live HEK293 cells expressing extracellular EF1p_mFAP2b, demonstrating positive allosterity *in cyto*. Average fluorescence fold-change (*lines*) and standard error of the mean (*shading*) is shown for regions of interest (ROIs) surrounding single cells without photobleaching (*orange*; n=15) or after photobleaching (*dark orange*; n=15). **e**, Fluorescence imaging of 100 μM acetylcholine (ACh) stimulations (added at arrow) of live HEK293 cells expressing cytosolic either EF2n_mFAP2a (*red*), EF4n_mFAP2b (*blue*), or EF4n_mFAP2a (*green*), demonstrating negative allosterity *in cyto*. Average fluorescence fold-change (*lines*) and standard error of the mean (*shading*) are shown for ROIs surrounding single cells expressing EF2n_mFAP2a (n=15), EF4n_mFAP2b (n=10), or EF4n_mFAP2a (n=15). **f**, Fluorescence imaging of live human induced pluripotent stem cell-derived cardiomyocytes expressing sarcoplasmic reticulum-targeted EF1n_mFAP2b (*violet*) labeled at 6 μM DFHBI (approximately $(K_d^+ \cdot K_d^-)^{1/2}$ for EF1n_mFAP2b, Table 3) showing the whole field of view normalized fluorescence fold-change, demonstrating negative allosterity *in cyto* and high photostability (compare to Figure 22b). The normalized average of 3 ROI traces in the fluorescence channel (*grey*) indicate peak cardiac contraction frames (*dotted lines*).

Molecular dynamics (MD) simulations starting from the X-ray crystal structure coordinates of EF1p2_mFAP2b in four conditions (apo, Ca^{2+} -bound, DFHBI-bound, and with both Ca^{2+} and DFHBI) suggest that Ca^{2+} binding to loop7 shifts the free energy landscape towards the holo (fluorescently active) conformation, even in the absence of DFHBI (Figure 20). This suggests a conformational selection^{39,40} mechanism consistent with the experimentally observed allosteric coupling of DFHBI and Ca^{2+} binding (Figure 11b,e).

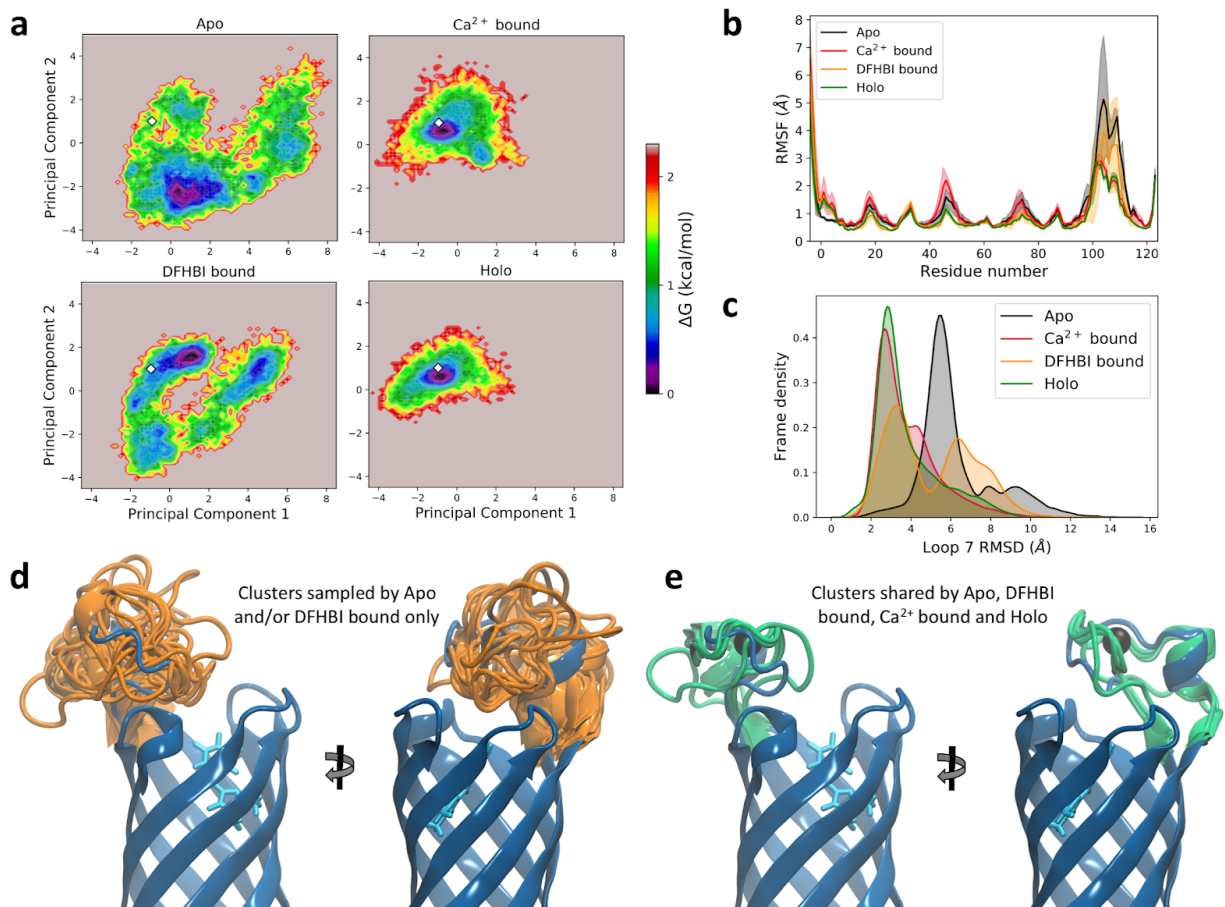


Figure 20. Molecular dynamics (MD) simulations of the X-ray crystal structure of EF1p2_mFAP2b under the four conditions: Apo, Ca²⁺-bound, DFHBI-bound, and Holo

a, Conformational free energy landscape in terms of the principal components of the protein backbone atom coordinates. The coordinates of the crystallographic structure are shown (*white diamonds*). The Ca²⁺-bound and Holo MD simulations did not divert significantly from the crystal conformation (*white diamonds*) and displayed similar conformational free energy profiles, while the Apo and DFHBI-bound systems presented a wider and shallower free energy landscape and sampled a large range of conformations with pronounced deviation from the crystal structure coordinates (*white diamonds*). **b**, Average root mean square fluctuations (RMSF) of the protein backbone C_α atoms (*lines*) and standard deviation of the means (*shaded*) of 3 replicates per condition reveals that the main source of conformational variability stems from the fluctuations of loop7. Apo and DFHBI-bound systems displayed a large degree of loop7 flexibility, whereas Ca²⁺-bound and Holo showed dampened and similar degrees of fluctuations. **c**, Smoothed histograms of the root mean square distance (RMSD) of loop7 backbone C, N and C_α atoms in the MD simulations from the crystallographic loop7 conformation. DFHBI-bound simulations, particularly, had a two-lobe RMSD distribution, in agreement with the two low-energy wells seen in the conformational free energy landscape in (**a**). **d**, Centroid structures from clusters sampled exclusively by the Apo and DFHBI-bound MD simulations (*orange cartoons*) overlaid onto the protein crystal structure (*blue cartoon*) with DFHBI (*cyan sticks*) and Ca²⁺ ion (*black*

sphere) bound. The centroid structures point to the high degree of flexibility of loop7 in the absence of Ca^{2+} . **e**, Centroids of the clusters that are sampled by all four conditions. Loop7 conformations (*green cartoons*) are overlaid onto the protein crystal structure (*blue cartoon*) with DFHBI (*cyan sticks*) and Ca^{2+} ion (*black sphere*) bound. No clusters were sampled exclusively by Ca^{2+} and Holo simulations, since the conformational ensemble of these simulations showed overlap with regions of the Apo and DFHBI-bound free energy landscape in (**a**). Thus, the clusters to which the Ca^{2+} and Holo simulations were assigned contained a minority of frames from the Apo and DFHBI-bound simulations as well. These cluster centroids showed a much more organized loop7, with smaller variations from the crystal structure atomic coordinates. **d,e**, The MD simulation conditions which did not contain Ca^{2+} bound in loop7 sampled a larger variety of conformations, which also included the active (fluorescent), Holo-like conformation to a small degree. The introduction of the Ca^{2+} ion into loop7, however, favored the fluorescently active conformation in a conformational selection manner and stabilized loop7 fluctuations.

To explore whether the Ca^{2+} -responsive mFAPs could detect Ca^{2+} ion fluxes in mammalian cells, we first expressed a positively allosteric Ca^{2+} -responsive mFAP harboring one EF-hand motif, EF1p_mFAP2b, in the extracellular matrix of HEK293 cells by fusion to an N-terminal immunoglobulin κ -chain leader sequence secretion signal, and a C-terminal transmembrane anchoring domain from platelet-derived growth factor receptor (PDGFR). To optimize detection sensitivity and photostability while compromising on fluorescence dynamic range, we chose to label HEK293 cells at 7 μM DFHBI or approximately $(K_d^+ \cdot K_d^-)^{1/2}$ for EF1p_mFAP2b, where K_d^+ and K_d^- are the DFHBI K_d for the Ca^{2+} -bound or Ca^{2+} -free sensor, respectively (Table 3). Titration of Ca^{2+} from 0 to 10 mM final concentration under constant DFHBI concentration resulted in a ~ 0.5 fluorescence fold-change ($\frac{\Delta F}{F_0}$) increase (Figure 19d). The fluorescence response is similar after photobleaching the cells, presumably due to high chromophore concentrations improving the photostability of mFAPs (Figure 6c,d).

Next, we expressed negatively allosteric Ca^{2+} -responsive mFAPs containing two or four EF-hand motifs (EF2n_mFAP2a, EF4n_mFAP2b, and EF4n_mFAP2a) in the cytosol of HEK293

cells, and stimulated Ca^{2+} release into the cytosol via endogenous muscarinic receptors¹⁵ by treatment with 100 μM acetylcholine (ACh). Ca^{2+} release into the cytosol resulted in an expected decrease in fluorescence fold-change ($\frac{\Delta F}{F_0}$) in HEK293 cells upon ACh stimulation (Figure 19e). DFHBI concentrations were at approximately $(K_d^+ \cdot K_d^-)^{1/2}$, which balances detection sensitivity and photostability against fluorescence dynamic range. Compared to the positive control fluorescent Ca^{2+} biosensor⁴¹ GCaMP6f (Figure 21), the Ca^{2+} -responsive mFAPs have less fluorescence dynamic range at the DFHBI concentrations used, but are highly photostable (Figure 19e, first 20 s).

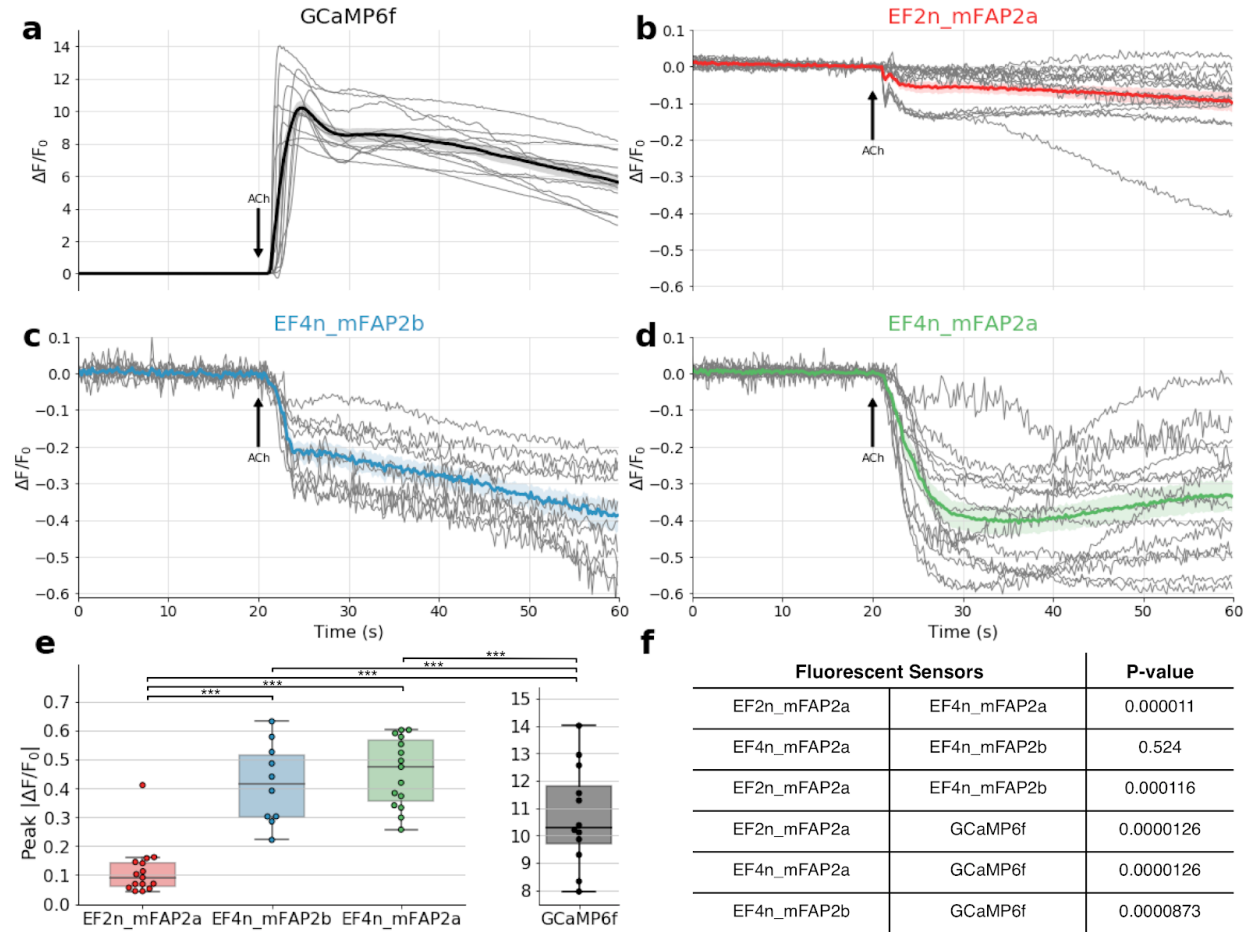


Figure 21. Time-lapse epifluorescence microscopy of acetylcholine (ACh) stimulations of live HEK293 cells expressing cytosolic Ca^{2+} -responsive mFAPs or GCaMP6f

a-d, 100 μM ACh was added (*black arrows*) and regions of interest (ROIs) surrounding single cells were analyzed for fluorescence fold-change ($\frac{\Delta F}{F_0}$) for either (**a**) GCaMP6f (n=12), (**b**) EF2n_mFAP2a (n=15) labeled at 20 μM DFHBI, (**c**) EF4n_mFAP2b (n=10) labeled at 43.3 μM DFHBI, or (**d**) EF4n_mFAP2a (n=15) 43.3 μM DFHBI. The mean $\frac{\Delta F}{F_0}$ (*thick lines*) and standard error of the mean (*shading*) are shown for the ROIs (*grey lines*). **e**, For each ROI in (**a-d**), the peak absolute value of the fluorescence fold-change upon ACh stimulation is plotted showing: center line, median; box limits, upper and lower quartiles; whiskers, distribution excluding outliers; points, peak absolute values of the fluorescence fold-change upon ACh stimulation. The two-sided Wilcoxon rank sum test was used to statistically compare groups (***) denotes P-value < 0.001). **f**, P-values between groups in (**e**).

As the fluorescence of negatively allosteric Ca^{2+} -responsive mFAPs increases when the Ca^{2+} concentration decreases, they allow reporting Ca^{2+} effluxes from compartments as increases

in fluorescence signal, whereas existing Ca^{2+} -responsive fluorescent protein sensors report Ca^{2+} effluxes as decreases in fluorescence signal^{17,42}. We expressed a negatively allosteric Ca^{2+} -responsive mFAP containing one EF-hand motif, EF1n_mFAP2b, in the sarcoplasmic reticulum (SR) of cultured human induced pluripotent stem cell (hiPSC)-derived cardiomyocytes (CMs). To optimize photostability while compromising on fluorescence fold-change, we chose to label CMs with a DFHBI concentration at approximately $(K_d^+ \cdot K_d^-)^{1/2}$ for EF1n_mFAP2b (Table 3). Ca^{2+} transients in the SR during the cardiac contraction cycling were detectable with high photostability (Figure 19f). Labeling CMs with DFHBI concentrations at approximately $\frac{K_d^-}{2}$ for EF1n_mFAP2b (Table 3) for optimal fluorescence fold-change while compromising on detection sensitivity and photostability resulted in robustly detectable Ca^{2+} transients during cardiac contraction cycling and moderate photostability using ~3-fold higher laser power density (Figure 22b). Inhibition of Ca^{2+} reuptake into the SR by treatment with 20 μM cyclopiazonic acid (CPA) resulted in a sustained increase in fluorescence fold-change ($\frac{\Delta F}{F_0}$) in the SR consistent with inhibition of SERCA pumps^{43,17} (Figure 22c).

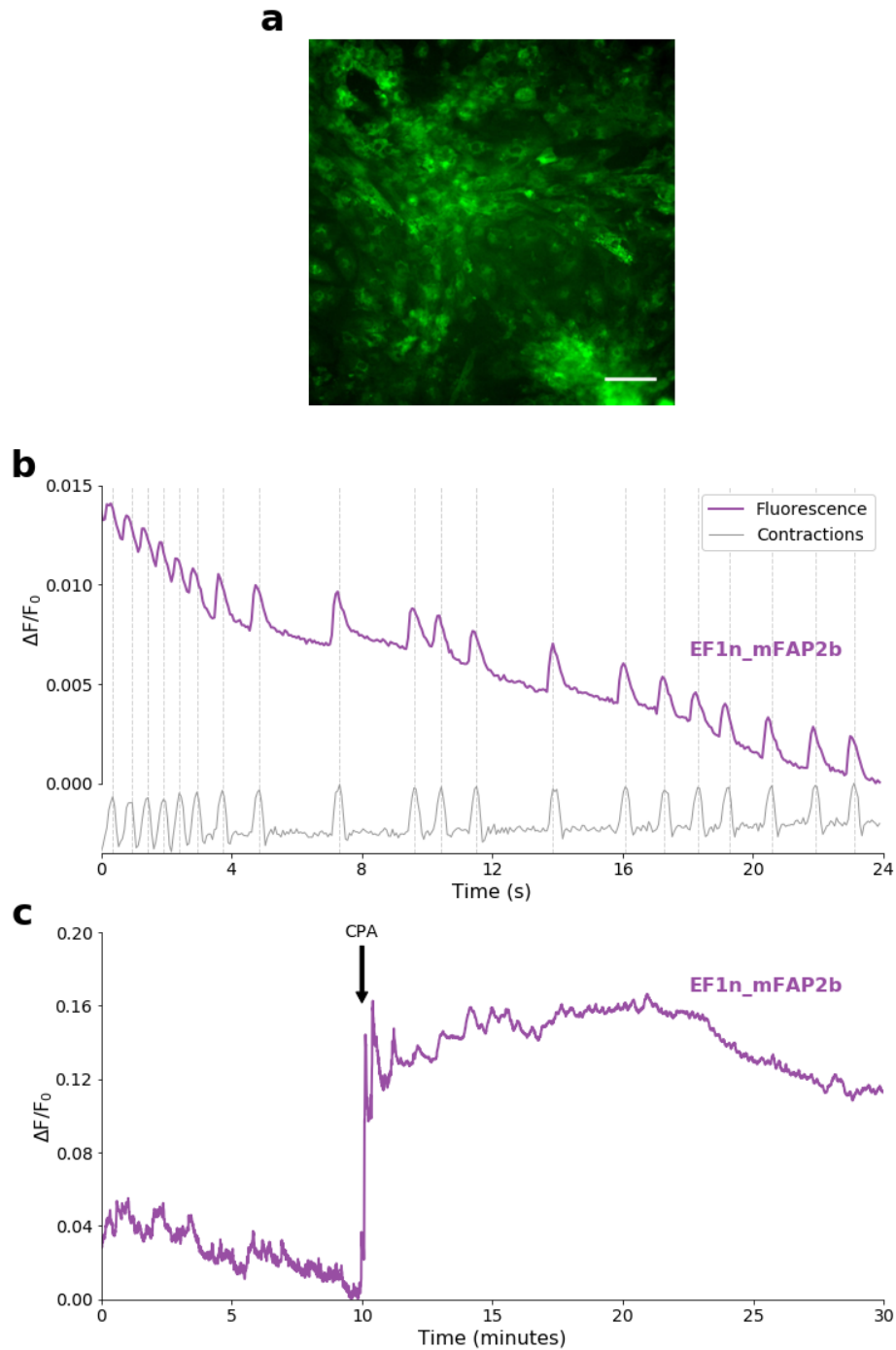


Figure 22. Time-lapse epifluorescence microscopy of human induced pluripotent stem cell (hiPSC)-derived cardiomyocytes (CMs) expressing sarcoplasmic reticulum (SR)-targeted EF1n_mFAP2b

a, Pseudo-colored maximum intensity z-axis projection from **(b)** of hiPSC-derived CMs expressing SR-targeted EF1n_mFAP2b. Scale bar represents 50 microns. **b**, Fluorescence imaging of live hiPSC-derived CMs expressing SR-targeted EF1n_mFAP2b (*violet*) labeled at 3

μM DFHBI (approximately $\frac{K_d^-}{2}$ for EF1n_mFAP2b, Table 3) imaged at ~ 16.7 Hz for 24 s showing whole field of view normalized fluorescence fold-change, demonstrating negative allostery *in cyto* and moderate photostability (compare to Figure 19f). The normalized average of 3 ROI traces in the fluorescence channel (*grey*) indicate peak cardiac contraction frames (*dotted lines*). **c**, Time-lapse epifluorescence microscopy imaging of hiPSC CMs expressing SR-targeted EF1n_mFAP2b labeled at $3 \mu\text{M}$ DFHBI imaged at 2 Hz for 30 minutes. $40 \mu\text{M}$ cyclopiazonic acid (CPA) was added (*black arrow*) which inhibits SERCA Ca^{2+} pumps blocking Ca^{2+} recovery into the SR. The negatively allosteric thermodynamic coupling between Ca^{2+} and DFHBI binding for SR-targeted EF1n_mFAP2b results in sustained fluorescence fold-change ($\frac{\Delta F}{F_0}$) increase upon CPA treatment via Ca^{2+} depletion from the SR.

EF1n_mFAP2b is the first Ca^{2+} -responsive fluorescent protein sensor that we are aware of displaying an increase in fluorescence intensity upon Ca^{2+} efflux from the SR in hiPSC-derived CMs (Figure 23).

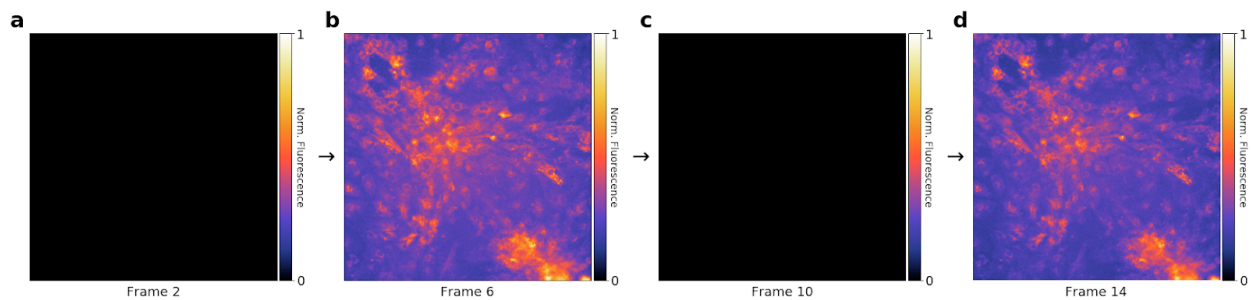


Figure 23. Processing time-lapse epifluorescence microscopy images of human induced pluripotent stem cell (hiPSC)-derived cardiomyocyte (CM) cells expressing sarcoplasmic reticulum (SR)-targeted EF1n_mFAP2b

a-d, The average fluorescence pixel intensity per frame (from Figure 22b) was computed, and the baseline of the average fluorescence pixel intensities approximated by iteratively fitting the baseline to a polynomial of degree 20. The approximate baseline average fluorescence pixel intensity per frame was subtracted from the average fluorescence pixel intensity per frame to compensate for photobleaching, then the baseline-subtracted average fluorescence pixel intensities were normalized across all frames scaling the minimum peak baseline-subtracted average fluorescence pixel intensity to 1 and the maximum trough baseline-subtracted average fluorescence pixel intensity to 0. Raw fluorescence pixel intensities (from Figure 22b) within each frame were normalized from 0 to 1, then re-scaled proportionally to the baseline-subtracted normalized average fluorescence pixel intensity, then pseudo-colored to show normalized fluorescence. The field of view contained 100% confluent cells, so regions without apparent

hiPSC-derived CM cells represent out-of-focus cellular SR fluorescence. **(a)** Frame 2, **(b)** frame 6, **(c)** frame 10, and **(d)** frame 14 **(a-d)** showing normalized fluorescence as a demonstration of Ca²⁺ ion transient reporting in the SR of hiPSC-derived CM cells imaged at 60 ms per frame.

3.3. Extended Loop7 mFAP and Ca²⁺-responsive mFAP Primary Amino Acid Sequences

| Design Name | Sequence |
|--------------|---|
| mFAP2bL1 | SRAAQLLPGTWQVTMTNEDGQTSQGQWHFQPRSPYTMDIVAQTISDGRPIVGYGKATVK TPDTLDIDITYPSLGNIKAQQQITMDSPTQFKWDAQFKQNDNPRYHGSTNILTGTLQRQE |
| mFAP2bL2 | SRAAQLLPGTWQVTMTNEDGQTSQGQWHFQPRSPYTMDIVAQTISDGRPIVGYGKATVK TPDTLDIDITYPSLGNIKAQQQITMDSPTQFKWDAHVKSNDSPLSGNTKILTGTLQRQE |
| mFAP2bL3 | SRAAQLLPGTWQVTMTNEDGQTSQGQWHFQPRSPYTMDIVAQTISDGRPIVGYGKATVK TPDTLDIDITYPSLGNIKAQQQITMDSPTQFKWDAQFKKDDDPYHGSTHILTGTLQRQE |
| mFAP2bL4 | SRAAQLLPGTWQVTMTNEDGQTSQGQWHFQPRSPYTMDIVAQTISDGRPIVGYGKATVK TPDTLDIDITYPSLGNIKAQQQITMDSPTQFKWDAEYKKNDDPRLKGSKSILTGTLQRQE |
| mFAP2bL5 | SRAAQLLPGTWQVTMTNEDGQTSQGQWHFQPRSPYTMDIVAQTISDGRPIVGYGKATVK TPDTLDIDITYPSLGNIKAQQQITMDSPTQFKWDAHYKTNDYPSLNGSKSILTGTLQRQE |
| EF1p_mFAP2b | SRAAQLLPGTWQVTMTNEDGQTSQGQWHFQPRSPYTMDIVAQTISDGRPIVGYGKATVK TPDTLDIDITYPSLGNIKAQQQITMDSPTQFKWDAHYKGDKDGDIISAAEAAAQILTGT LQRQE |
| EF1p_mFAP2a | SRAAQLLPGTWQATFTNEDGQTSQGQWHFQPRSPYTMDIVAQTISDGRPIVGYGKATVK TPDTLDIDITYPSLGNIKAQQQITMDSPTQFKWDAHYKGDKDGDIISAAEAAAQILTGT LQRQE |
| EF1p2_mFAP2b | SRAAQLLPGTWQVTMTNEDGQTSQGQWHFQPRSPYTMDIVAQTISDGRPIVGYGKATVK TPDTLDIDITYPSLGNIKAQQQITMDSPTQFKWDAHYKGDKDGDIISAAEAAAQGLTGT LQRQE |
| EF1p2_mFAP2a | SRAAQLLPGTWQATFTNEDGQTSQGQWHFQPRSPYTMDIVAQTISDGRPIVGYGKATVK TPDTLDIDITYPSLGNIKAQQQITMDSPTQFKWDAHYKGDKDGDIISAAEAAAQGLTGT LQRQE |
| EF1p3_mFAP2b | SRAAQLLPGTWQVTMTNEDGQTSQGQWHFQPRSPYTMDIVAQTISDGRPIVGYGKATVK TPDTLDIDITYPSLGNIKAQQQITMDSPTQFKWDAEYKGDKDGDIISAAEAAAQILTGT LQRQE |
| EF1p3_mFAP2a | SRAAQLLPGTWQATFTNEDGQTSQGQWHFQPRSPYTMDIVAQTISDGRPIVGYGKATVK TPDTLDIDITYPSLGNIKAQQQITMDSPTQFKWDAEYKGDKDGDIISAAEAAAQILTGT LQRQE |
| EF1n_mFAP2b | SRAAQLLPGTWQVTMTNEDGQTSQGQWHFQPRSPYTMDIVAQTISDGRPIVGYGKATVK TPDTLDIDITYPSLGNIKAQQQITMDSPTQFKWDAHVDKDGDIISAAEAAAQTKILTGT LQRQE |

| | |
|--------------|---|
| EF1n_mFAP2a | SRAAQLLPGTWQATFTNEDGQTSQGQWHFQPRSPYTMDIVAQGTISDGRPIVGYGKATVK TPDTLDIDITYPSLGNIKAQQQITMDSPTQFKWDAHVDKDG DGYISAAEAAAQTKILTGT LQRQE |
| EF1n2_mFAP2b | SRAAQLLPGTWQVTMTNEDGQTSQGQWHFQPRSPYTMDIVAQGTISDGRPIVGYGKATVK TPDTLDIDITYPSLGNIKAQQQITMDSPTQFKWDAHVDKDG DGYISAAEAAAQPHILTGT LQRQE |
| EF1n2_mFAP2a | SRAAQLLPGTWQATFTNEDGQTSQGQWHFQPRSPYTMDIVAQGTISDGRPIVGYGKATVK TPDTLDIDITYPSLGNIKAQQQITMDSPTQFKWDAHVDKDG DGYISAAEAAAQPHILTGT LQRQE |
| EF1n3_mFAP2b | SRAAQLLPGTWQVTMTNEDGQTSQGQWHFQPRSPYTMDIVAQGTISDGRPIVGYGKATVK TPDTLDIDITYPSLGNIKAQQQITMDSPTQFKWDAHVDKDG DGYISAAEAAAQPRLTGTL QRQE |
| EF1n3_mFAP2a | SRAAQLLPGTWQATFTNEDGQTSQGQWHFQPRSPYTMDIVAQGTISDGRPIVGYGKATVK TPDTLDIDITYPSLGNIKAQQQITMDSPTQFKWDAHVDKDG DGYISAAEAAAQPRLTGTL QRQE |
| EF2n_mFAP2b | SRAAQLLPGTWQVTMTNEDGQTSQGQWHFQPRSPYTMDIVAQGTISDGRPIVGYGKATVK TPDTLDIDITYPSLGNIKAQQQITMDSPTQFKWDAHVDKDG NGYISAAELRHVMTNLGEK LTDEEVDEMIREADIDGDGQVNYEEFVQMPRLTGT LQRQE |
| EF2n_mFAP2a | SRAAQLLPGTWQATFTNEDGQTSQGQWHFQPRSPYTMDIVAQGTISDGRPIVGYGKATVK TPDTLDIDITYPSLGNIKAQQQITMDSPTQFKWDAHVDKDG NGYISAAELRHVMTNLGEK LTDEEVDEMIREADIDGDGQVNYEEFVQMPRLTGT LQRQE |
| EF2n2_mFAP2b | SRAAQLLPGTWQVTMTNEDGQTSQGQWHFQPRSPYTMDIVAQGTISDGRPIVGYGKATVK TPDTLDIDITYPSLGNIKAQQQITMDSPTQFKWDAHVDKDG NGYISAAELRHVMTNLGEK LTDEEVDEMIREADIDGDGQVNAEEFVQMPRLTGT LQRQE |
| EF2n2_mFAP2a | SRAAQLLPGTWQATFTNEDGQTSQGQWHFQPRSPYTMDIVAQGTISDGRPIVGYGKATVK TPDTLDIDITYPSLGNIKAQQQITMDSPTQFKWDAHVDKDG NGYISAAELRHVMTNLGEK LTDEEVDEMIREADIDGDGQVNAEEFVQMPRLTGT LQRQE |
| EF2n3_mFAP2b | SRAAQLLPGTWQVTMTNEDGQTSQGQWHFQPRSPYTMDIVAQGTISDGRPIVGYGKATVK TPDTLDIDITYPSLGNIKAQQQITMDSPTQFKWDAHVDKDG NGYISAAELRHVMTNLGEK LTDEEVDEMIREADIDGDGQVNAEEAAQMTKILTGT LQRQE |
| EF2n3_mFAP2a | SRAAQLLPGTWQATFTNEDGQTSQGQWHFQPRSPYTMDIVAQGTISDGRPIVGYGKATVK TPDTLDIDITYPSLGNIKAQQQITMDSPTQFKWDAHVDKDG NGYISAAELRHVMTNLGEK LTDEEVDEMIREADIDGDGQVNAEEAAQMTKILTGT LQRQE |
| EF4n_mFAP2b | SRAAQLLPGTWQVTMTNEDGQTSQGQWHFQPRSPYTMDIVAQGTISDGRPIVGYGKATVK TPDTLDIDITYPSLGNIKAQQQITMDSPTQFKWDAHVKGD KDGDTITTKELGTVMRSLG QNPTEAELQDMINEVDADGDGTIDFPEFLTMMARKMKD T DSEEEIREAFRVFDKDGNGYI SAAELRHVMTNLGEKLTDEEVDEMIREADIDGDGQVNYEEFVQMPHILTGT LQRQE |
| EF4n_mFAP2a | SRAAQLLPGTWQATFTNEDGQTSQGQWHFQPRSPYTMDIVAQGTISDGRPIVGYGKATVK TPDTLDIDITYPSLGNIKAQQQITMDSPTQFKWDAHVKGD KDGDTITTKELGTVMRSLG QNPTEAELQDMINEVDADGDGTIDFPEFLTMMARKMKD T DSEEEIREAFRVFDKDGNGYI SAAELRHVMTNLGEKLTDEEVDEMIREADIDGDGQVNYEEFVQMPHILTGT LQRQE |

Chapter 4. Discussion, Materials and Methods

4.1. Discussion

We have demonstrated that the functionality of mFAPs can be readily extended by structure-based design and engineering. It should be emphasized, however, that the engineering of useful fluorescence biosensors based on mFAPs is still in its early days – the mFAPs were first described less than a year ago¹⁰. Conventional fluorescent protein-based sensors still have numerous advantages over the mFAPs in brightness (e.g. EGFP is ~3.5-fold brighter than the mFAP2a–DFHBI-1T complex), fluorescence spectral diversity⁴⁴, Ca²⁺ affinity²³ and fluorescence dynamic range⁴¹. These sophisticated reporters and sensors reflect decades of work by many groups; we hope this report will stimulate exploration of the mFAP platform. With further optimization using deep mutational scanning and structure-based design methodologies, there is likely considerable room for improvement of brightness, photostability, pH-responsiveness, Ca²⁺-responsiveness, and engineering for detection of different analytes.

At this stage, the primary advantages of the new platform are smaller size, photostability, chromophore-specificity, spatiotemporal control over fluorescence via on-demand labeling protocols, ability to fluoresce without O₂ needed for chromophore maturation (mFAP function and maturation should be unchanged in anaerobic environments), and nearly instantaneous fluorescence activation upon folding and chromophore binding. The mFAP system can be adapted to bind DFHBI-derived chromophores with different fluorescence colors, as shown by the low-level binding of the chromophore DFHO²¹ to mFAP3 (Table 2). mFAPs can be used as modular fluorescent sensors for detection and quantification of other small molecules, ions,

peptides, or nucleic acids by insertion of their respective binding peptides into the loops of mFAPs without circularly permuting the mFAPs²³, or by splitting mFAPs into two fragments to follow protein-protein association. We encourage protein engineers to explore these and other applications of the mFAP platform. The following sections of Chapter 4 comprise the materials and methods for data presented in Chapters 2 and 3.

4.2. Methods

Design of brighter and pH-responsive mFAPs

A previously described¹⁰ mFAP2 computational design model was used as a template for manual selection and design of mutable residues using Rosetta^{27,45} macromolecular modeling software. Guided by the previously generated deep mutational scanning maps¹⁰ of stability and fluorescence of b11L5F, we constructed three mFAP2 mutational variants mFAP2(P50T,S52V), mFAP2(S52T), and mFAP2(P50T,S52V,G100D) that were expected to improve the stability of the protein while also aiding crystallization. Circular dichroism in the absence of DFHBI revealed that mFAP2(P50T,S52V), hereafter called mFAP2.1, demonstrated improved stability at pH 2.93 (Figure 2b,c) and brighter fluorescence from the protonated state of DFHBI at pH 3.66 (Figure 2d,e) compared to mFAP2, consistent with improved binding of the protonated tautomers of DFHBI to the stabilized protein. A minimal site-directed mutagenesis (SDM) library was generated at 15 residue positions on mFAP2.1 encoding mutations hypothesized to improve the fluorescence ratio fold-change from low to high pH, increase DFHBI affinity, and reduce conformational flexibility of the loop connecting the seventh and eighth β -strands (known as loop7) juxtaposing the DFHBI binding pocket.

Fluorescence screening of the SDM library at pH 3.66 and pH 7.36 revealed that the most pH-responsive mutant mFAP2.1(T50P), also known as mFAP2.2, demonstrated ~1.3-fold higher fluorescence ratio fold-change from pH 3.66-7.36 than mFAP2.1 (Figure 2f). Subsequently, two independent combinatorial libraries were generated from mFAP2.2: one at 5 positions aimed at increasing loop7 rigidity, and another at 8 positions aimed at optimizing hydrophobic packing of residues in the hydrophobic β -barrel core. The brightest variant from the first library mFAP2.2(A100E,G101N,N102D,T104H), hereafter known as mFAP2.3, and the brightest variant of the second library mFAP2.2(M27W,V39I,V57A,F93W), hereafter known as mFAP2.4, showed an increase in fluorescence intensity from the phenolate state of DFHBI of ~1.1-fold and ~3.4-fold from mFAP2.2 at pH 7.36, respectively (Figure 2g,h). The mutations producing mFAP2.3 and mFAP2.4 were combined into one scaffold generating mFAP2.5. A last mutation (V67I) was identified by screening a combinatorial library of mutations at 7 positions aimed at packing more methyl groups into the hydrophobic β -barrel core of mFAP2.5. The new protein (Figure 1a), referred to as mFAP2b (“b” for bright), is ~1.2-fold brighter than mFAP2.5 and ~1.3-fold brighter than mFAP2.4 at neutral pH (Figure 2i). It was demonstrated that mFAP2b had ~10.2-fold weaker affinity for DFHBI than the initial mFAP2 design.

Another combinatorial library was generated at 5 positions of mFAP2b aimed at increasing affinity for the deprotonated state of DFHBI without compromising fluorescence intensity by packing both aromatic and aliphatic residues in the hydrophobic β -barrel core of mFAP2b. Screening for fluorescence intensity of the phenolate state of DFHBI using a relatively low DFHBI concentration (554.88 nM) resulted in mFAP2b(V13A,M15F), known as mFAP2a (“a” for affinity). mFAP2a displayed ~1.3-fold brighter fluorescence than mFAP2b at low

DFHBI concentration (Figure 2j). Aiming to further improve packing of methyl groups in the hydrophobic β -barrel core to increase the fluorescence intensity of the phenolate state of DFHBI at neutral pH while accommodating the interesting geometry of the Y71W mutation, a final combinatorial library was constructed at 3 positions of mFAP2a, resulting in designs mFAP3 through mFAP8. However, these mutants were dimmer and demonstrated lower expression levels than mFAP2b or mFAP2a, although mFAP3 showed to be the brightest DFHO binding variant (mFAP3 with 10 μ M DFHO is \sim 10-fold dimmer than mFAP2b with 10 μ M DFHBI, Table 2).

For several of the variants demonstrating the highest fluorescence intensity of the deprotonated state of DFHBI from the mFAP2.2 loop7 combinatorial library and mFAP2.2 hydrophobic β -barrel core combinatorial library (Figure 2g,h), the fluorescence ratio fold-change from pH 3.66-7.36 was measured (data not shown) as well as fluorescence of the protonated state of DFHBI at pH 3.66 (data not shown). 14 new designs (which included mFAP_pH) were constructed by manually combining the loop7 and hydrophobic β -barrel core mutations that demonstrated the highest fluorescence ratio fold-change from pH 3.66-7.36 and highest fluorescence intensity of the protonated state of DFHBI.

Design of chromophore-selective mFAPs

Computational modeling of DFHBI (Figure 1b) into the binding pocket of mFAP2b (Figure 1f) and mFAP2a (Figure 1h) using Rosetta^{27,45} macromolecular modeling software showed that the mutations V13A and M15F resulted in a void in the binding pocket of mFAP2a. It was hypothesized that a commercially-available structural variant of the DFHBI chromophore

with a trifluoromethyl group, DFHBI-1T²⁰ (Figure 1c) , could pack into the void without causing steric clashes. Computational modeling of DFHBI-1T in the pocket of mFAP2a (Figure 1i) demonstrated good protein–chromophore shape complementarity, whereas DFHBI-1T modeled into the mFAP2b pocket (Figure 1g) resulted in steric clashes. Studying the fluorescence of mFAP2a and mFAP2b in the presence of DFHBI-1T experimentally validated this (Figure 1d,e). Relative fluorescence intensities and binding affinities of DFHBI, DFHBI-1T and DFHO for selected mFAP variants were then measured at neutral pH (Table 2).

Design of extended loop library

β -hairpin loop fragments from the Protein Data Bank (www.rcsb.org) were used to manually curate custom β -barrel loop fragment databases. RosettaRemodel⁴⁶ was used to fix the β -hairpin loop termini to loops 1, 3, 5, and 7 of the *de novo* β -barrel scaffolds b11 and b32¹⁰, picking 3-mer and 9-mer fragments from the custom β -barrel loop fragment databases, from which 2,226 designs with successfully closed loops were generated. Loop coordinates were extracted as .pdb files and used as templates to generate Rosetta blueprint files specifying amino acid type, secondary structure, and ABEGO⁴⁷ type of loops to be rebuilt onto loops 1, 3, 5, and 7 of a computational model of mFAP2b, resulting in 8,904 Rosetta blueprint files. For each blueprint file, a RosettaScripts^{26,27} XML script (see Section 4.3) was used to graft the loop onto mFAP2b with a centroid energy function followed by Monte Carlo⁴⁸ sampling of protein side-chain repacking and protein side-chain and backbone minimization steps in a full-atom Cartesian coordinate energy function⁷. 7,748 resulting designs were filtered for the following computational protein design metrics (as scored from the XML script in Section 4.3): geometry =

1; total_score_res \leq -3.72714; holes \leq -1.2729; pstat \geq 0.755044; buns_sc_heavy \leq 2; buns_bb_heavy \leq 2; interfE \leq -38.375; SC \geq 0.734076; p_aa_pp \leq -40.8947; and omega \leq 2.8757. Only 59 designs with extended loops built onto loops 1, 3 and 7 of mFAP2b passed the filter criteria for experimental testing.

Design of Ca²⁺-responsive mFAPs

The mFAP2b loop7 sequence and the five extended loop7 sequences shown to confer fluorescence (Figure 9) were sampled as linkers for grafting the sequence of one EF-hand motif from PDB ID 1NKF³² onto loop7 of mFAP2b. An in-house script (see Section 4.3) was written to prune the experimentally-validated extended loop7 sequences one residue at a time keeping up to 4 residues on the N-terminal and C-terminal linkers relative to the grafted EF-hand motif, optionally adding an additional glycine residue on the N-terminal linker and optionally adding an additional glycine or proline residue on the C-terminal linker. This combinatorial library had a theoretical diversity of 1,140 linker designs. The linkers resulting in positively and negatively allosteric Ca²⁺-responsive mFAPs containing one EF-hand motif were combinatorially sampled to act as linkers for grafting two EF-hand motifs from PDB ID 1FW4³³ onto loop7 of mFAP2b, where the N-terminal helix of PDB ID 1FW4 was truncated up to homologous residues on successfully grafted single EF-hand motif designs. This combinatorial library had a theoretical diversity of 385. Interestingly, screening a combinatorial linker library that preserved the N-terminal helix of PDB ID 1FW4 resulted in unstable proteins that did not fluoresce and dimly fluorescent proteins that did not thermodynamically couple Ca²⁺ and DFHBI binding (data not shown). The linkers resulting in negatively allosteric Ca²⁺-responsive mFAPs containing two

EF-hand motifs were combinatorially sampled to act as linkers for grafting four EF-hand motifs from PDB ID 1PRW³⁴ onto loop7 of mFAP2b, where the N-terminal helix of PDB ID 1PRW was truncated up to homologous residues on successfully grafted single EF-hand motif designs. This combinatorial library had a theoretical diversity of 25. The Ca²⁺-responsive mFAP naming convention used was: “EF” (for “EF-hand motif”) + the number of EF-hand motifs grafted (e.g. 1, 2, or 4) + “p” or “n” (for “positively allosteric” or “negatively allosteric”, respectively) + an optional design identification number + “_mFAP2a” or “_mFAP2b” (for the mFAP2a or mFAP2b primary amino acid sequence, respectively, excluding loop7).

Synthetic DNA construction

For combinatorial libraries, oligonucleotides with degenerate codons encoding desired mFAP sequences were designed using SwiftLib⁴⁹. Overlapping forward and reverse oligonucleotides with degenerate and/or non-degenerate codons spanning the mFAP gene of interest were synthesized (IDT DNA). Oligonucleotides spanning identical gene regions were pooled at equimolar ratios relative to the theoretical amino acid diversity encoded by each gene region. Full-length genes were constructed using assembly polymerase chain reaction (PCR) with Phusion polymerase (NEB). For the extended loop library, the loop1, loop3, and loop7 libraries were assembled separately, and the concentrations of assembly PCR products consisting of full-length genes were quantified and the three libraries pooled in quantities proportional to the theoretical library diversities of assembly PCR products. Successfully assembled full-length genes, as well as synthetic gBlock (IDT DNA) oligonucleotides encoding full-length protein sequences, with 5' and 3' flanking vector backbone sequences were sub-cloned into the pET15b

vector (Novagen) or the pcDNA5/FRT/TO vector (ThermoFisher Scientific) using Gibson assembly. The mFAP2.2 loop7 combinatorial library was constructed via Gibson assembly of polyacrylamide gel electrophoresis (PAGE)-purified duplex oligonucleotides into pET15b-mFAP2.2 linear vector DNA. The full-length gene encoding pHRed¹² was synthesized and cloned into the pET29b(+) vector (IDT DNA). Cloned DNA constructs were transformed into Lemo21(DE3) competent *E. coli* (NEB) and plated onto LB-agar plates substituted with 50 µg/mL carbenicillin or 50-100 µg/mL kanamycin.

Large-scale protein purification

For expression of 6xHis-tagged proteins in Lemo21(DE3) *E. coli* (NEB), either a single colony, 25 µL of overnight-grown culture, or 25 µL of a 20% glycerol culture stock was inoculated into 50, 500, or 1000 mL of LB media or Studier auto-induction⁵⁰ media (with or without 0.5 mM L-rhamnose) substituted with 50 µg/mL carbenicillin or 50 µg/mL kanamycin. To induce protein expression, cells were grown at 37°C shaking at 200-250 rotations per minute (rpm) overnight with 0.5 mM isopropyl β-D-thiogalactopyranoside (IPTG) final concentration added either prior to inoculation or 4 hours prior to harvesting cells. Cells were harvested by centrifugation at 4,000 rpm for 10 minutes at 4°C. Cell pellets were resuspended in 20-30 mL of either lysis buffer #1 (25 mM Tris, 300 mM NaCl, 20 mM imidazole, pH 8.0) substituted with 1 mg/mL phenylmethylsulfonyl fluoride (PMSF) (Sigma Aldrich) and a small amount of deoxyribonuclease I (DNase I) from bovine pancreas (Sigma Aldrich), lysis buffer #2 (20 mM Tris, 300 mM NaCl, 30 mM imidazole, pH 7.4), or lysis buffer #3 (20 mM Na₂HPO₄, 500 mM NaCl, 30 mM imidazole, 0.25% CHAPS, 1 mM PMSF, 1 mg/mL DNase, pH 8.0), then lysed via

either sonication (Fisher Scientific) at 40% amplitude, FastPrep (MPBio) at 1,600 rpm, or cell disruption using a M110P microfluidizer (Microfluidics) at 18,000 psi.

Crude lysates were centrifuged at 24,000xg for 30-45 minutes at 4°C. Clarified lysates were purified via gravity Ni-NTA immobilized metal affinity chromatography (IMAC). 2 mL of Ni-NTA resin (QIAGEN) was equilibrated with 10 mL of either lysis buffer #1, wash buffer #2 (20 mM Tris, 500 mM NaCl, 30 mM imidazole, 5% glycerol, pH 7.4), or wash buffer #3 (20 mM Na₂HPO₄, 500 mM NaCl, 30 mM imidazole, 5% glycerol, pH 8.0). Clarified lysate was loaded onto the column and the flow through was collected. The column was washed 1-3 times with 20 mL of either wash buffer #1 (25 mM Tris, 300 mM NaCl, 30 mM imidazole, pH 8.0), wash buffer #2, or wash buffer #3, and then eluted in 5-15 mL of either elution buffer #1 (20 mM Tris, 300 mM NaCl, 500 mM imidazole, 5% glycerol, pH 7.4), elution buffer #2 (25 mM Tris, 300 mM NaCl, 250 mM imidazole, pH 8.0), or elution buffer #3 (20 mM Na₂HPO₄, 300 mM NaCl, 500 mM imidazole, 5% glycerol, pH 8.0). For keeping 6xHis tags intact, purified protein eluates from IMAC were buffer exchanged into high salt Tev cleavage buffer (25 mM Tris, 100 mM NaCl, pH 8.0) or low salt Tev cleavage buffer (20 mM Tris, 50 mM NaCl, pH 7.4) using Amicon Ultra-15 Centrifugal Filter Units (Millipore Sigma). For removing 6xHis tags, a 1:100 dilution of TEV-6xHis protease was added and the reaction was incubated at 25°C overnight. TEV-6xHis protease was removed via secondary Ni-NTA IMAC purification eluting in 5 mL of lysis buffer #1 or lysis buffer #2. Cleaved protein was concentrated in Amicon Ultra-15 Centrifugal Filter Units. Protein concentrations were measured using a QuBit 2.0 and QuBit Protein Assay Kit (ThermoFisher Scientific) or a NanoDrop 2000 (Thermo Scientific) with extinction coefficients predicted from primary amino acid sequence using the ProtParam tool

(<https://web.expasy.org/protparam>) or biopython ProtParam module (<https://github.com/biopython/biopython/blob/master/Bio/SeqUtils/ProtParam.py>).

Size-exclusion chromatography (SEC)

Protein samples were prepared at ≥ 1 mg/mL and applied to a Superdex 75 10/300 GL column (GE Healthcare) or Superdex 200 10/300 GL column on a LC 1200 Series high-performance liquid chromatography (HPLC) machine (Agilent Technologies) for separation of IMAC-purified proteins based on molecular size. SEC-purified proteins were eluted in either high salt Tev cleavage buffer, Tris buffered saline (20 mM Tris, 300 mM NaCl, pH 7.4), phosphate buffered saline (PBS) (25 mM phosphate, 150 mM NaCl, pH 7.4) or Dulbecco's Phosphate-Buffered Saline without calcium or magnesium (DPBS) (Thermo Scientific). Monomeric protein fractions were concentrated using Amicon Ultra-15 Centrifugal Filter Units. Protein concentrations were measured as discussed above.

Small-scale protein purification

25 μ L of overnight-grown cultures of Lemo21(DE3) *E. coli* (NEB) were inoculated into each well of Nunc 2.0 mL DeepWell 96-well plates (Thermo Scientific) containing 1 mL of LB media substituted with 50 μ g/mL carbenicillin with 2-8 replicate plates to optimize purified protein yields. Cells were grown at 37°C and shaken at 1,200 rpm for 3-4 hours, then 0.5 mM IPTG final concentration was added, and protein expression induced for 4 hours at 37°C shaken at 1,200 rpm. Cells were pelleted at 2,272xg for 2-5 minutes, pellets resuspended in 50 μ L of

lysis buffer #1 substituted with 1 mg/mL PMSF and a small amount of DNase I, combining pellets of any replicate plates. Cells were transferred to PCR plates for cell lysis in a plate sonicator (Qsonica) at 60% amplitude for 2-4 minutes total. Clarified lysates were applied to His MultiTrap HP (GE Healthcare) 96-well plates pre-equilibrated in lysis buffer #1, and IMAC purification undergone following the manufacturer's protocol for purification except resin was washed three times in wash buffer #1 and eluted three times, each time using 50 μ L of elution buffer #1 and consolidating eluents.

Screening libraries

The number of *E. coli* colonies picked for functional screening was approximately 4-fold the theoretical diversity of each library. *E. coli* colonies were inoculated into 1 mL of LB media substituted with 50 μ g/mL carbenicillin in Nunc 2.0 mL DeepWell 96-well plates, and were grown at 37°C shaking at \sim 1,200 rpm overnight. 25 μ L of these cultures were inoculated into 1 mL of fresh LB media substituted with 50 μ g/mL carbenicillin, grown at 37°C and \sim 1,200 rpm for 3-4 hours, then 0.5 mM IPTG final concentration was added to each well, and protein expression induced for 4 hours at 37°C shaking at \sim 1,200 rpm. Cells were pelleted at 2,272xg for 2-5 minutes and pellets were resuspended in 50 μ L of lysis buffer #1 substituted with 1 mg/mL PMSF, a small amount of DNase I, and 2 mg/mL lysozyme from chicken egg white (Sigma) for lysis. Crude lysates were vigorously shaken at 25-37°C for 12-48 hours, then clarified by centrifugation. Clarified lysates were assayed on a Synergy Neo2 hybrid multi-mode reader (BioTek) in 96-well non-binding surface microplates (Corning 3650).

For each clone encoding a β -barrel core variant, loop7 variant, or extended loop variant, 15 μ L of clarified lysate was combined with 185 μ L of Na_2HPO_4 -citrate (pH 7.36 or 3.66) buffer substituted with 150 mM NaCl and 1.075 μ M DFHBI (Lucerna). Na_2HPO_4 -citrate buffer was made from 0.2 M Na_2HPO_4 and 0.1 M citrate stock solutions, and final pH was adjusted using hydrochloric acid (HCl) or sodium hydroxide (NaOH). DFHBI stock solution was 2 mM DFHBI in 23.75 mM Tris (pH 8.0), 95 mM NaCl, and 5% dimethyl sulfoxide (DMSO). Clones that demonstrated fluorescence were Sanger sequenced via colony PCR of overnight cultures, and the brightest designs or designs with highest fluorescence fold-change across pH 7.36-3.66 were further characterized with large-scale protein purification.

For each clone encoding one or more EF-hand motifs grafted onto β -barrel loop7, 15 μ L of lysate was combined with 185 μ L of either 2 mM CaCl_2 , 25 mM Tris (pH 8.0), 100 mM NaCl, 1.075 μ M DFHBI or 2 mM EGTA, 25 mM Tris (pH 8.0), 100 mM NaCl, 1.075 μ M DFHBI. Clones that demonstrated greater than an approximately two-fold change in fluorescence intensity between CaCl_2 and EGTA conditions were Sanger sequenced, and the highest fold-change designs were further characterized with large-scale protein purification.

Fluorescence intensity assays

To measure fluorescence intensities of the phenolate state of chromophores, fluorescence endpoints were measured on a Synergy Neo2 hybrid multi-mode reader (BioTek) in flat bottom, black polystyrene, non-binding surface 96-well microplates (Corning 3650). Fluorescence intensity was measured in triplicate by exciting at $\lambda_{\text{ex}} = 484$ nm and measuring fluorescence emission at $\lambda_{\text{em}} = 505$ nm (or $\lambda_{\text{em}} = 511$ nm for clones harboring the W27 mutation) (Figure 2g,h).

The W27 mutation redshifts the peak emission wavelength from $\lambda_{em} = \sim 505$ nm to $\lambda_{em} = \sim 511$ nm, presumably due to the W27 indole ring donating a hydrogen bond to the imidazolinone moiety of the deprotonated state of DFHBI which stabilizes the chromophore conjugated π -electron system in the excited state causing the redshift in emission¹⁴. 15 μ L of small-scale purified protein was combined with 185 μ L of Na_2HPO_4 -citrate (pH 7.36) substituted with 150 mM NaCl and 108.11 nM DFHBI (from a 2 mM DFHBI stock solution) for a final concentration of 100 nM DFHBI. In measuring the excitation spectra from $\lambda_{em} = 525$ nm of each clone in triplicate (Figure 2i), 30 μ L of large-scale purified protein was combined with 170 μ L of 25 mM Tris (pH 8.0) substituted with 100 mM NaCl and 914.12 nM DFHBI (from a 0.2 mM DFHBI stock solution in 0.5% DMSO and 99.5% high salt Tev cleavage buffer) for a final concentration of 7.77 μ M protein and 777 nM DFHBI. In measuring the fluorescence intensity at $\lambda_{ex} = 484$ nm and $\lambda_{em} = 509$ nm of each clone in triplicate (Figure 2j), 30 μ L of large-scale purified protein was combined with 170 μ L of 25 mM Tris (pH 8.0) substituted with 100 mM NaCl and 652.8 nM DFHBI (from a 2 mM DFHBI stock solution) for a final concentration of 5.5488 μ M protein and 554.88 nM DFHBI. In collecting emission spectra by exciting fluorescence at $\lambda_{ex} = 484$ nm (Figure 9b) and measuring fluorescence endpoints in triplicate at unique peak excitation and emission wavelengths (Figure 9c), 195 μ L of large-scale purified protein was combined with 5 μ L of 25 mM Tris (pH 8.0) substituted with 100 mM NaCl and 40 μ M DFHBI (from a 2 mM DFHBI stock solution) for a final concentration of 10 μ M protein and 1 μ M DFHBI.

In measuring fluorescence intensity of small-scale purified proteins (Table 2), wells were excited at $\lambda_{ex} = 488$ nm for DFHBI and DFHBI-1T and $\lambda_{ex} = 505$ nm for DFHO, and fluorescence emission measured at $\lambda_{em} = 510$ nm for DFHBI and DFHBI-1T and $\lambda_{em} = 545$ nm for DFHO.

Fluorescence endpoints were measured using either 25 μL or 50 μL of small-scale purified protein in either 175 μL or 150 μL , respectively, of Na_2HPO_4 -citrate (pH 7.36) buffer supplemented with 150 mM NaCl and either 100 nM or 10 μM of either DFHBI (Lucerna), DFHBI-1T (Lucerna) or DFHO (Lucerna) (from 20 mM chromophore stock solutions in 100% DMSO), for 200 μL final volumes.

Densitometry

In quantifying relative protein expression levels in *E. coli* (Table 2), 5 μL of small-scale purified proteins were combined with 5 μL of 2x Laemmli buffer, denatured at 99°C for 10 minutes, and 5 μL of each sample run on Any kD Mini-PROTEAN TGX Stain-Free Precast Gels (Bio-Rad) in Tris-glycine buffer alongside 5 μL of Precision Plus Protein Unstained Protein Standard (Bio-Rad). Gels were stained using an eStain L1 Protein Staining System (GenScript) and imaged using a Molecular Imager ChemiDoc XRS+ (Bio-Rad). Relative densitometry was analyzed in Image Lab Software Version 6.0.1 build 34 Standard Edition (Bio-Rad) referenced to the 15 kDa protein ladder band.

pH-dependent fluorescence assays

pH-dependent fluorescence was measured on a Synergy Neo2 hybrid multi-mode reader in flat bottom, black polystyrene, non-binding surface 96-well microplates (Corning 3650). In measuring the pH-sensitivity of β -barrel variants in triplicate (Figure 7b), 20 μL of large-scale purified protein was combined with 180 μL of Na_2HPO_4 -citrate (pH 7.34 or 3.61) substituted

with 150 mM NaCl and 277.78 nM DFHBI (from a 2 mM DFHBI stock solution) for final concentrations of 2.5 μ M protein and 250 nM DFHBI. Blank buffer wells for background subtraction were prepared identically except using 20 μ L of high salt Tev cleavage buffer instead of purified protein. Wells were excited at $\lambda_{ex} = 387$ nm or $\lambda_{ex} = 484$ nm and fluorescence emission measured at $\lambda_{em} = 501$ nm or $\lambda_{em} = 505$ nm, respectively. Following buffer background subtraction, the fluorescence ratio fold-change from pH 3.61-7.34 was calculated as:

$$\text{Fluorescence Ratio Fold-Change (pH 3.61 - 7.34)} = \frac{\left(\frac{F^{\lambda_{ex} = 387 \text{ nm}, \lambda_{em} = 501 \text{ nm}}}{F^{\lambda_{ex} = 484 \text{ nm}, \lambda_{em} = 505 \text{ nm}}} \right)_{\text{pH 3.61}}}{\left(\frac{F^{\lambda_{ex} = 387 \text{ nm}, \lambda_{em} = 501 \text{ nm}}}{F^{\lambda_{ex} = 484 \text{ nm}, \lambda_{em} = 505 \text{ nm}}} \right)_{\text{pH 7.34}}}$$

where $F^{\lambda_{ex}, \lambda_{em}}_{pH}$ is the mean of three technical replicates of endpoint fluorescence measurements at the subscripted pH value and superscripted excitation (λ_{ex}) and emission (λ_{em}) wavelengths.

In measuring pH-dependent excitation spectra (Figure 8f,g), excitation spectra were measured at pH 3.61 using excitation wavelengths in the range $\lambda_{ex} = 300$ -480 nm and emission wavelength $\lambda_{em} = 501$ nm, and measured at pH 7.34 using excitation wavelengths in the range $\lambda_{ex} = 300$ -484 nm and emission wavelength $\lambda_{em} = 505$ nm.

In measuring pH-sensitivity of β -barrel variants (Figure 2f) in triplicate, 140 μ L of Na₂HPO₄-citrate (pH 7.36 or 3.66) substituted with 150 mM NaCl and 1.429 μ M DFHBI (from a 2 mM DFHBI stock solution) was combined with 10 μ L of small-scale purified protein for a final concentration of 1.333 μ M DFHBI. Fluorescence endpoints were measured by exciting at $\lambda_{ex} = 387$ nm or $\lambda_{ex} = 483$ nm and measuring fluorescence emission at $\lambda_{em} = 501$ nm or $\lambda_{em} = 504$ nm, respectively. Without background subtraction, the fluorescence ratio fold-change from pH 3.66-7.36 was calculated as:

$$\text{Fluorescence Ratio Fold-Change (pH 3.66 - 7.36)} = \frac{\left(\frac{F_{\text{pH } 3.66}^{\lambda_{\text{ex}} = 387 \text{ nm}, \lambda_{\text{em}} = 501 \text{ nm}}}{F_{\text{pH } 3.66}^{\lambda_{\text{ex}} = 483 \text{ nm}, \lambda_{\text{em}} = 504 \text{ nm}}} \right)}{\left(\frac{F_{\text{pH } 7.36}^{\lambda_{\text{ex}} = 387 \text{ nm}, \lambda_{\text{em}} = 501 \text{ nm}}}{F_{\text{pH } 7.36}^{\lambda_{\text{ex}} = 483 \text{ nm}, \lambda_{\text{em}} = 504 \text{ nm}}} \right)}$$

where $F_{\text{pH}}^{\lambda_{\text{ex}}, \lambda_{\text{em}}}$ is the mean of three technical replicates of endpoint fluorescence measurements at the subscripted pH and superscripted excitation (λ_{ex}) and emission (λ_{em}) wavelengths.

In measuring pH-dependent fluorescence (Figure 8d,e,h,i), Na₂HPO₄-citrate buffer substituted with 150 mM NaCl at 32 unique pH values were produced via mixing various volumes of 100 mM citric acid (Sigma Aldrich), 200 mM Na₂HPO₄ (Sigma Aldrich), and 2 M NaCl, and final pHs quantified via an Accumet AB15 Basic pH meter (Fisher Scientific). pHRed was produced via large-scale protein purification, 6xHis-tag removal and SEC-purification, and mFAP_pH was produced via large-scale protein purification and SEC-purification. pH-dependent fluorescence was measured at 500 nM final protein concentration at each pH in triplicate in 200 μ L final volumes per well. To prevent pH fluctuations upon addition of protein and DFHBI, 195 μ L of Na₂HPO₄-citrate buffers substituted with 150 mM NaCl at each pH was aliquoted per well, 4 μ L of 25 μ M protein was aliquoted per well, and 1 μ L of 1 mM DFHBI (in 2.5% DMSO and 97.5% high salt Tev cleavage buffer) was added to wells containing mFAP_pH, whereas 1 μ L of chromophore buffer (2.5% DMSO and 97.5% high salt Tev cleavage buffer) was added to wells containing pHRed. Blank plates for background subtraction for mFAP_pH and pHRed were prepared identically, respectively, except adding 4 μ L of high salt Tev cleavage buffer instead of purified protein. In measuring excitation spectra at each pH (Figure 8d), excitation wavelengths were set to the range $\lambda_{\text{ex}} = 250\text{-}540$ nm and fluorescence emission measured at $\lambda_{\text{em}} = 562$ nm.

In measuring emission spectra at two pH values (Figure 8e), emission spectra for the blueshifted excitation peak was measured at pH 3.63 using excitation wavelength $\lambda_{ex} = 379$ nm and emission wavelengths in the range $\lambda_{em} = 460-800$ nm, and emission spectra for the redshifted excitation peak was measured at pH 8.38 using excitation wavelength $\lambda_{ex} = 430$ nm and emission wavelengths in the range $\lambda_{em} = 460-800$ nm. In measuring fluorescence from both the blueshifted and redshifted excitation peaks (Figure 8h,i), for mFAP_pH the fluorescence excitation wavelengths were $\lambda_{ex} = 379$ nm and $\lambda_{ex} = 483$ nm and fluorescence emission wavelengths were $\lambda_{em} = 498$ nm and $\lambda_{em} = 503$ nm, respectively, whereas for pHRed the fluorescence excitation wavelengths were $\lambda_{ex} = 440$ nm and $\lambda_{ex} = 575$ nm and fluorescence emission wavelengths were both $\lambda_{em} = 635$ nm. In Figure 8i, for the mFAP_pH–DFHBI complex and pHRed the ratiometric fluorescence (F_{ratio}) is calculated from the background-subtracted, unnormalized fluorescence measurements from Figure 8h using fluorescence emission from the redshifted excitation peak ($F^{redshifted \lambda_{ex}}$) as the numerator and fluorescence emission from the blueshifted excitation peak ($F^{blueshifted \lambda_{ex}}$) as the denominator:

$$F_{ratio} = \frac{F^{redshifted \lambda_{ex}}}{F^{blueshifted \lambda_{ex}}}$$

In Figure 8i, mean ratiometric fluorescence values are fit to continuous logistic equations with the formula $F_{ratio} = \frac{23.48}{1 + e^{-2.02 \cdot (pH - 6.90)}}$ for the mFAP_pH–DFHBI complex and $F_{ratio} = \frac{4.20}{1 + e^{2.00 \cdot (pH - 6.60)}}$ for pHRed using non-linear least squares fitting, which serve as a continuous calibration curve for real-time quantification of pH. *In situ* calibration curves unique to the system of interest can be determined as previously described¹¹.

DFHBI, DFHBI-1T, and DFHO titrations

Fluorescence endpoints were measured on a Synergy Neo2 hybrid multi-mode reader (BioTek) in flat bottom, black polystyrene, non-binding surface 96-well microplates (Corning 3650). In measuring chromophore binding affinities (Figure 1d,e), mFAP2, mFAP2a, and mFAP2b were produced by large-scale protein purification and SEC purification. Proteins were aliquoted in eight technical replicates in 200 μ L final volumes to 20 nM final concentration in ten serial dilutions ($\sqrt{10}$ dilution factor) of DFHBI starting from 31.62 μ M DFHBI or 31.62 μ M DFHBI-1T final concentrations, including an eleventh condition without chromophore. Fluorescence was excited at $\lambda_{\text{ex}} = 468$ nm and fluorescence emission measured at $\lambda_{\text{em}} = 530$ nm. Background fluorescence endpoints of wells with identical chromophore concentrations but purified protein replaced with an identical volume of high salt Tev cleavage buffer were measured, and fluorescence endpoints subtracted from those measured with protein. Background-subtracted data were averaged and the means normalized from 0 to 1 and fit to a single binding site isotherm equation using non-linear least squares fitting to obtain a fitted K_d value (Table 1), and the fit re-scaled to the maximum mean value (Figure 1d,e).

Chromophore affinities (Table 2) were obtained by producing proteins via large-scale protein purification keeping 6xHis-tags intact (with some variants further purified by SEC) and preparing proteins at 25 μ L final volumes in flat bottom, black polystyrene, non-binding surface 96-well half-area microplates (Corning 3686). Proteins were aliquoted to 500 nM final concentrations in high salt Tev cleavage buffer (mFAP2.2.5 was prepared at 385.8 nM, and mFAP2a and mFAP3 were prepared at 50 nM) in eleven serial dilutions ($\sqrt{10}$ dilution factor) from 1 mM DFHBI, 1 mM DFHBI-1T, or 1 mM DFHO, including a twelfth condition without

chromophore. Fluorescence endpoints were measured on a Synergy Neo2 hybrid multi-mode reader (BioTek) with excitation and emission wavelengths set differently between protein variants to achieve optimal fluorescence output. Background fluorescence endpoints of wells with identical chromophore concentrations but purified protein replaced with an identical volume of high salt Tev cleavage buffer were measured, and fluorescence endpoints measured with identical instrument settings subtracted from those measured with protein prior to normalization.

Ca²⁺-responsive mFAP DFHBI titrations

In measuring Ca²⁺-dependent DFHBI affinity of Ca²⁺-responsive mFAPs on a Synergy Neo2 hybrid multi-mode reader (Figure 11a,b,c, Figure 13a,b,d,e,g,h, Figure 14a,b,d,e,g,h, and Figure 15a,b,d,e,g,h), purified proteins were produced via large-scale protein purification and aliquoted to a final concentration of 500 nM in either 450 mM CaCl₂ (Sigma Aldrich) (prepared in high salt Tev cleavage buffer) or high salt Tev cleavage buffer, along with ten serial dilutions ($\sqrt{10}$ dilution factor) of DFHBI starting from 316.22 μ M DFHBI (from a 2 mM DFHBI stock solution) including an eleventh condition without chromophore. Final volumes were 25 μ L in flat bottom, black polystyrene, non-binding surface 96-well half-area microplates (Corning 3686) or 200 μ L in flat bottom, black polystyrene, non-binding surface 96-well microplates (Corning 3650). Fluorescence endpoints were measured using excitation wavelength $\lambda_{\text{ex}} = 488$ nm and emission wavelength $\lambda_{\text{em}} = 510$ nm. Background fluorescence endpoints of wells with identical chromophore concentrations lacking protein (substituted for equivalent volumes of high salt Tev cleavage buffer) were measured and subtracted from protein measurements prior to normalization.

For DFHBI titrations of EF4n_mFAP2a and EF4n_mFAP2b (Figure 16a,b), a small amount of Chelex 100 sodium form (Sigma Aldrich) was added to purified protein (produced by large-scale protein purification and SEC-purification) and nutated at 4°C overnight. High salt Tev cleavage buffer with a small amount of Chelex 100 was prepared and mixed at room temperature overnight, and a 2 mM DFHBI stock solution (dissolved in 5% DMSO and 95% high salt Tev cleavage buffer) with a small amount of Chelex 100 was prepared and nutated overnight at 4°C. Proteins were aliquoted to a final concentration of 5 μM in either 500 μM CaCl₂ (Sigma Aldrich) (prepared in high salt Tev cleavage buffer) or 500 μM EGTA (Sigma Aldrich) (prepared in high salt Tev cleavage buffer), along with ten serial dilutions ($\sqrt{10}$ dilution factor) of DFHBI starting from 316.22 μM DFHBI (using the DFHBI stock solution and high salt Tev cleavage buffer pre-treated with Chelex 100), including an eleventh condition without chromophore. Final volumes were 25 μL in flat bottom, black polystyrene, non-binding surface 96-well half-area microplates (Corning 3686). Fluorescence endpoints were measured using excitation wavelength $\lambda_{\text{ex}} = 488$ nm and emission wavelength $\lambda_{\text{em}} = 510$ nm for EF4n_mFAP2b and excitation wavelength $\lambda_{\text{ex}} = 478$ nm and emission wavelength $\lambda_{\text{em}} = 520$ nm for EF4n_mFAP2a. Background fluorescence endpoints of wells with identical chromophore concentrations lacking protein (substituted for equivalent volumes of Chelex 100 pre-treated high salt Tev cleavage buffer) were measured and subtracted from protein measurements prior to normalization.

Ca²⁺-responsive mFAP Ca²⁺ titrations

In measuring Ca²⁺ affinity of mFAPs on a Synergy Neo2 hybrid multi-mode reader (Figure 11d,e,f, Figure 13c,f,i, Figure 14c,f,i, and Figure 16c,f,i), purified proteins were produced via large-scale protein purification and aliquoted in triplicate to a final concentration of 500 nM with 5 μ M DFHBI (from a 2 mM DFHBI stock solution) in eleven serial dilutions ($\sqrt{10}$ dilution factor) of CaCl₂ (Sigma Aldrich) starting from either 900 mM or 90 mM CaCl₂ (diluted using high salt Tev cleavage buffer) including a twelfth condition without CaCl₂. Final volumes were 200 μ L in flat bottom, black polystyrene, non-binding surface 96-well microplates (Corning 3650). Fluorescence endpoints were measured using excitation wavelength $\lambda_{\text{ex}} = 484$ nm and emission wavelength $\lambda_{\text{em}} = 508$ nm. Triplicate background fluorescence endpoints of wells with identical chromophore and CaCl₂ concentrations lacking protein (substituted for equivalent volumes of high salt Tev cleavage buffer) were measured, averaged per condition, and subtracted from protein measurement averages of the same conditions.

For Ca²⁺ titrations of EF4n_mFAP2a and EF4n_mFAP2b (Figure 16c), a small amount of Chelex 100 sodium form (Sigma Aldrich) was added to purified protein (produced by large-scale protein purification and SEC-purification) and nutated at 4°C overnight. EF4n_mFAP2a was aliquoted in triplicate to a final concentration of 8 μ M with 80 μ M DFHBI (from a 2 mM DFHBI stock solution pre-treated with Chelex 100) and EF4n_mFAP2b was aliquoted in triplicate to a final concentration of 6.25 μ M with 43.35 μ M DFHBI (from a 2 mM DFHBI stock solution pre-treated with Chelex 100), in eleven serial dilutions ($\sqrt{10}$ dilution factor) of CaCl₂ starting from 9 mM or 4 mM CaCl₂ (diluted using high salt Tev cleavage buffer pre-treated with Chelex 100) including a twelfth condition without CaCl₂. Final volumes were 25 μ L in flat bottom, black

polystyrene, non-binding surface 96-well half-area microplates (Corning 3686) or 200 μ L in flat bottom, black polystyrene, non-binding surface 96-well microplates (Corning 3650). Fluorescence endpoints were measured for EF4n_mFAP2a using excitation wavelength $\lambda_{\text{ex}} = 478$ nm and emission wavelength $\lambda_{\text{em}} = 520$ nm, and EF4n_mFAP2b using excitation wavelength $\lambda_{\text{ex}} = 484$ nm and emission wavelength $\lambda_{\text{em}} = 508$ nm. Triplicate background fluorescence endpoints of wells with identical chromophore and CaCl_2 concentrations lacking protein (substituted for equivalent volumes of high salt Tev cleavage buffer) were measured, averaged per condition, and subtracted from protein measurement averages of the same conditions. For non-linear least squares fitting to obtain K_d values, means were fit to a single binding site isotherm equation for positively allosteric Ca^{2+} -responsive mFAPs or an inverse single binding site isotherm equation for negatively allosteric Ca^{2+} -responsive mFAPs, where Ca^{2+} binding sites were modeled independently with a Hill coefficient of 1.

EF2n_mFAP2b DFHBI titration versus Ca^{2+} titration heatmap

EF2n_mFAP2b was aliquoted to a final concentration of 500 nM in eleven serial dilutions ($\sqrt{10}$ dilution factor) of CaCl_2 starting from 4.5 mM CaCl_2 along columns, and eight serial dilutions ($\sqrt{10}$ dilution factor) of DFHBI starting from 500 μ M DFHBI along rows, at final volumes of 25 μ L in flat bottom, black polystyrene, non-binding surface 96-well half-area microplates (Corning 3686). Fluorescence endpoints were measured on a Synergy Neo2 hybrid multi-mode reader using excitation wavelength $\lambda_{\text{ex}} = 484$ nm and emission wavelength $\lambda_{\text{em}} = 508$ nm. Raw data (without background subtraction) was normalized from 0 to 1 and reported (Figure 17c, *top row*).

Circular dichroism (CD)

CD measurements were recorded at 25°C in a 1 mm cuvette on an AVIV model 420 CD spectrometer (Biomedical, Inc.). mFAP2 and mFAP2.1 were purified by large-scale protein purification and SEC-purification in PBS, and CD wavelength scans recorded from 195 nm to 260 nm. mFAP2 was measured at 0.4412 mg/mL and mFAP2.1 at 0.5 mg/mL in Na₂HPO₄-citrate buffer (pH adjusted to 7.75, 3.96, or 2.93 using NaOH and HCl). Reported data does not background subtract buffer blanks (Figure 2b,c).

EF4n_mFAP2b (Figure 12) was purified by large-scale protein purification and SEC purification in DPBS. A small amount of Chelex-100 was added to the protein sample and nutated overnight at 4°C. A stock solution of 1 mM CaCl₂ was prepared in DPBS pre-treated with a small amount of Chelex-100 overnight. Far-ultraviolet CD wavelength scans and thermal denaturations were performed with 0.5 mg/mL purified protein in either 100 μM CaCl₂ or DPBS, both using Chelex 100 pre-treated DPBS. Wavelength scans from 195 nm to 260 nm were recorded at 25°C, and thermal denaturation was monitored at 220 nm wavelength from 25°C to 95°C at 2°C evenly spaced intervals. Reported data are background subtracted from the corresponding 100 μM CaCl₂ or DPBS buffer measurements without protein.

Quantum yield measurements

Protein preparation. mFAP2a and mFAP2b were produced by large-scale protein purification and dialyzed into DPBS that was adjusted to pH 7.40 using NaOH.

Chromophore preparation. DFHBI (Lucerna) and DFHBI-1T (Lucerna) were dissolved to 20 mM in 100% DMSO, and diluted in DPBS (pH 7.40) to measure absorbances on a Jasco V-750 spectrophotometer at peak absorbance wavelengths (417 nm for DFHBI and 422 nm for DFHBI-1T). Following background subtraction of identical buffer without chromophore, Beer's Law was used to calculate the molar chromophore concentrations of the stock solutions using previously reported extinction coefficients²⁰.

Preparation of protein–chromophore complexes. For quantum yield measurements, 1.0 μM chromophore solutions in DPBS (pH 7.40) at 4.0 mL final volumes were prepared for the following six conditions: DFHBI only, DFHBI-1T only, 133.83 μM 6xHis-mFAP2a with DFHBI, 133.70 μM 6xHis-mFAP2a with DFHBI-1T, 205.80 μM 6xHis-mFAP2b with DFHBI, 205.60 μM 6xHis-mFAP2b with DFHBI-1T.

Extinction coefficients. Absorbance spectra of protein-chromophore complexes were first measured using a DenoVix DS-11+ Spectrophotometer (1 nm interval). The extinction coefficients were then calculated using Beer's Law:

$$A = \varepsilon \cdot b \cdot c$$

where A is peak absorbance, ε is extinction coefficient, b is path length (1 cm), and c is concentration (1.0 μM).

Relative quantum yield. A Perkin-Elmer LS-B Luminescence Spectrophotometer (10 nm bandwidth, 1 nm interval, 100 nm/min) was used. The fluorescence emission spectra of the protein–chromophore complexes (in DPBS, pH 7.40) and reference dye Acridine Yellow G (in methanol) were first obtained, and the quantum yield was then calculated using the equation⁵¹:

$$\Phi_c = \Phi_r \cdot \frac{1-10^{-A_r(\lambda_{ex})}}{1-10^{-A_c(\lambda_{ex})}} \cdot \frac{\int F_c(\lambda)d\lambda}{\int F_r(\lambda)d\lambda} \cdot \frac{n_c^2}{n_r^2}$$

where φ is quantum yield, $A(\lambda_{ex})$ is absorbance at the excitation wavelength λ_{ex} ($\lambda_{ex} = 440$ nm), F is fluorescence emission, n is refractive index of the solution (1.335 for DPBS at pH 7.40 and 1.3284 for methanol), and the subscripts ‘c’ and ‘r’ refer to the protein–chromophore complex measured and the reference dye, respectively. The reference dye Acridine Yellow G (in methanol) has a quantum yield value of 0.57 that was used²⁴.

Absolute quantum yield. An integrating sphere instrument (Hamamatsu C9920-12) (6 nm excitation bandwidth, 1 nm interval) and a high-sensitivity photonic multi-channel analyzer (Hamamatsu C10027-01) were used to measure a light emission spectrum. Absolute quantum yields were measured for solutions of protein–chromophore complexes in DPBS (pH 7.4) in which the protein was $\geq 95\%$ saturated with chromophore, producing ~ 1 μM protein–chromophore complex samples. Protein–chromophore complex samples and control samples were excited at 440 nm and absolute quantum yields were calculated according to the equation:

$$\Phi_c = \frac{f_{em}}{f_{abs}}$$

where f_{em} is the emitted photon flux and f_{abs} is the absorbed photon flux. The absolute quantum yields of the two control samples (Acridine Yellow G and fluorescein) agreed well with literature values^{24,52}.

COS-7 cell culture, transfection, and fixation

COS-7 cells (ATCC CRL-1651) were cultured, transfected, and fixed as described previously¹⁰.

Epifluorescence microscopy of COS-7 cells

Conventional widefield epifluorescence imaging of cultured live COS-7 cells and fixed COS-7 cells (Figure 5) was performed on an inverted Nikon Ti-S microscope as described previously¹⁰. For widefield epifluorescence microscopy of fixed COS-7 cells expressing mFAP2a or mFAP2b targeted to the endoplasmic reticulum (ER) (Figure 5), samples were labeled with either 40 μ M DFHBI or 40 μ M DFHBI-1T in 1x phosphate buffered saline (PBS, Fisher Scientific #BP399-1) (11.9 mM phosphates, 137 mM NaCl, 2.7 mM KCl, pH 7.4) for at least 10 minutes before imaging. Cells were rinsed three times with 1 mL of 1x PBS. Exposure times were 200 ms and current was 500 mA. For time-lapse widefield epifluorescence microscopy of live COS-7 cells expressing mFAP2a or mFAP2b targeted to the ER (data not shown), cells were labeled with 40 μ M DFHBI in 1x PBS. The time-lapse movies were acquired using 200 ms exposure times every 5 s for 25 total frames. Excitation current was 100 mA. The total acquisition duration per movie was just over 2 minutes, and movie playback speeds are 5 frames per second.

Photostability assay

COS-7 cells transfected with either pcDNA5/FRT/TO-AcGFP1-sec61 β , pcDNA5/FRT/TO-mFAP2a-sec61 β , or pcDNA5/FRT/TO-mFAP2b-sec61 β were fixed and imaged (Figure 6) at 25°C using a Zeiss LSM-510 laser scanning confocal fluorescence microscope equipped with a Plan-Apochromat 63x/1.4 oil DIC objective lens. The Argon/2 488 nm excitation laser was set to 50% output power (4.0 A tube current) and at 10% transmission resulting in 10.3 μ W laser power. The pinhole size was set to 98 μ m (1.02 Airy units). The excitation laser source passed through a HFT488 dichroic beam splitter to the specimen, and fluorescence captured through the HFT488 dichroic beam splitter to a 505 nm long-pass emission filter to the detector. Acquiring 740x740 pixel (71.43 μ m²) images with a single laser scan direction and 12-bit pixel depth resulted in a 1.13 s scantime and 0.8 μ s pixeltime for photostability assays. For all samples, amplifier offset was set to -1.0 and amplifier gain set to 1.0. For samples expressing AcGFP1-sec61 β , detector gain was set to 500. For samples expressing mFAP2a-sec61 β , detector gain was set to 800 for 50 μ M DFHBI labeling, 700 for 50 μ M DFHBI-1T labeling, and 900 for 0.5 μ M DFHBI and 0.5 μ M DFHBI-1T labeling. For samples expressing mFAP2b-sec61 β , detector gain was set to 700 for 50 μ M DFHBI labeling and 900 for 0.5 μ M DFHBI labeling. Fixed COS-7 cells expressing AcGFP1-sec61 β were imaged in Tris buffered saline (25 mM Tris, 300 mM NaCl, pH 8.0), and those expressing mFAP2a-sec61 β and mFAP2b-sec61 β were washed ten times with 50 μ L of high salt Tev protease buffer, and labeled with chromophore in high salt Tev protease buffer for at least 10 minutes prior to imaging. Raw “*.lsm” data files were analyzed with the pylsm python module (<https://pypi.org/project/pyLSM/>) and in-house scripts. For each region of interest encompassing

one or more fixed cells, normalized image intensity (Figure 6c,d) was calculated by summing image pixel intensities per frame and dividing by the summed image pixel intensities of the first frame. Pixel intensities at the bit depth of the microscope detector were discounted. Reported photostability relative to AcGFP1 was computed by non-linear least squares fitting of the average normalized image intensities to an exponential decay equation to obtain exponential decay constants.

Laser scanning confocal fluorescence microscopy of E. coli

Lemo21(DE3) *E. coli* cultures expressing either mFAP2a or mFAP2b were induced with 0.5 mM IPTG final concentration for 4 hours at 37°C shaking at 250 rpm. For imaging separate cultures (Figure 1f,g,h,i), 1.5% agarose pads supplemented with either 10 μ M DFHBI or 10 μ M DFHBI-1T final concentrations were moulded as previously described⁵³. 1 mL of induced cells was aliquoted from each culture, centrifuged, the pellet re-suspended in 1 mL of high salt Tev cleavage buffer, solution pelleted again, and the pellet re-suspended in 100 μ L of either 10 μ M DFHBI or 10 μ M DFHBI-1T (from 2 mM chromophore stock solutions in 5% DMSO and 95% high salt Tev cleavage buffer). 2 μ L of cells in chromophore solution were aliquoted onto \sim 1 cm² agarose pads containing the corresponding chromophore, and the agarose pad placed in μ -Slide 4 Well chambers (ibidi) for imaging.

For imaging mixed cultures (Figure 4), induced cultures were diluted 10-fold in ddH₂O and their optical density at 600 nm measured using a Genesys 10S UV-Vis spectrophotometer (Thermo Scientific). Proportional volumes of cell cultures expressing either mFAP2a or mFAP2b were mixed to achieve a 1:1 ratio of cells from each culture. 100 μ L of this mixture was

centrifuged, the pellet re-suspended in 200 μ L of high salt Tev cleavage buffer, solution pelleted again, and the pellet re-suspended in 10 μ L of either 10 μ M DFHBI or 10 μ M DFHBI-1T (from 2 mM chromophore stock solutions in 5% DMSO and 95% high salt Tev cleavage buffer), and incubated for 10 minutes at 25°C. 5 μ L of each cellular mixture in different chromophores was pipetted onto frosted microscope slides (Fisher Scientific) between Premium Superslip glass coverslips (Fisher Scientific).

Images were acquired on a Zeiss LSM-510 laser scanning confocal fluorescence microscope equipped with a Plan-Apochromat 63x/1.4 oil DIC objective lens. The Argon/2 488 nm excitation laser was set to 50% output power (4.0 A tube current) and at 10% transmission resulting in 10.3 μ W laser power. Pinhole size was set to 98 μ m (1.02 Airy units), and fluorescence was captured through a 505 nm long-pass emission filter. Detector gain was set to 650, amplifier offset was set to -0.85, and amplifier gain was set to 1.0. 740x740 pixel (71.43 μ m²) images (Figure 1f,g,h,i) or 1480x1480 pixel (142.86 μ m²) images (Figure 4) were acquired with a single laser scan direction and 12-bit pixel depth. Raw “*.lsm” data files were analyzed with the pylsm python module (<https://pypi.org/project/pyLSM/>) and in-house scripts. For Figure 4c, summed pixel intensities were calculated per image, including the pixel intensities at the bit depth of the microscope detector.

X-ray crystallography

EF1p2_mFAP2b was produced by large-scale protein purification, 6xHis-tag removal and SEC purification in Tris buffered saline (20 mM Tris, 300 mM NaCl, pH 7.4). Purified protein was mixed with excess DFHBI (re-suspended in 100% DMSO), while keeping the final DMSO

concentration <1%, followed by addition of 5 mM CaCl₂ final concentration. The EF1p2_mFAP2b–DFHBI complex was then concentrated to ~25 mg/mL, and initially tested for crystallization via sparse matrix screens in 96-well sitting drops using a mosquito (TTP LabTech). A single crystal was obtained in a 200 nL drop from 100 mM HEPES pH 7.5 and 25% PEG 3350 (Index, Hampton Research). The drop was flooded with reservoir solution plus 2 mM DFHBI and 20% ethylene glycol then flash frozen in liquid nitrogen. Data was collected with a home-source rotating anode on a Saturn 944+ CCD and processed in HKL2000⁵⁴. For phasing and refinement, structures were solved by Molecular Replacement with Phaser via phenix^{55,56} using a mFAP2b design model from Rosetta²⁷ with appropriate residue side-chains cut back to C_α atoms and DFHBI and loop7 residues removed. The structure was then built and refined using Coot⁵⁷ and phenix⁵⁸, respectively (Table 4).

Molecular dynamics (MD) simulations

Chain B of the resolved EF1p2_mFAP2b–DFHBI–Ca²⁺ co-crystal structure (PDB ID 6OHH) was used as the starting point for MD simulations. The other three system conditions were obtained by removing the coordinates of the Ca²⁺ ion and DFHBI ligand (Apo), or either that of the ion or of the ligand (DFHBI-bound and Ca²⁺-bound conditions, respectively). Missing side chains were added using Schrödinger's Maestro (version 10.4, Schrödinger, LLC, New York, NY) and all crystallographic waters were kept. Protonation states at pH 7 were assigned using Maestro's PROPKA. The accessible protein cavities left by the removal of the ligand in the Apo and Ca²⁺-bound systems were hydrated with Dowser⁵⁹. Proteins were solvated in TIP3P water boxes⁶⁰ with a buffer distance of 16 Å to the box edges and NaCl ions were added to

provide charge neutrality at a total concentration of 150 mM. The Amber14SB force field^{61,62} was used for the protein and NaCl. The DFHBI ligand was parametrized using Antechamber and the generalized Amber Force Field (GAFF)^{63,64}, with geometry optimization performed with Gaussian 09⁶⁵. Ca²⁺ parameters were obtained from Bradbrook *et al*⁶⁶.

The systems were minimized in five stages with increasing number of unconstrained atoms (proton only, solvent, ligand, side-chains, and the full system) totaling 13,000 steps of steepest descent and conjugate gradient methods. This was followed by equilibration involving an initial heating to 100 K at constant volume for 50 ps followed by heating to 298 K at a constant pressure of 1 bar for 200 ps. The systems were further equilibrated at 298 K and 1 bar for 2.25 ns. Production runs were performed using GPU accelerated Amber14^{62,67} at 1 bar and 298 K with periodic boundary conditions and a 2 fs timestep, with non-bonded short-range interactions evaluated within a cutoff of 10 Å. Each of the four system conditions were simulated in three independent 500 ns replicates. The first 100 ns of each production run were disregarded from analysis to allow for adequate structural relaxation from the starting conformation. The trajectories were visualized in VMD⁶⁸ and aligned to the protein crystal structure. The protein backbone atom coordinates were used to probe the conformational free energy landscape using PyEMMA⁶⁹ and in-house scripts. The loop7 residues coordinates of all simulations were jointly clustered into 25 clusters, resulting in whole protein cluster centroids with an average backbone heavy atom root mean square distance (RMSD) of 2.49 Å to each other. Clustering was performed on loop7 backbone coordinates using the PyEMMA k_means algorithm, and each cluster centroid structure was defined as the structure which minimized the sum of the RMSD

values to all other cluster members. CPPTRAJ⁷⁰ and MDTraj⁷¹ were used for RMSF and RMSD analysis.

HEK293 cell transfections

Closed circular plasmid DNAs were purified in ddH₂O for transfections. pGP-CMV-GCaMP6f was a gift from Douglas Kim & GENIE Project (Addgene plasmid #40755; RRID: Addgene_40755). Wild-type HEK293 cells (ATCC CRL-1573) were cultured on 24-well plates in DMEM media (4.5 g/L D-glucose, L-glutamine, ThermoFisher catalog #11965-092) supplemented with 10% fetal bovine serum (FBS) and 1% Penicillin/Streptomycin in a 5% CO₂ atmosphere at 37°C. Cells were seeded into 24-well plates (ThermoFisher catalog #FB012929) at 100,000 cells/well. 24 hours after seeding, cell media was aspirated and replaced with 200 µL of DMEM media. Lipofectamine 3000 (ThermoFisher Scientific) reagents were prepared according to the manufacturer's instructions by mixing 1.5 µL of Lipofectamine 3000 reagent diluted in 25 µL of OPTI-MEM with 1 µg of plasmid DNA diluted in 25 µL OPTI-MEM and 2 µL of P3000 reagent, allowing for formation of DNA–lipid complexes for approximately 10 minutes. Reagent volumes were increased to meet the number of wells to be transfected. 50 µL of complexed lipofectamine reagents were pipetted into each well, cells were incubated for 30 minutes, and the volume in each well was raised to 750 µL with DMEM media. Approximately six hours after transfection, media was replaced with 1 mL of DMEM media. Cells were incubated for 48 hours to allow for protein expression.

HEK293 cell Ca²⁺ titrations

Ca²⁺ titration protocol. A stock solution of DFHBI was prepared in anhydrous DMSO at 20 mM concentration. Two days after the transfection of pDisplay-EF1p_mFAP2b, each 24-well plate well was rinsed twice with pre-warmed Ca²⁺-deficient Tyrode's solution (124 mM NaCl, 2 mM KCl, 2 mM MgCl₂, 10 mM HEPES and 10 mM glucose, pH between 7.3-7.4 with NaOH), then filled with 200 μL of the same solution containing 7 μM DFHBI (approximately $(K_d^+ \cdot K_d^-)^{1/2}$ for EF1p_mFAP2b, Table 3). Cells were incubated (5% CO₂ at 37°C) in the dark for 5 minutes before the Ca²⁺ titration to allow DFHBI to reach equilibrium with the sensor. Cells were imaged at 5 frames/s for 1 minute with a sCMOS camera (Photometrics Prime95B) and a 20x magnification lens (Leica HCX PL FLUOTAR L 20X/0.40 NA CORR). The cells were continually illuminated at 7.65 mW/cm² with a LumenCor Light Engine (Semrock filters: Excitation 474/27 nm; Emission 520/35 nm). 20 s into the imaging experiment, a syringe pump (Harvard Apparatus Pump 11 Elite) was triggered by a TTL pulse. 200 μL of 20 mM Ca²⁺ Tyrode's solution (84 mM NaCl, 2 mM KCl, 2 mM MgCl₂, 20 mM CaCl₂, 10 mM HEPES and 10 mM glucose, pH between 7.3-7.4 with NaOH) with the identical DFHBI concentration was added at a rate of 2 mL/minute to the wells. The final conditions of each well were 400 μL volume of 10 mM Ca²⁺ with constant 7 μM DFHBI concentration throughout the end of the experiment. "After Photobleaching" (see Figure 19d) cells in a different region of interest (ROI) were illuminated for the same duration and imaging conditions used for each imaging experiment prior to the titration experiment.

Data analysis. Regions of interest (ROIs) surrounding single cells were hand-drawn in ImageJ software⁷². For each cellular ROI in each frame the average fluorescence was calculated

in ImageJ. In order to perform background subtraction, cellular ROIs were then moved proximal to the original cell to an ROI where there was no fluorescence. Each cellular ROI average fluorescence had the average background intensity subtracted for each frame. Following background subtraction, change in fluorescence was calculated by the following formula:

$$\frac{\Delta F}{F_0} = \frac{F - F_0}{F_0}$$

where F is the background-subtracted average fluorescence per ROI per frame, and F_0 is the background-subtracted average baseline fluorescence as measured one second prior to the Ca^{2+} titration⁴¹ (Figure 19d).

HEK293 cell acetylcholine stimulations

Stimulation protocol. All DFHBI solutions were prepared using an anhydrous 100% DMSO stock solution of 20 mM DFHBI. The media was aspirated from the wells and the cells were rinsed once with 200 μL of Tyrode's solution (120 mM NaCl, 2 mM KCl, 2 mM MgCl_2 , 2 mM CaCl_2 , 10 mM HEPES, 10 mM glucose, pH adjusted to 7.3-7.4 using NaOH). Cells were placed in 750 μL Tyrode's solution supplemented with 20 μM DFHBI for EF2n_mFAP2a-expressing cells, 43.3 μM DFHBI (from a 20 mM DFHBI stock solution in 100% DMSO) for EF4n_mFAP2a-expressing and EF4n_mFAP2b-expressing cells. GCaMP6f-expressing cells were placed in 750 μL Tyrode's solution. Cells were placed in the dark at 37°C for 30 minutes prior to stimulation. Imaging was performed on a Leica DMI8 microscope controlled by MetaMorph Imaging software. Cells were imaged at 5 frames/s for 1 minute with a sCMOS camera (Photometrics Prime95B) and a 20x magnification lens (Leica

HCX PL FLUOTAR L 20X/0.40 NA CORR). The cells were continually illuminated at 7.65 mW/cm² with a LumenCor Light Engine (Semrock filters: Excitation 474/27 nm; Emission 520/35 nm). 20 s into the imaging experiment, a syringe pump (Harvard Apparatus Pump 11 Elite) was triggered by a TTL pulse. 100 μL of Tyrode's solution spiked with the identical DFHBI concentration (and % DMSO) and 850 μM acetylcholine (ACh) was added at a rate of 2 mL/minute to the wells. The final conditions of each well were 850 μL volume of 100 μM ACh with constant DFHBI concentration throughout the addition of ACh stimulation solution.

Data analysis. Regions of interest (ROIs) surrounding single cells were hand-drawn in ImageJ software⁷². For each cellular ROI in each frame the average fluorescence was calculated in ImageJ. In order to perform background subtraction, cellular ROIs were then moved proximal to the original cell to an ROI where there was no fluorescence. Each cellular ROIs average fluorescence had the corresponding background fluorescence subtracted for each frame. Following background subtraction, change in fluorescence was calculated by the following formula:

$$\frac{\Delta F}{F_0} = \frac{F - F_0}{F_0}$$

where F is the background-subtracted average fluorescence per ROI per frame, and F_0 is the background-subtracted average baseline fluorescence as measured one second prior to ACh stimulation⁴¹. A maximal fluorescence response (i.e. the peak $|\frac{\Delta F}{F_0}|$) was determined as the maximum absolute value of the fluorescence fold-change after the stimulation frame, and the two-sided Wilcoxon rank sum test was used to compare values (Figure 21).

Human induced pluripotent stem cell (hiPSC)-derived cardiomyocyte (CM) imaging

hiPSC culture and cardiomyocyte differentiation. Undifferentiated IMR90 hiPSCs (WiCell) were maintained in mTeSR-1 (StemCell Technologies) on tissue culture plastic coated with Matrigel diluted 1:60 (Corning) at 37°C and 5% CO₂. Cardiomyocytes were differentiated using a monolayer-based directed differentiation protocol as previously described⁷³. hiPSCs were dissociated into a single cell suspension using Versene (Life Technologies) and plated at a high density ($1.5\text{-}2.5 \cdot 10^5$ cells·cm⁻²) in mTeSR containing 10 μM Y-27632 ROCK inhibitor onto Matrigel-coated plates. 24 hours after plating, media was replaced with fresh mTeSR. 48 hours after seeding, differentiation was induced by changing the media to 10-12 μM CHIR 99021 (Stemgent) in RPMI 1640 supplemented with B27 minus insulin (RPMI-ins, ThermoFisher). After 24 hours post-induction, the media was changed to fresh RPMI-ins. At 3 days post-induction, the media was changed to 3-5 μM IWP4 (Stemgent) in RPMI-ins. At 5 days post-induction, the media was changed to fresh RPMI-ins. At 7 days post-induction, the media was changed to RPMI medium containing B27 supplement with insulin (RPMI+ins), and media was changed every other day. Cardiomyocytes were replated at day 14 post-induction in RPMI+ins at $1.5 \cdot 10^5$ cells·cm⁻². Cardiomyocytes were then purified via metabolic challenge by culturing in DMEM without glucose or sodium pyruvate, supplemented with 4 mM sodium L-lactate for 4 days⁷⁴.

Recombinant adeno-associated virus (rAAV) production and infection of hiPSC CMs.

AAV-CAG-hChR2-H134R-tdTomato was a gift from Karel Svoboda (Addgene plasmid # 28017; RRID:Addgene_28017), the vector backbone into which the EF1n_mFAP2b gene with sarcoplasmic reticulum (SR) localization sequence was subcloned. rAAV serotype 6 (rAAV6)

were produced using previously described methods⁷⁵. Titers for rAAV6-SR-EF1n_mFAP2b were $2.90 \cdot 10^{13}$ viral genomes/mL. Purified hiPSC-derived CMs in 6-well plates were infected with 3 μ L of the EF1n-mFAP2b rAAV6 construct at 30 days post-induction. Cardiomyocytes were incubated for 5 days before imaging. RPMI+ins media was replenished every 2 days without exchanging media.

Contraction and SR Ca²⁺ transient imaging. Leica DMI8 microscope controlled by MetaMorph Imaging software was used to image contraction and calcium transients of the sarcoplasmic reticulum in cardiomyocytes. Prior to imaging experiments, cardiomyocytes were rinsed with Tyrode's solution and the 6-well plate wells were filled with 2 mL of Tyrode's solution with 6 μ M DFHBI (Figure 19f) or 3 μ M DFHBI (Figure 22b) from the stock solution. Cardiomyocytes were imaged at ~ 16.7 Hz (60 ms per frame) for up to 24 seconds with a sCMOS camera (Photometrics Prime95B) and a 20x magnification lens (Leica HCX PL FLUOTAR L 20X/0.40 NA CORR). The cells were continually illuminated at 5.72 mW/cm² (Figure 19f) or 15.8 mW/cm² (Figure 22b,c) with a LumenCor Light Engine (Semrock filters: Excitation 474/27 nm; Emission 520/35 nm). For mapping contraction, 3 different ROIs were hand-drawn, and displacement of cells were measured in the fluorescence channel. The normalized mean of the 3 traces is plotted to visualize contraction of cardiomyocytes (Figure 19f, Figure 22b). In order to quantify tissue-level Ca²⁺ ion fluxes during cardiac contraction, fluorescence fold-change over the whole field of view was calculated for each frame then temporally matched with contraction data. Fluorescence fold-change in each frame was calculated by the following formula:

$$\frac{\Delta F}{F_0} = \frac{F - F_0}{F_0}$$

where F is the fluorescence per frame, and F_0 is the fluorescence of the frame with the minimum fluorescence (Figure 19f, Figure 22b).

Pharmacological inhibition of SERCA Ca^{2+} pumps. Cardiomyocytes in 2 mL of Tyrode's solution labeled with 3 μ M DFHBI were imaged at 2 Hz for 30 minutes with an sCMOS camera (Photometrics Prime95B) and a 20x magnification lens (Leica HCX PL FLUOTAR L 20X/0.40 NA CORR). A stock solution of 20 mM cyclopiazonic acid (Tocris, 1235) in anhydrous DMSO was prepared. 2 mL of Tyrode's solution containing 3 μ M DFHBI and 40 μ M cyclopiazonic acid (CPA) was administered at approximately 10 minutes from initial image acquisition to inhibit SERCA pumps and disrupt Ca^{2+} ion recovery into the SR after contraction⁴³. In order to quantify the change of Ca^{2+} ion levels after inhibition of SERCA pumps, an average value for fluorescence intensity of the field of view was calculated for each frame. Fold-change in fluorescence in each frame was calculated by the following formula:

$$\frac{\Delta F}{F_0} = \frac{F - F_0}{F_0}$$

where F is the fluorescence per frame, and F_0 is the fluorescence of the frame with the minimum fluorescence (Figure 22c).

4.3. Code Availability

The Rosetta macromolecular modeling suite (<https://www.rosettacommons.org>) is freely available to academic/non-commercial users and commercial licenses are available via the University of Washington Technology Transfer Office. The Rosetta design protocol for the extended loop library is available below. The sequence design protocol to generate the

combinatorial library of amino acid linker sequences to graft one EF-hand motif onto loop7 of mFAP2b is also available below.

Custom RosettaScripts XML script used to design extended loops onto loop7 of mFAP2b:

Rosetta build specifications:

Git tag: v2018.12-dev60119

Operating system: Linux

Compiler: gcc (Ubuntu 5.4.0-6ubuntu1~16.04.4) 5.4.0 20160609

Example RosettaScripts²⁶ command line:

```
~Rosetta/main/source/bin/rosetta_scripts.hdf5.linuxgccrelease  
@flags -s mFAP2b.pdb -parser:script_vars  
bp=mFAP2b_cutpoints_71_77_L3A_0035.bp
```

Example blueprint file (e.g. mFAP2b_cutpoints_71_77_L3A_0035.bp):

```
1 S LE .  
2 R HA .  
3 A HA .  
4 A HA .  
5 Q HA .  
6 L HA .  
7 L LA .  
8 P LB .  
9 G EE .  
10 T EB .  
11 W EB .  
12 Q EB .  
13 V EB .  
14 T EB .  
15 M EB .  
16 T EB .  
17 N EB .  
18 E LA .
```

19 D LA .
20 G LG .
21 Q LB .
22 T EB .
23 S EB .
24 Q EB .
25 G EE .
26 Q EB .
27 W EB .
28 H EB .
29 F EB .
30 Q EB .
31 P EB .
32 R EA .
33 S EB .
34 P LA .
35 Y LA .
36 T EB .
37 M EB .
38 D EB .
39 I EB .
40 V EB .
41 A EB .
42 Q EB .
43 G EE .
44 T EB .
45 I EB .
46 S LG .
47 D LG .
48 G LG .
49 R EB .
50 P EB .
51 I EB .
52 V EB .
53 G EB .
54 Y EB .
55 G EB .
56 K EB .
57 A EB .
58 T EB .
59 V EB .
60 K EA .
61 T EB .
62 P LA .
63 D LA .

64 T EB .
65 L EB .
66 D EB .
67 I EB .
68 D EB .
69 I EB .
70 T EB .
71 Y EB R
0 E LE R
0 G EB R
0 K LA R
0 S LB R
0 G HE R
0 S HA R
0 L HA R
0 A EB R
0 G LG R
0 S LB R
0 K LB R
0 I LO R
77 I EB R
78 K EB .
79 A EB .
80 Q EB .
81 G EE .
82 Q EB .
83 I EB .
84 T EB .
85 M EB .
86 D EA .
87 S EB .
88 P LA .
89 T LA .
90 Q EB .
91 F EB .
92 K EB .
93 W EB .
94 D EB .
95 A EB .
96 T EB .
97 T LA .
98 K LB .
99 G LG .
100 E LB .
101 N LE .

102 D LA .
103 F LB .
104 H LB .
105 G LE .
106 R EB .
107 L EB .
108 T EB .
109 G EB .
110 T EB .
111 L EB .
112 Q EB .
113 R EB .
114 Q LB .
115 E LO .
116 Z L .

Example RosettaScripts²⁶ command line flags file:

```
-parser:protocol blueprintbdr.xml  
-out:level 100  
-out:path:all output  
-scorefile score.sc  
-extra_res_fa HBI.fa.params  
-overwrite  
-write_all_connect_info 1  
-run::preserve_header  
-connect_info_cutoff 3.0  
-nblast_autoupdate  
-jd2:ntrials 1  
-packing::use_input_sc 1  
-packing::extrachi_cutoff 1  
-packing::ex1  
-packing::ex2  
-linmem_ig 10  
-parser_read_cloud_pdb 1  
-ignore_unrecognized_res  
-no_optH false  
-flip_HNQ  
-no_his_his_pairE  
-enzdes:detect_design_interface  
-chemical:exclude_patches LowerDNA UpperDNA Cterm_amidation  
VirtualBB ShoveBB VirtualDNAPhosphate VirtualNTerm CTermConnect  
sc_orbitals pro_hydroxylated_case1 pro_hydroxylated_case2  
ser_phosphorylated thr_phosphorylated tyr_phosphorylated
```

```

tyr_sulfated lys_dimethylated lys_monomethylated
lys_trimethylated lys_acetylated glu_carboxylated cys_acetylated
tyr_diiiodinated N_acetylated C_methylamidated
MethylatedProteinCterm
-holes:dalphaball DAlphaBall.gcc

```

*RosettaScripts*²⁶ XML script to build extended loop7 designs (e.g. blueprintbdr.xml):

```

<ROSETTASCRIPTS>
  <SCOREFXNS>
    <ScoreFunction name="default_cart" weights="ref2015_cart.wts" />
    <ScoreFunction name="default_score3" weights="score3.wts" />
  </SCOREFXNS>
  <RESIDUE_SELECTORS>
    <ResidueName name="ligand" residue_name3="HBI" />
    <Not name="protein" selector="ligand" />
    <Layer name="core" select_core="true" core_cutoff="4.0" />
  </RESIDUE_SELECTORS>
  <TASKOPERATIONS>
    <InitializeFromCommandline name="init" />
    <IncludeCurrent name="ic" />
    <LimitAromaChi2 name="limchi2" include_trp="1" />
    <ExtraRotamersGeneric name="ex1_2"
      ex1="1" ex2="1" ex3="0" ex4="0"
      ex1aro="1" ex2aro="1" ex1aro_exposed="0"
      ex2aro_exposed="0"
      ex1_sample_level="1" ex2_sample_level="1"
      ex3_sample_level="0" ex4_sample_level="0"
      ex1aro_sample_level="1" ex2aro_sample_level="1"
      ex1aro_exposed_sample_level="0"
      ex2aro_exposed_sample_level="0"
      extrachi_cutoff="24"/>
    <RestrictToRepacking name="repack_only" />
    <OperateOnResidueSubset name="prevent_repacking" selector="ligand" >
      <PreventRepackingRLT/>
    </OperateOnResidueSubset>
    <OperateOnResidueSubset name="restrict_to_repacking" selector="protein" >
      <RestrictToRepackingRLT/>
    </OperateOnResidueSubset>
  </TASKOPERATIONS>
  <MOVERS>
    <PackRotamersMover name="repack" scorefxn="default_cart"
      task_operations="init,ic,limchi2,ex1_2,repack_only" />
  </MOVERS>
  <FILTERS>
    <ScoreType name="total_score" scorefxn="default_cart"
      score_type="total_score" threshold="1000" confidence="0"/>
    <ScoreType name="p_aa_pp" scorefxn="default_cart" score_type="p_aa_pp"
      threshold="1000" confidence="0"/>
    <ScoreType name="chainbreak" scorefxn="default_cart"
      score_type="linear_chainbreak" threshold="1000" confidence="0"/>

```

```

    <ScoreType name="omega" scorefxn="default_cart" score_type="omega"
threshold="1000" confidence="0"/>
    <ScoreType name="cart_bonded" scorefxn="default_cart"
score_type="cart_bonded" threshold="1000" confidence="0"/>
    <ResidueCount name="nres" confidence="0" />
    <CalculatorFilter name="total_score_res" confidence="0"
equation="SCORE/NRES" threshold="-3.2" >
    <Var name="SCORE" filter_name="total_score" />
    <Var name="NRES" filter_name="nres" />
</CalculatorFilter>
    <Geometry name="geometry" omega="165" cart_bonded="20" start="1"
end="100000" confidence="0" />
    <ShapeComplementarity name="SC" min_sc="0" min_interface="0" verbose="0"
quick="0" jump="1" residue_selector1="protein" residue_selector2="ligand"
write_int_area="0" confidence="0" />
    <RepackWithoutLigand name="rwl" scorefxn="default_cart"
target_res="all_repacked" rms_threshold="1.5" confidence="0" />
    <DSasa name="dsasa" lower_threshold="0.0" upper_threshold="1.0"
confidence="0" />
    <PackStat name="pstat" chain="0" threshold="0.60" confidence="0" />
    <Holes name="holes" threshold="1.8" residue_selector="core"
normalize_per_atom="true" exclude_bb_atoms="true" confidence="0" />
    <BuriedUnsatHbonds name="buns" scorefxn="default_cart"
residue_surface_cutoff="15.0" ignore_surface_res="true"
print_out_info_to_pdb="true" confidence="0"/>
    <BuriedUnsatHbonds name="buns_sc_heavy" use_reporter_behavior="true"
report_sc_heavy_atom_unsats="true" scorefxn="default_cart"
residue_surface_cutoff="15.0" ignore_surface_res="true"
print_out_info_to_pdb="true" confidence="0"/>
    <BuriedUnsatHbonds name="buns_bb_heavy" use_reporter_behavior="true"
report_bb_heavy_atom_unsats="true" scorefxn="default_cart"
residue_surface_cutoff="15.0" ignore_surface_res="true"
print_out_info_to_pdb="true" confidence="0"/>
    <BuriedUnsatHbonds name="buns_all_heavy" use_reporter_behavior="true"
report_all_heavy_atom_unsats="true" scorefxn="default_cart"
residue_surface_cutoff="15.0" ignore_surface_res="true"
print_out_info_to_pdb="true" confidence="0"/>
    <BuriedUnsatHbonds name="buns_nonheavy" use_reporter_behavior="true"
report_nonheavy_unsats="true" scorefxn="default_cart"
residue_surface_cutoff="15.0" ignore_surface_res="true"
print_out_info_to_pdb="true" confidence="0"/>
    <ScoreType name="rama" score_type="rama" scorefxn="default_cart"
threshold="0" confidence="0" />
    <LigInterfaceEnergy name="interfE" scorefxn="default_cart"
energy_cutoff="0.0" confidence="0" />
    <Ddg name="ddg_complex" scorefxn="default_cart" threshold="0" jump="1"
repeats="3" relax_mover="repack" confidence="0" />
    <PreProline name="prepro" use_statistical_potential="0" confidence="0"/>
    <ResidueCount name="ala_count" max_residue_count="30" residue_types="ALA"
confidence="0"/>
    <ResidueCount confidence="0" name="TYR" residue_types="TYR"/>
    <ResidueCount confidence="0" name="TRP" residue_types="TRP"/>
    <ResidueCount confidence="0" name="PHE" residue_types="PHE"/>
    <ResidueCount confidence="0" name="MET" residue_types="MET"/>

```

```

<ResidueCount confidence="0" name="HIS" residue_types="HIS"/>
<ResidueCount confidence="0" name="ARG" residue_types="ARG"/>
<ResidueCount confidence="0" name="LYS" residue_types="LYS"/>
<ResidueCount confidence="0" name="ASP" residue_types="ASP"/>
<ResidueCount confidence="0" name="GLU" residue_types="GLU"/>
<ResidueCount confidence="0" name="SER" residue_types="SER"/>
<ResidueCount confidence="0" name="THR" residue_types="THR"/>
<ResidueCount confidence="0" name="ASN" residue_types="ASN"/>
<ResidueCount confidence="0" name="GLN" residue_types="GLN"/>
<ResidueCount confidence="0" name="CYS" residue_types="CYS"/>
<ResidueCount confidence="0" name="GLY" residue_types="GLY"/>
<ResidueCount confidence="0" name="PRO" residue_types="PRO"/>
<ResidueCount confidence="0" name="VAL" residue_types="VAL"/>
<ResidueCount confidence="0" name="ILE" residue_types="ILE"/>
<SSShapeComplementarity name="ss_sc" verbose="0" loops="1" helices="1"
confidence="0" />
</FILTERS>
<MOVERS>
  <BlueprintBDR name="bdr" blueprint="%%bp%%" use_abego_bias="1"
use_sequence_bias="1" scorefxn="default_score3"/>
  <FastRelax name="fast_relax" scorefxn="default_cart" repeats="1"
task_operations="init,ic,limchi2,ex1_2,prevent_repacking,restrict_to_repacking
"
      batch="0" ramp_down_constraints="0"
      cartesian="1" bondangle="1" bondlength="1"
      min_type="lbfgs_armijo_nonmonotone" >
    <MoveMap>
      <Chain number="1" chi="1" bb="1" />
      <Chain number="2" chi="0" bb="0" />
    </MoveMap>
  </FastRelax>
  <GenericMonteCarlo name="gmc" mover_name="fast_relax"
filter_name="total_score_res" trials="5" sample_type="low" temperature="0.62"
drift="1" recover_low="1" preapply="1">
    <Filters>
      <AND filter_name="SC" temperature="0.62" sample_type="high" rank="0"/>
    </Filters>
  </GenericMonteCarlo>
</MOVERS>
<APPLY_TO_POSE>
</APPLY_TO_POSE>
<PROTOCOLS>
  <Add mover="bdr" />
  <Add mover="gmc" />
  <Add filter="TYR" />
  <Add filter="TRP" />
  <Add filter="PHE" />
  <Add filter="MET" />
  <Add filter="HIS" />
  <Add filter="ARG" />
  <Add filter="LYS" />
  <Add filter="ASP" />
  <Add filter="GLU" />
  <Add filter="SER" />

```

```

<Add filter="THR" />
<Add filter="ASN" />
<Add filter="GLN" />
<Add filter="CYS" />
<Add filter="GLY" />
<Add filter="PRO" />
<Add filter="VAL" />
<Add filter="ILE" />
<Add filter="ala_count" />
<Add filter="prepro" />
<Add filter="ss_sc" />
<Add filter="holes" />
<Add filter="p_aa_pp" />
<Add filter="chainbreak" />
<Add filter="omega" />
<Add filter="cart_bonded" />
<Add filter="total_score" />
<Add filter="total_score_res" />
<Add filter="nres" />
<Add filter="geometry" />
<Add filter="SC" />
<Add filter="ddg_complex" />
<Add filter="interfE" />
<Add filter="rwl" />
<Add filter="dsasa" />
<Add filter="pstat" />
<Add filter="rama" />
<Add filter="holes" />
<Add filter="buns" />
<Add filter="buns_sc_heavy" />
<Add filter="buns_bb_heavy" />
<Add filter="buns_all_heavy" />
<Add filter="buns_nonheavy" />
</PROTOCOLS>
<OUTPUT />
</ROSETTASCRIPTS>

```

Python script to design combinatorial library of amino acid linker sequences for grafting one EF-hand motif onto loop7 of mFAP2b:

Before running this python script, install the biopython python module:

```
conda install -c bioconda biopython=1.72
```

To download the script as a Jupyter Notebook (Supplementary_Note_3.ipynb):

```
git clone https://github.com/klimaj/mFAPs.git
```

4.4. Data Availability

The atomic coordinates and experimental data of EF1p2_mFAP2b–DFHBI–Ca²⁺ co-crystal structure have been deposited in the RCSB Protein Data Bank with the accession number 6OHH. Primary amino acid sequences of mFAP variants characterized herein are reported in Section 2.3 and Section 3.3. Plasmid DNA and the data that support the findings of this study are available upon reasonable request. Computational design models for the 59 extended loop decoys, 5 refined extended loop7 decoys, and mFAP2a and mFAP2b decoys are available to download, and β -barrel loop fragment databases used to design the extended loop library are available to download (<https://github.com/klimaj/mFAPs>).

4.5. Acknowledgements

J.C.K. would like to thank G. Reggiano for help extracting loops as .pdb files in designing the extended loop library, and D. Baker, J.B. Hurley, A. Nath, J. Bai, W.N. Zagotta, C.A. Smith, M.S. Glaz, L. Stewart, N.M. Ennist, H. Park, H. Shen and other members of the Baker laboratory for discussions. J.C.K. was supported by a National Science Foundation Graduate Research Fellowship (grant DGE-1256082). Part of this work was conducted at the Molecular Analysis Facility, a National Nanotechnology Coordinated Infrastructure site at the University of Washington which is supported in part by the National Science Foundation (grant NNCI-1542101), the University of Washington, the Molecular Engineering & Sciences Institute,

the Clean Energy Institute, and the National Institutes of Health. The Berkeley Center for Structural Biology is supported in part by the National Institutes of Health, National Institute of General Medical Sciences, and the Howard Hughes Medical Institute. The Advanced Light Source is a Department of Energy Office of Science User Facility under Contract No. DE-AC02-05CH11231. Any opinions, findings, and conclusions or recommendations expressed in this material are those of the author and do not necessarily represent the official views of the funding agencies.

4.6. Author Contributions

J.C.K., A.A.V., J.D., and D.B designed the research. J.C.K. performed: library assembly and screening; *in vitro* chromophore, pH, and Ca²⁺ titrations; fluorescence intensity assays and densitometry; laser scanning confocal fluorescence microscopy of *E. coli*; photostability assays on fixed COS-7 cells; and circular dichroism. J.C.K., J.D., C.M.C. and L.C. purified proteins. M.Y.L. measured quantum yields. L.A.G. cultured, transfected, and fixed COS-7 cells, and performed epifluorescence microscopy of live and fixed COS-7 cells. L.A.D. performed X-ray crystallography. E.P.B. performed molecular dynamics simulations. J.H.L. and M.R. cultured and transfected HEK293 cells. J.H.L. performed epifluorescence microscopy of HEK293 cell Ca²⁺ titrations. M.R. performed epifluorescence microscopy of HEK293 cell ACh stimulations. S.B. cultured and differentiated hiPSCs into CMs. J.H.L. cultured, infected, and performed epifluorescence microscopy of hiPSC-derived CMs. A.A.V. curated the β -barrel loop fragment databases and grafted them onto b11 and b32; J.D. designed mFAP2.0.1 and mFAP2.1; and

J.C.K. designed all other proteins. D.B., B.L.S., A.B., J.C.V., R.E.A., and D.L.M. supervised research.

4.7. Competing Interests

J.C.K., A.A.V., J.D., and D.B. are inventors on a U.S. patent application submitted by the University of Washington that covers the described methods, sequences and applications.

Chapter 5. Conclusion and Future Directions

In Chapter 2 we demonstrated that optimization of mFAPs resulted in two highly fluorogenic proteins (mFAP2a and mFAP2b) in the presence of DFHBI and/or DFHBI-1T. We showed that the mFAPs are more photostable than the EGFP variant AcGFP1. We identified mutations that produce a pH-responsive protein–chromophore pair (the mFAP_pH–DFHBI complex) that can be used for real-time pH quantification using ratiometric fluorescence microscopy. In Chapter 3 we also showed that insertions of Ca²⁺ ion binding motifs into a loop of the β -barrel produced Ca²⁺-responsive protein–chromophore pairs that can be used as fluorescent Ca²⁺ biosensors.

Because mFAPs can be used as a versatile platform for protein sensor engineering, it is furthermore proposed that the different amino acid sequence variants of the mFAP system can be combined in a modular way. For example, because it is known that mFAP2a binds DFHBI-1T, it follows that the mFAP2a-based Ca²⁺-responsive mFAPs (named “EF*_mFAP2a”) could be used with DFHBI-1T to detect Ca²⁺ ion fluxes. As another example of the modularity of the new protein sensor engineering platform, because mFAP2b with the (W27M, W93F) mutations is mFAP_pH which exhibits the ability to bind both the protonated and deprotonated states of DFHBI, it follows that the mFAP2b-based Ca²⁺-responsive mFAPs (named “EF*_mFAP2b”) with the additional (W27M, W93F) mutations incorporated could be used simultaneously quantify pH (via ratiometric fluorescence measurements) and report Ca²⁺ ion concentration changes (via intensimetric fluorescence measurements). Additionally, the mFAP3 core mutations known to promote low-level binding of the chromophore DFHO could be implemented in any of the Ca²⁺-responsive mFAPs for an orange-red colored fluorescence

readout of Ca^{2+} ion concentration changes. Moreover, due to the promiscuity of EF-hand motifs for binding Ca^{2+} , La^{3+} , Tb^{3+} , and other ions³⁷, the Ca^{2+} -responsive mFAPs could be used for real-time detection of Ca^{2+} , La^{3+} , Tb^{3+} , and other ion transients. mFAPs also have considerable potential to be optimized to bind DFHBI-derived chromophores with different fluorescence spectra with high affinity and brightness. Additionally, mFAPs could be used as modular fluorescent biosensors for detection and quantification of, in principle, any small molecule, ion, peptide, or nucleic acid by insertion of the respective binding motif into the loops of mFAPs. Finally, circularly permuted variations²³ of mFAPs and split versions of mFAPs (i.e. split into two or more separate peptides for later assembly) can result in similar and new functions and fluorescence properties compared to those outlined in Chapters 2 and 3. Additionally, in principle mFAPs could be engineered to monitor the presence of one, two, or more small molecules, ions, peptides, proteins, nucleic acid, and/or substrates simultaneously.

Beyond detection of analyte concentration changes using mFAPs, quantification of analyte concentrations using mFAPs requires generating an accurate calibration curve establishing mFAP fluorescence intensities versus known analyte concentrations at a fixed chromophore concentration. Because the mFAP fluorescence intensity depends on cellular mFAP expression level (i.e. the number of mFAP molecules present per volume imaged), quantification of analyte concentrations requires normalizing the mFAP fluorescence signal to the cellular mFAP expression level. This is accomplished via covalently fusing the mFAP to a fluorescent protein of dissimilar color to the mFAP–chromophore complex (such as the red fluorescent protein mCherry in the case of the mFAP2b–DFHBI complex). To normalize for the cellular mFAP expression levels imaged per pixel, the mFAP fluorescence signal can be divided by the

fluorescence signal of the covalently fused fluorescent protein imaged per pixel. After normalizing for cellular mFAP expression levels, the calibration curve obtained *in vitro* at a fixed chromophore concentration can be used to accurately quantify analyte concentrations *in situ* in real-time using an identical chromophore concentration. Use of a carefully generated *in vitro* calibration curve and *in situ* chromophore labeling protocol should be emphasized because, due to the thermodynamic coupling between analyte and chromophore binding, the analyte affinity for the biosensor changes as the chromophore concentration changes (Figure 17).

The future prospects of optimizing mFAPs for molecular biology and bionanotechnology applications appear promising. Because the bound chromophore can readily exchange with free chromophore in solution in a binding/unbinding equilibrium, a future direction would be to demonstrate that the mFAP system is amenable to super-resolution microscopy⁷⁶ techniques such as Points Accumulation for Imaging in Nanoscale Topography (protein-PAINT⁷⁷), a type of single-molecule localization microscopy (SMLM). In principle, stochastic formation of protein–chromophore complexes results in fluorescence bursts (without a photoactivation step) for protein-PAINT, and the density of fluorescence bursts should be tunable via the chromophore labeling concentration. Although my preliminary SMLM experiments using mFAP2a and mFAP2b labeled with DFHBI or DFHBI-1T show hints of a true SMLM signal (data not shown), the mFAP platform requires further exploration of parameters affecting SMLM signal, including microscope parameters (e.g. frame rate, exposure time, and laser power density), biological parameters (e.g. type of chromophore, chromophore concentration, presence of O₂ scavengers), as well as SMLM analysis parameters (e.g. fluorescence burst intensity threshold and number of frames analyzed). If successful, due to the thermodynamic coupling between DFHBI and Ca²⁺

binding in the Ca^{2+} -responsive mFAPs, it is suggested that the fluorescence burst rate could be tuned by modulating either DFHBI concentration or Ca^{2+} ion concentration.

Additional future directions involve improving Ca^{2+} ion affinity and fluorescence fold-change upon Ca^{2+} ion binding, which would require amino acid sequence re-engineering via residue insertions, deletions, and mutations in the EF-hand motif(s) and linker sequences connecting the EF-hand motifs to the mFAPs. Another potential future direction would be to address any side-effects exhibited by expressing Ca^{2+} -responsive mFAPs *in cyto* or *in vivo*, which are not currently observed but also not thoroughly investigated. It is known that *in vivo* expression of the GFP-based Ca^{2+} biosensor GCaMP produces cellular side-effects due to the calmodulin domain in GCaMP disrupting *in vivo* Ca^{2+} dynamics and gene expression, thereby interfering with both gating and signaling of L-type calcium channels (CaV1)¹⁶. It was found that GCaMP expression side-effects could be mitigated by incorporating an extra calmodulin domain into GCaMP, producing GCaMP-X, effectively protecting CaV1-dependent excitation–transcription coupling from perturbations¹⁶. It is therefore suggested that any side-effects of *in cyto* or *in vivo* expression of Ca^{2+} -responsive mFAPs might be improved by fusion of an extra calmodulin domain to the N- or C-terminal residues. With further feedback and improvements from researchers around the world, the future of the mFAP platform in molecular biology, bionanotechnology and beyond appears bright.

References

1. Bhalla, N., Jolly, P., Formisano, N. & Estrela, P. Introduction to biosensors. *Essays Biochem.* **60**, 1–8 (2016).
2. Chalfie, M. Green fluorescent protein as a marker for gene expression. *Trends in Genetics* **10**, 151 (1994).
3. Cirino, P. C., Mayer, K. M. & Umeno, D. Generating mutant libraries using error-prone PCR. *Methods Mol. Biol.* **231**, 3–9 (2003).
4. Miyazaki, K. & Arnold, F. H. Exploring nonnatural evolutionary pathways by saturation mutagenesis: rapid improvement of protein function. *J. Mol. Evol.* **49**, 716–720 (1999).
5. Huang, P.-S., Boyken, S. E. & Baker, D. The coming of age of de novo protein design. *Nature* **537**, 320–327 (2016).
6. Kan, S. B. J., Lewis, R. D., Chen, K. & Arnold, F. H. Directed evolution of cytochrome c for carbon-silicon bond formation: Bringing silicon to life. *Science* **354**, 1048–1051 (2016).
7. Alford, R. F. *et al.* The Rosetta All-Atom Energy Function for Macromolecular Modeling and Design. *J. Chem. Theory Comput.* **13**, 3031–3048 (2017).
8. Kim, D. E., Blum, B., Bradley, P. & Baker, D. Sampling bottlenecks in de novo protein structure prediction. *J. Mol. Biol.* **393**, 249–260 (2009).
9. Rocklin, G. J. *et al.* Global analysis of protein folding using massively parallel design, synthesis, and testing. *Science* **357**, 168–175 (2017).
10. Dou, J. *et al.* De novo design of a fluorescence-activating β -barrel. *Nature* **561**, 485–491 (2018).
11. Godinho, L. F. & Schrader, M. Determination of Peroxisomal pH in Living Mammalian

- Cells Using pHRed. *Methods Mol. Biol.* **1595**, 181–189 (2017).
12. Tantama, M., Hung, Y. P. & Yellen, G. Imaging intracellular pH in live cells with a genetically encoded red fluorescent protein sensor. *J. Am. Chem. Soc.* **133**, 10034–10037 (2011).
 13. Helassa, N., Podor, B., Fine, A. & Török, K. Design and mechanistic insight into ultrafast calcium indicators for monitoring intracellular calcium dynamics. *Scientific Reports* **6**, (2016).
 14. Li, Z. *et al.* Mutagenesis of mNeptune Red-Shifts Emission Spectrum to 681-685 nm. *PLoS One* **11**, e0148749 (2016).
 15. Tian, L. *et al.* Imaging neural activity in worms, flies and mice with improved GCaMP calcium indicators. *Nature Methods* **6**, 875–881 (2009).
 16. Yang, Y. *et al.* Improved calcium sensor GCaMP-X overcomes the calcium channel perturbations induced by the calmodulin in GCaMP. *Nat. Commun.* **9**, 1504 (2018).
 17. Henderson, M. J. *et al.* A Low Affinity GCaMP3 Variant (GCaMPer) for Imaging the Endoplasmic Reticulum Calcium Store. *PLoS One* **10**, e0139273 (2015).
 18. Strack, R. L. & Jaffrey, S. R. New approaches for sensing metabolites and proteins in live cells using RNA. *Curr. Opin. Chem. Biol.* **17**, 651–655 (2013).
 19. Autour, A., Westhof, E. & Ryckelynck, M. iSpinach: a fluorogenic RNA aptamer optimized for in vitro applications. *Nucleic Acids Res.* **44**, 2491–2500 (2016).
 20. Song, W., Strack, R. L., Svendsen, N. & Jaffrey, S. R. Plug-and-play fluorophores extend the spectral properties of Spinach. *J. Am. Chem. Soc.* **136**, 1198–1201 (2014).
 21. Song, W. *et al.* Imaging RNA polymerase III transcription using a photostable

- RNA-fluorophore complex. *Nat. Chem. Biol.* **13**, 1187–1194 (2017).
22. Yan, Q. *et al.* Localization microscopy using noncovalent fluorogen activation by genetically encoded fluorogen-activating proteins. *Chemphyschem* **15**, 687–695 (2014).
 23. Tebo, A. G. *et al.* Circularly Permuted Fluorogenic Proteins for the Design of Modular Biosensors. *ACS Chem. Biol.* **13**, 2392–2397 (2018).
 24. Olmsted, J. Calorimetric determinations of absolute fluorescence quantum yields. *The Journal of Physical Chemistry* **83**, 2581–2584 (1979).
 25. RNA mimics of green fluorescent protein. *AccessScience* doi:10.1036/1097-8542.yb130009
 26. Fleishman, S. J. *et al.* RosettaScripts: a scripting language interface to the Rosetta macromolecular modeling suite. *PLoS One* **6**, e20161 (2011).
 27. Das, R. & Baker, D. Macromolecular Modeling with Rosetta. *Annual Review of Biochemistry* **77**, 363–382 (2008).
 28. Mandell, D. J., Coutsias, E. A. & Kortemme, T. Sub-angstrom accuracy in protein loop reconstruction by robotics-inspired conformational sampling. *Nat. Methods* **6**, 551–552 (2009).
 29. Stein, A. & Kortemme, T. Improvements to robotics-inspired conformational sampling in rosetta. *PLoS One* **8**, e63090 (2013).
 30. Qian, B. *et al.* High-resolution structure prediction and the crystallographic phase problem. *Nature* **450**, 259–264 (2007).
 31. Wang, C., Bradley, P. & Baker, D. Protein-protein docking with backbone flexibility. *J. Mol. Biol.* **373**, 503–519 (2007).
 32. Siedlecka, M., Goch, G., Ejchart, A., Sticht, H. & Bierzynski, A. Alpha-helix nucleation by

- a calcium-binding peptide loop. *Proc. Natl. Acad. Sci. U. S. A.* **96**, 903–908 (1999).
33. Olsson, L. L. & Sjölin, L. Structure of Escherichia coli fragment TR2C from calmodulin to 1.7 Å resolution. *Acta Crystallogr. D Biol. Crystallogr.* **57**, 664–669 (2001).
 34. Fallon, J. L. & Quioco, F. A. A closed compact structure of native Ca(2+)-calmodulin. *Structure* **11**, 1303–1307 (2003).
 35. Stefan, M. I., Edelstein, S. J. & Le Novère, N. An allosteric model of calmodulin explains differential activation of PP2B and CaMKII. *Proc. Natl. Acad. Sci. U. S. A.* **105**, 10768–10773 (2008).
 36. Busch, E., Hohenester, E., Timpl, R., Paulsson, M. & Maurer, P. Calcium affinity, cooperativity, and domain interactions of extracellular EF-hands present in BM-40. *J. Biol. Chem.* **275**, 25508–25515 (2000).
 37. Ye, Y. *et al.* A grafting approach to obtain site-specific metal-binding properties of EF-hand proteins. *Protein Eng.* **16**, 429–434 (2003).
 38. Zondlo, S. C., Gao, F. & Zondlo, N. J. Design of an encodable tyrosine kinase-inducible domain: detection of tyrosine kinase activity by terbium luminescence. *J. Am. Chem. Soc.* **132**, 5619–5621 (2010).
 39. Guo, J. & Zhou, H.-X. Protein Allostery and Conformational Dynamics. *Chem. Rev.* **116**, 6503–6515 (2016).
 40. Malmstrom, R. D., Kornev, A. P., Taylor, S. S. & Amaro, R. E. Allostery through the computational microscope: cAMP activation of a canonical signalling domain. *Nature Communications* **6**, (2015).
 41. Chen, T.-W. *et al.* Ultrasensitive fluorescent proteins for imaging neuronal activity. *Nature*

- 499, 295–300 (2013).
42. Bovo, E., Martin, J. L., Tyryfter, J., de Tombe, P. P. & Zima, A. V. R-CEPIA1er as a new tool to directly measure sarcoplasmic reticulum [Ca] in ventricular myocytes. *Am. J. Physiol. Heart Circ. Physiol.* **311**, H268–75 (2016).
 43. Seidler, N. W., Jona, I., Vegh, M. & Martonosi, A. Cyclopiazonic acid is a specific inhibitor of the Ca²⁺-ATPase of sarcoplasmic reticulum. *J. Biol. Chem.* **264**, 17816–17823 (1989).
 44. Day, R. N. & Davidson, M. W. The fluorescent protein palette: tools for cellular imaging. *Chem. Soc. Rev.* **38**, 2887–2921 (2009).
 45. Cooper, S. *et al.* Predicting protein structures with a multiplayer online game. *Nature* **466**, 756–760 (2010).
 46. Huang, P.-S. *et al.* RosettaRemodel: a generalized framework for flexible backbone protein design. *PLoS One* **6**, e24109 (2011).
 47. Lin, Y.-R. *et al.* Control over overall shape and size in de novo designed proteins. *Proc. Natl. Acad. Sci. U. S. A.* **112**, E5478–85 (2015).
 48. Rohl, C. A., Strauss, C. E. M., Misura, K. M. S. & Baker, D. Protein Structure Prediction Using Rosetta. *Methods in Enzymology* 66–93 (2004). doi:10.1016/s0076-6879(04)83004-0
 49. Jacobs, T. M., Yumerefendi, H., Kuhlman, B. & Leaver-Fay, A. SwiftLib: rapid degenerate-codon-library optimization through dynamic programming. *Nucleic Acids Res.* **43**, e34 (2015).
 50. Studier, F. W. & William Studier, F. Protein production by auto-induction in high-density shaking cultures. *Protein Expression and Purification* **41**, 207–234 (2005).
 51. Würth, C., Grabolle, M., Pauli, J., Spieles, M. & Resch-Genger, U. Relative and absolute

- determination of fluorescence quantum yields of transparent samples. *Nature Protocols* **8**, 1535–1550 (2013).
52. Sjöback, R., Nygren, J. & Kubista, M. Absorption and fluorescence properties of fluorescein. *Spectrochimica Acta Part A: Molecular and Biomolecular Spectroscopy* **51**, L7–L21 (1995).
53. Skinner, S. O., Sepúlveda, L. A., Xu, H. & Golding, I. Measuring mRNA copy number in individual *Escherichia coli* cells using single-molecule fluorescent in situ hybridization. *Nat. Protoc.* **8**, 1100–1113 (2013).
54. Otwinowski, Z. & Minor, W. [20] Processing of X-ray diffraction data collected in oscillation mode. *Methods in Enzymology* 307–326 (1997).
doi:10.1016/s0076-6879(97)76066-x
55. Adams, P. D. *et al.* PHENIX: a comprehensive Python-based system for macromolecular structure solution. *Acta Crystallographica Section D Biological Crystallography* **66**, 213–221 (2010).
56. McCoy, A. J. *et al.* Phaser crystallographic software. *Journal of Applied Crystallography* **40**, 658–674 (2007).
57. Emsley, P., Lohkamp, B., Scott, W. G. & Cowtan, K. Features and development of Coot. *Acta Crystallographica Section D Biological Crystallography* **66**, 486–501 (2010).
58. Afonine, P. V. *et al.* Towards automated crystallographic structure refinement with phenix.refine. *Acta Crystallographica Section D Biological Crystallography* **68**, 352–367 (2012).
59. Gumbart, J., Trabuco, L. G., Schreiner, E., Villa, E. & Schulten, K. Regulation of the

- Protein-Conducting Channel by a Bound Ribosome. *Structure* **17**, 1453–1464 (2009).
60. Jorgensen, W. L., Chandrasekhar, J., Madura, J. D., Impey, R. W. & Klein, M. L. Comparison of simple potential functions for simulating liquid water. *The Journal of Chemical Physics* **79**, 926–935 (1983).
61. Maier, J. A. *et al.* ff14SB: Improving the Accuracy of Protein Side Chain and Backbone Parameters from ff99SB. *Journal of Chemical Theory and Computation* **11**, 3696–3713 (2015).
62. Case, D. A. *et al.* AMBER 14, University of California, San Francisco. (2014).
63. Wang, J., Wolf, R. M., Caldwell, J. W., Kollman, P. A. & Case, D. A. Development and testing of a general amber force field. *Journal of Computational Chemistry* **25**, 1157–1174 (2004).
64. Wang, J., Wang, W., Kollman, P. A. & Case, D. A. Automatic atom type and bond type perception in molecular mechanical calculations. *Journal of Molecular Graphics and Modelling* **25**, 247–260 (2006).
65. Frisch, M. J. *et al.* Gaussian 09, Revision C.01. (2010).
66. Bradbrook, G. M. *et al.* X-Ray and molecular dynamics studies of concanavalin-A glucoside and mannoside complexes Relating structure to thermodynamics of binding. *Journal of the Chemical Society, Faraday Transactions* **94**, 1603–1611 (1998).
67. Salomon-Ferrer, R., Götz, A. W., Poole, D., Le Grand, S. & Walker, R. C. Routine Microsecond Molecular Dynamics Simulations with AMBER on GPUs. 2. Explicit Solvent Particle Mesh Ewald. *Journal of Chemical Theory and Computation* **9**, 3878–3888 (2013).
68. Humphrey, W., Dalke, A. & Schulten, K. VMD: Visual molecular dynamics. *Journal of*

- Molecular Graphics* **14**, 33–38 (1996).
69. Scherer, M. K. *et al.* PyEMMA 2: A Software Package for Estimation, Validation, and Analysis of Markov Models. *Journal of Chemical Theory and Computation* **11**, 5525–5542 (2015).
 70. Roe, D. R. & Cheatham, T. E. PTRAJ and CPPTRAJ: Software for Processing and Analysis of Molecular Dynamics Trajectory Data. *Journal of Chemical Theory and Computation* **9**, 3084–3095 (2013).
 71. McGibbon, R. T. *et al.* MDTraj: A Modern Open Library for the Analysis of Molecular Dynamics Trajectories. *Biophysical Journal* **109**, 1528–1532 (2015).
 72. Schindelin, J. *et al.* Fiji: an open-source platform for biological-image analysis. *Nature Methods* **9**, 676–682 (2012).
 73. Lian, X. *et al.* Directed cardiomyocyte differentiation from human pluripotent stem cells by modulating Wnt/ β -catenin signaling under fully defined conditions. *Nature Protocols* **8**, 162–175 (2013).
 74. Tohyama, S. *et al.* Distinct Metabolic Flow Enables Large-Scale Purification of Mouse and Human Pluripotent Stem Cell-Derived Cardiomyocytes. *Cell Stem Cell* **12**, 127–137 (2013).
 75. Halbert, C. L., Allen, J. M. & Chamberlain, J. S. AAV6 Vector Production and Purification for Muscle Gene Therapy. *Methods in Molecular Biology* 257–266 (2018).
doi:10.1007/978-1-4939-7374-3_18
 76. Yan, Q. *et al.* Superresolution Localization Microscopy Using Fluorogen Activating Proteins. *Biophysical Journal* **100**, 476a (2011).
 77. Bozhanova, N. G. *et al.* Protein labeling for live cell fluorescence microscopy with a highly

photostable renewable signal. *Chem. Sci.* **8**, 7138–7142 (2017).

Curriculum Vitae

Jason Christopher Klima

klimaj@uw.edu; klima.jason@gmail.com

Education

- Ph.D. in Biochemistry and Nanotechnology & Molecular Engineering (Dual Degree), University of Washington, Seattle, June 2019
- B.S. in Chemistry and Biochemistry, College of Creative Studies, University of California, Santa Barbara, September 2011
 - Minor in Music, College of Letters and Sciences, University of California, Santa Barbara, September 2011

Publications

- Scott E. Boyken, Mark A. Benhaim, Florian Busch, Mengxuan Jia, Matthew J. Bick, Heejun Choi, **Jason C. Klima**, Zibo Chen, Carl Walkey, Alexander Mileant, Aniruddha Sahasrabudde, Kathy Y. Wei, Edgar A. Hodge, Sarah Byron, Alfredo Quijano-Rubio, Banumathi Sankaran, Neil P. King, Jennifer Lippincott-Schwartz, Vicki H. Wysocki, Kelly K. Lee, David Baker. *De novo* design of tunable, pH-driven conformational changes. *Science* **364**(6441): 658-664 (2019).
- Kelly Jin, **Jason C. Klima**, Grant Deane, Malcolm Dale Stokes, Michael I. Latz. Pharmacological investigation of the bioluminescence signaling pathway of the dinoflagellate *Lingulodinium polyedrum*: evidence for the role of stretch-activated ion channels. *Journal of Phycology* **49**(4): 733-45 (2013).

Awards and Honors

- National Science Foundation Graduate Research Fellowship Program, 2014–2019
- National Institutes of Health Postbaccalaureate IRTA Fellowship, 2011–2013
- Merck and Company Index Award, 2011
- Phi Lambda Upsilon Award, National Honorary Chemical Society, 2011
- Burnham Scholarship for Engineering and Applied Sciences, 2007–2012
- Summer Institute of Mathematics and Science (SIMS) Program, 2007
- Excellence in Physics Award, SIMS, 2007
- Member of Golden Key International Honour Society, 2016–current
- Member of the RosettaCommons, 2014–current
- Member of University of Washington Nanotechnology & Molecular Engineering Student Association, 2013–current

- Member of University of California, Santa Barbara, Chemistry Club, 2009–2011
- Member of NIH Mitochondrial Interest Group, Genetics Interest Group, and RNA Club, 2012–2013
- Member of the National Society of Collegiate Scholars, 2008–current
- Member of the National Society of High School Scholars, 2006–current

Work Experience

- Spring 2014–current: Graduate Research Assistant
 - Institute for Protein Design, University of Washington, Seattle, WA
 - Research: Computational protein design of small molecule fluorescent biosensors. Optimizing apixaban-binding proteins using computational modeling and directed evolution.
 - Supervisors: Drs. David Baker and James B. Hurley
- Winter 2014–Spring 2014: Graduate Research Assistant
 - Department of Biochemistry, University of Washington, Seattle, WA
 - Research: Characterizing the functionally distinct domains of mammalian mitochondrial fusion proteins Mfn1/2.
 - Supervisor: Dr. Suzanne Hoppins
- Autumn 2014–Winter 2014: Graduate Research Assistant
 - Department of Biochemistry, University of Washington, Seattle, WA
 - Research: Developing glutamate- and aspartate-sensing fluorescent reporters to probe photoreceptor metabolism.
 - Supervisors: Drs. James B. Hurley and Susan Brockerhoff
- Autumn 2011–Summer 2013: Post-baccalaureate Intramural Research Training Award (IRTA) Fellow
 - National Institutes of Health, Bethesda, MD
 - Research: Developing a methodology to genetically transform mammalian mitochondria for studying structure-function relationships. Characterizing a temperature-sensitive mitochondrial DNA mutant *D. melanogaster* model. Testing a hypothesis for synthesizing photoactive mitochondria.
 - Supervisor: Dr. Hong Xu
- Summer 2010–Autumn 2010: Laboratory Assistant
 - University of California, San Diego, Skaggs School of Pharmacy and Pharmaceutical Sciences
 - Research: Collecting live mouse tissue samples, genotyping transgenic/knockout mice, DNA extraction from human blood, DNA microchipping, and SNP detection by mass spectrometry.
 - Supervisor: Dr. Kang Zhang
- Summer 2009–Autumn 2009, & Summer 2010–Autumn 2010: Research Assistant
 - University of California, San Diego, Scripps Institution of Oceanography
 - Research: Characterizing the signal transduction pathway of spontaneous bioluminescence in dinoflagellate cells using pharmacological agonists/antagonists for receptors implicated in luminescence.

- Supervisor: Dr. Michael Latz
- Summer 2009–Autumn 2009: Computer Technician
 - University of California, San Diego, Salk Institute for Biological Studies
 - Research: Designing and maintaining the laboratory website, and gaining experience with the scientific grant submission process.
 - Supervisor: Dr. Ursula Bellugi
- Autumn 2008–Winter 2008: Laboratory Assistant
 - University of California, Santa Barbara, Department of Chemistry and Biochemistry
 - Research: Performing UV/Vis spectroscopy and high-performance liquid chromatography to isolate siderophores from marine bacteria.
 - Supervisor: Dr. Allison Butler
- Summer 2008–Autumn 2008: Marine Physical Laboratory Summer Internship
 - University of California, San Diego, Scripps Institution of Oceanography
 - Research: Characterizing the signal transduction pathway of spontaneous bioluminescence in dinoflagellate cells.
 - Supervisor: Dr. Grant Deane
- Autumn 2006–Summer 2007: Laboratory Assistant, Muscle Tissue Core
 - Veterans Medical Research Foundation, La Jolla, CA
 - Research: Gaining experience with Coulter counting, gel electrophoresis, glucose assays, western blot development using radiolabeled peptides, performing radiation tests, and making buffers.
 - Supervisors: Drs. Susan Phillips and Theodore P. Ciaraldi

Research Skills

- Computer Programming Languages
 - Python
 - XML
 - JSON
 - Bash
 - HTML
 - PyMOL
- Research Fields of Expertise
 - Biochemistry
 - Western Blotting
 - Recombinant Protein Expression
 - Protein Purification
 - Tissue Culture
 - Transfection
 - Nanotechnology
 - Fluorescence Spectroscopy
 - Fluorescence Anisotropy
 - Molecular Engineering

- Rosetta
 - Protein Structure Prediction
 - Protein-protein Interactions
 - Protein-ligand Interactions
 - Small Molecule Binder Design
- Microscopy
 - Confocal Microscopy
 - Fluorescence Microscopy
 - Epi-fluorescence Microscopy
 - Light Microscopy
- Protein Engineering
 - Biosensors
 - Flow Cytometry
 - Protein Chemistry
 - Protein Characterization
 - Protein Assays
 - Structural Biology
 - Stability Studies
- Molecular Genetics
 - Polymerase Chain Reaction (PCR)
 - Real-Time PCR (qPCR)
 - Molecular Cloning
 - Genetics
 - Microbiology
 - Gel Electrophoresis
- Additional Research Skills
 - Scientific Writing
 - Data Analysis
 - Assay Development
 - High-performance Computing

Teaching Experience

- PyRosetta Bootcamp Instructor, Institute for Protein Design, University of Washington, 2019
- PyRosetta Code School Instructor, RosettaCommons, Johns Hopkins University, 2019
- University of Washington Center for Learning and Undergraduate Enrichment (CLUE) Tutor: Biochemistry 405, Autumn Quarter 2017
- University of Washington Teacher's Assistant: Biochemistry 405, Autumn Quarter 2015
- University of Washington Teacher's Assistant: Biochemistry 441, Winter Quarter 2015
- University of Washington Teacher's Assistant: Biochemistry 440, Autumn Quarter 2014

Volunteer Experience

- Pacific Science Center Life Sciences Research Weekend: 2014, 2015, 2016, 2017.
 - At the University of Washington Center for Game Science booth, I taught children and their parents how protein engineers discover cures to treat diseases, and explained how nanotechnology research at the University of Washington is advancing disease treatment options. Participating in this outreach program allowed me to translate my technical experience into casual language that boosted my local community's comprehension of nanotechnological research while inspiring young adults into science, technology, engineering and mathematics (STEM) fields through interactive workshops.
- University of Washington Engineering Discovery Days: 2014, 2015, 2016.
 - At this joint exhibit between the Molecular Engineering and Sciences Institute and the Washington Nanofabrication Facility, I and fellow University of Washington students and faculty in engineering shared our research with the local Seattle community, particularly with children in K-8 grades.

Vitae

Jason Christopher Klima grew up in San Diego, CA. In 2003, he began playing piano and developed a repertoire of works by Chopin, Liszt, Debussy, Schubert, and Beethoven, including his own compositions. By 2007, while studying gold nanowire nucleation he became fascinated with the biological sciences, and also finished writing a symphony. In 2011, he earned a Bachelor of Science degree in Chemistry and Biochemistry from the College of Creative Studies, University of California, Santa Barbara (UCSB). He additionally earned a Minor in Music from the College of Letters and Sciences, UCSB, where he studied music composition, played viola for the UCSB symphony orchestra, and sang in the UCSB chamber choir. While studying mammalian mitochondrial genetic transformation at the National Institutes of Health (NIH) as a Postbaccalaureate Intramural Research Training Award (IRTA) Fellow under the mentorship of Dr. Hong Xu, he played viola with the NIH Philharmonia, and acted as Music Director for the NIH a cappella group Nerds In Harmony. In 2019, he earned a Doctor of Philosophy degree in Biochemistry and Nanotechnology & Molecular Engineering at the University of Washington under the mentorship of Drs. David Baker and James B. Hurley.